Broadband Modeling of Earthquake Sources and Mantle Structures

Thesis by

Teh-Ru Alex Song

In Partial Fulfillment of the Requirements

for the Degree of

Doctor of Philosophy

California Institute of Technology

Pasadena, California

2006

(Submitted 6/23/2006)

(graduation date should be 2008)

© 2006
Teh-Ru Alex Song
All Rights Reserved

Broadband Modeling of Earthquake Sources and Mantle Structures

Thesis by

Teh-Ru Alex Song

In Partial Fulfillment of the Requirements

for the Degree of

Doctor of Philosophy

California Institute of Technology

Pasadena, California

2006

(Submitted 6/23/2006)

(graduation date should be 2008)

Acknowledgements

Being at Caltech has been a special experience for me. I would like to first thank my advisor, Don Helmberger. He gives me unlimited freedom to basically do whatever I want. During my 6 years stay at Seismo Lab, Don has presented me with enthusiam for picking apart every wiggle of the seismogram and has emphasized the significance of looking at the data. Even during the end of my phD, Don allowed me to complete my thesis any place I desired and I am so grateful for his kindness and consideration. Besides, chating with him on basketball is always entertaining and fun. Thank you Don !

During the past few years, seismo lab has given me great opportunities to work on different topics with Mark Simons, Jeroen Tromp and Hiroo Kanamori. Every one of them presents a unique personality and style of research. It certainly put an imprint on how I deal with different problems. Working with them is such a wonderful experience and thank them so much for guiding me through various difficulties. In addition, Don Anderson Mike Gurnis and Paul Asimow all provided great ideas about my research and thesis and gave me lots of valuable comments.

Of course, many people have given me a hand when I needed it the most. To name a few: Chen Ji often behaves like a big brother and we always have great time discussing various problems. Certainly, Qinya's presence gives me a different outlook on life and has helped me throughout the years. I thank her so much and wish her the best. During difficult times in my phD, my landlord Helen treated me like family and made me feel at home. Without her, it would not have been possible to complete the thesis. Also, I am grateful for the help and company from my office mates, Evelina, Viola and Rosemary, and many others in the lab. Finally, I would like to dedicate

this thesis to my family in Taiwan and my Ally.

Abstract

Broadband seismic arrays have provided unprecedented data sets for seismologists to image the slips on faults and velocity structure beneath Earth's surface at all scales. In particular, plate boundary zones are the most complicated regions on the surface and full of complexities. Often that great earthquakes occur and rapid structural changes take place.

In my thesis, one major effort is to use geophysical data and broadband seismic data to characterize the occurrences of great earthquakes at the subduction zone interface. Using gravity data from satellite and bathymetry model ETopo5, I recognized the strong correlation between gravity, topography and the occurrences of great earthquakes. Such a correlation gives a strong indication that lateral variations in the occurrences of great earthquakes at a given subduction zone are strongly linked to the fore-arc structure and topographic features such as basin and peninsulas. I also give robust estimates of the size and rupture extent of the recent 2004 Sumatra-Andaman giant earthquake using Earth's normal modes.

Another part of my thesis consists of modeling waveform distortion and interference to study lithosphere and deep upper mantle structure. Modeling multi-pathing associated with sharp structure has become a very powerful method to delineate structure and explain the complicated behavior shown in the data recorded by dense arrays.

Future research will focus on linking geodynamic models and seismic analysis of broadband waveform data as a way to further constrain the mantle structure and validate various geodynamic models.

Contents

List of Figures

List of Tables

Overview

0.1 Introduction

Plate tectonics has become one of the most successful theories describing the kinematics of the movement of the solid Earth. Great earthquakes occur mostly in the plate boundary, especially at the subduction zone interface. However, the occurrences of these great earthquakes are not uniform and vary substantially among different subduction zones. Even within a given subduction zone, the release of energy is not uniform but rather shows significant lateral variations. It is not clear what controls these spatial differences and over what time scale they form and persist.

Giant earthquakes ($M_w > 9$) rarely happen but generate tremendous energy. The 2004 Sumatra-Andaman giant earthquake ruptured the Sunda Arc, generating a huge tsunami. To accurately estimate the size of this event, I model very long period normal modes ($>$ 1000 sec) using a centroid and finite rupture model. This gives robust estimate on the size of this earthquake and its rupture extent, while it can also validate rupture models constructed using surface waves and body waves.

Seismic structures usually change very rapidly near the place where deformations occur currently or in the past. While velocity structures near plate boundary zones often vary rapidly, there are deformation zones within the plate interior that also show large contrast in seismic structures. Recent dense broadband seismic networks and PASSCAL experiments provide excellent chances to explore such complexities.

This thesis is divided into two parts. The first part focuses on the great earthquakes occurring at the subduction zone interfaces and contains chapter 1 and chapter 2. It includes analysis of variations in the occurrences of great earthquakes at

subduction zone interfaces using gravity data and topography data. In addition, it contains modeling of unprecedented, very-long-period normal modes data of the 2004 Sumatra-Andaman giant earthquake. The second part of the thesis focuses on the broadband modeling of upper mantle triplications (Chapter 3, Chapter 4) and wave diffractions along dipping lithosphere structures (Chapter 5, Chapter 6).

In Chapter 1, I present analysis of satellite gravity data and topography data of global subduction zones and associate them with the occurrences of great earthquakes at the subduction zone interfaces. Though the convergence velocity of the plate and its age have been suggested to relate to the occurrence of great earthquakes at different subduction zones, lateral variations in the occurrences of great earthquakes along a given subduction zone suggests mechanical properties at the subduction zone interface might change rapidly as well, due to differences in fluid content, sediment thickness, structures in the upper plate, etc. Gravity has long been used as a proxy to study the variation in stress in the crust and mantle. Here I correlate the gravity, topography and the occurrences of great earthquakes and find a strong correlation between spatial variations in gravity, topography and the occurrences of great earthquakes in the forearc regions. I discuss the importance of such a strong correlation and its link to geological structure at million years time scale.

In Chapter 2, I present modeling of very long period free Earth's oscillations of the Sumatra-Andaman giant earthquake. This giant event occurred on 24 December 2004 near northern Sumatra and ruptured northward more than 1000 km to the Andaman Islands. Sea floor deformation caused by the displacement along the subduction zone interface produced a tsunami that caused tremendous fatalities and damage. However, the size and rupture extent were not clear even soon after the disaster. Harvard CMT solution and teleseismic body wave inversion both indicated that the earthquake centroid was near $3^\circ - 4^\circ N$ and the moment magnitude near Mw 9.0. However, these results underestimated the amplitude of long period surface waves ($>$ 500 secs) and very long period normal modes ($>$ 1000 secs). I find that the splitting pattern of the gravest mode ${}_0S_2$ singlets provided indisputable evidence that this giant earthquake ruptured significantly toward the north and the centroid was near

7.5°N. Using coupled-mode theory, I also model the modal spectrum below 1 mHz and constrain the finite fault model to explain very broadband seismic data in the 10-3300 secs period. Such approach is essential in studying great earthquakes.

In Chapter 3, I present direct S wave triplication data to investigate the extent of a possible low velocity layer in the deep upper mantle beneath the northwestern United States. In particular, I find that the secondary branch AB at the epicentral distance of $21^\circ - 24^\circ$ is powerful. At these ranges, the strong AB branch is bottoming near the depth of the 410 discontinuity and serves as a nice proxy of the existence of a low velocity layer (or low velocity gradient) atop the 410. Such a low velocity layer atop the 410 has major potential implications for the water content in Earth's transition zone. Modeling waveform data recorded at TriNet and several other PASSCAL arrays for several events offshore Oregon and Washington, I map out the extent of such low velocity layers. I also examine the consistency of my model with previous receiver function results and find they are complementary to each other.

In Chapter 4, I extend the analysis in Chapter 3 from 1D models to 2D finite difference models but focus on the dataset recorded by TriNet from events offshore Oregon. This dataset presents clear evidence of a sharp velocity contrast in the deep upper mantle changing from east to west. Such 3D waveform behavior can be reproduced with a simple model consisting of a low velocity zone in the deep upper mantle beneath northeastern California but diminishes rapidly to the northwest. Such a sharp change in velocity above the 410 is very useful to characterize the origin of this low velocity anomaly in the deep upper mantle.

In Chapter 5, I explore the usefulness of amplitude information and waveform distortion in validating existing travel time tomography models. For example, we consider waveform data recorded at La Ristra Transect across the Rio Grande Rift in the southwestern United States from events beneath South America. Synthetics produced by the original travel time tomographic model do not explain the waveform distortion and amplitude variations presented in the data. We consider an amplified tomographic model with a slab-like feature extending to about 600 km that has a much larger velocity contrast to the ambient mantle. Simply amplifying the tomographic

model gives a much better fit to the amplitude variation and waveform distortions. A simplified model constructed independently also shows a consistent result. Incoming waves propagating through such a dipping velocity contrast produce waveform distortion and amplitude decay through diffraction along the boundary. Systematic investigations show how to constrain the geometry and amplitude of such a dipping velocity contrast, which is complementary to travel time delay measurement. Consistent modeling of both P and S waveform distortion and amplitude decay are shown later in Chapter6 with some speculations on the origin of such a dipping structure near the edge of the Great Plains and the Rio Grande Rift.

In Chapter 6, I present results of modeling P and S waveform distortions across the slab-like feature beneath the edge of the western Great Plains and the Rio Grande Rift. I use the preferred amplified S model and scale it to the P model using a scaling factor $dlnVs/dlnVp$. Such a simple procedure produces a consistent model that explains the whole dataset from exactly the same source-receiver pairs. Incoming waves sampling this dipping structure give direct constraints on its physical origin. The modeling result gives a relatively low scaling factor $dlnVs/dlnVp$, which suggests that this dipping structure is likely compositionally distinct from the ambient mantle.

Chapter 1

Large Trench-Parallel Gravity Variations Predict Seismogenic Behavior in Subduction Zones

Abstract

We demonstrate that great earthquakes occur predominantly in regions with strongly negative trench parallel gravity anomalies (TPGA), whereas regions with strongly positive TPGA are relatively aseismic. These observations suggest that, over time scales up to at least 1 My, spatial variations of seismogenic behavior within a given subduction zone are stationary and linked to the geological structure of the fore-arc. The correlations we observe are consistent with a model in which spatial variations in frictional properties on the plate interface control variations in fore-arc topography, gravity, and seismogenic behavior. *(Originally published as Song and Simons, Science, 301, 630-633, 2003)*

1.1 Introduction

Studies of profiles of the gravity field taken perpendicular to the strike of subduction zones suggest that trench-normal gravity profiles are predominantly controlled by mantle rheology, slab buoyancy, and interplate shear tractions on the plate interface (1-8). Under the premise that spatial variations in gravity over the fore-arc serve as a proxy for the long term state of stress on the plate interface, we investigate trench-parallel gravity anomalies (TPGA) using global marine gravity grids (9, 10). The large amplitude, longer wavelength trench-normal gravity variations can overwhelm the smaller amplitude TPGA (Fig. 1.1A).

Therefore, in constructing maps of TPGA, we subtract an average regional trench-normal gravity profile from the original free-air gravity data (11, 12, Fig. 1.1B). For this analysis, we are only concerned with TPGA over the location of the plate interface where large thrust earthquakes occur (less than 50 km). We hypothesize that the large amplitude variations of TPGA that we observe (order of 40 mGal) correspond to variations in shear tractions on the plate interface, which are in turn dependent on normal tractions and the coefficient of friction, and may impact the seismogenic character of a given subduction zone. To test this hypothesis, we compare our estimates of TPGA with co-seismic distributed slip models from selected earthquakes, as well as with the epicenters of large earthquakes from the Harvard CMT and relocated ISC global catalogs (13-15). We first consider the three largest earthquakes of the century: 1960 Chile (moment magnitude, M_w 9.5), 1964 Alaska (M_w 9.2) and 1952 Kamchatka (M_w9.0). For the Alaska/Aleutians subduction zone, we find a strong visual correlation between the location of the principal areas experiencing large co-seismic slip in the 1964 Alaska earthquake (M_w 9.2) (16) and negative TPGA (Fig. 1.1B). A region of lower co-seismic slip between the two high-slip areas correlates with a region of positive TPGA (Fig. 1.1B). Regions of large co-seismic slip, as inferred from distributed slip models of the 1938 Alaska (M_w 8.3), 1957 Aleutian (M_w 8.6), and 1965 Aleutian (M_w 8.7) earthquakes (17, 18), also occur predominantly in regions of negative TPGA. Areas of large co-seismic slip during the 1938 earthquake are bounded to the

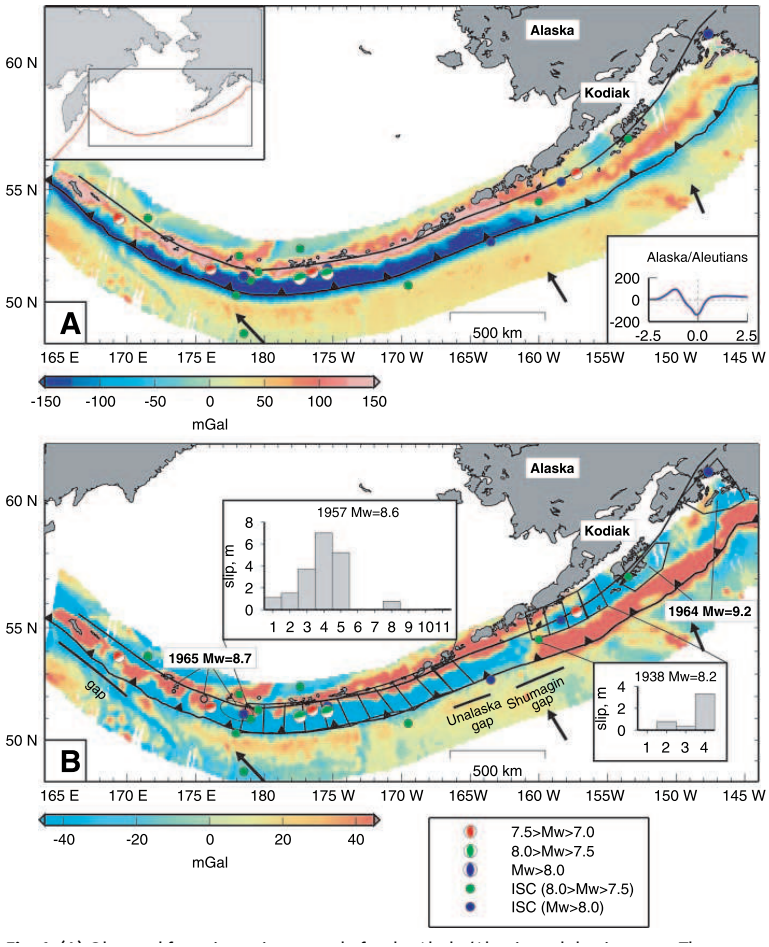

Figure 1.1: (A) Observed free-air gravity anomaly for the Alaska/Aleutian subduction zone. The average trench-normal gravity profile is calculated for the region shown in the inset and is shown in the sub-panel of Fig. 1.1A, with the horizontal axis being trench-normal distance in degrees and vertical axis being gravity in mGal. The color bar shows the amplitude of the free-air gravity anomaly. (B) Estimated TPGA for the Alaska-Aleutian subduction zone. The color bar shows the amplitude of TPGA. For the 1938 and 1957 events (17, 18), we indicate their respective slip distributions in the inset panels and the fault parameterization is indicated on the TPGA map. Areas with large co-seismic slip during 1964 Alaska and 1965 Aleutian earthquakes (16, 17) are outlined in black lines. For all panels, subduction zone earthquakes from the ISC (1900-1976) with $M_w \geq 7.5$ and Harvard CMT (1976-2001) catalogs with $M_w \geq 7.0$ are plotted as solid circles and moment tensors, respectively. For both (A) and (B), trench location (40) and 50 km slab iso-depth contour (41) are indicated by the barbed and thick black lines, respectively. Directions of relative plate convergence (42) are shown as arrows.

west (the Shumagin segment) and on the up-dip limit by regions of positive TPGA. Similarly, the along strike extent of the 1960 Chilean earthquake (19) is bounded by regions of increasing TPGA (Fig. 1.6A). The Kurile/Kamchatka subduction zone also shows a strong correlation between the location of large earthquakes and negative TPGA, with an obvious gap in the occurrence of large earthquakes corresponding to a 600 km long region of positive TPGA (Fig. 1.6B). Areas of large co-seismic slip during the 1952 Kamchatka earthquake (20), however, correspond to both positive and negative TPGA. We note that spatial distribution of slip shown for these historical events might not be tightly constrained due to lack of sufficient data (Section 1.2).

We rely on global earthquake catalogs to explore more systematically the relationship between occurrences of large earthquakes and TPGA over the past century. We estimate the mean TPGA within the fault area for each subduction zone earthquakes with $M_w \geq 6.0$ (11). We find that the total seismic moment associated with subduction zone earthquakes located on the slab interface is localized to regions of negative TPGA (Section 1.2, Fig. 1.6). To emphasize the relationship between large earthquakes and TPGA, we consider histograms of moment release vs. TPGA, using four bins of about equal areas of the plate interface. Seismic moment released in one fourth of the total area with positive TPGA (> 40 mGal) accounts for less than 5% of the total moment released in the 20th century regardless of whether or not we include the three largest earthquakes. Furthermore, the average seismic moment per event for earthquakes occurring in areas with negative TPGA (< -40 mGal) is over ten times larger than that for those occurring in areas with large positive TPGA (Section 1.2). We note that while great earthquakes occur predominantly in areas with large amplitude negative TPGA, the converse relationship does not necessarily hold, i.e., not all regions with negative TPGA necessarily experience great earthquakes.

Using the ETOPO-5 (21) digital elevation model, we treat bathymetry in the same manner as the gravity field to form the trench parallel topography anomaly (TPTA) (11). Areas with strongly negative TPGA and TPTA (< -750 m) are the most active in terms of both the number of total events and the number of large events ($M_w \geq 7.5$) (Fig. 1.2B, Fig. 1.10). Corresponding regions with strongly positive

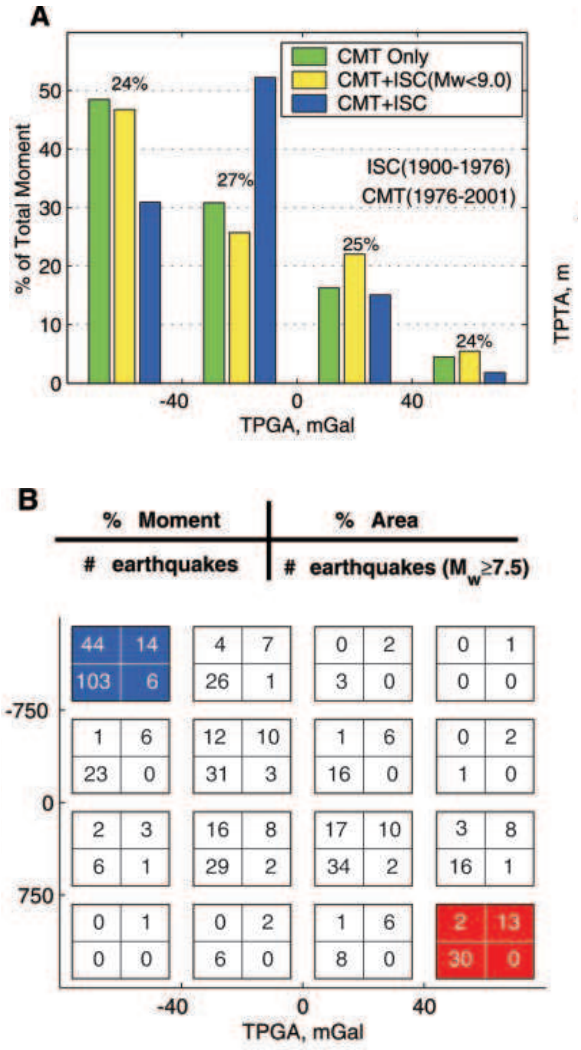

Figure 1.2: (A) Histogram of total seismic moment vs. TPGA. We consider separate events only in the CMT catalog (1976-2001), as well as a combined set of CMT (1976-2001) and ISC (1900-1976). We only consider events with $M_w \geq 6.0$. The percentage of area in each bin is shown above each bar. (B Seismic moment release vs. TPGA and TPTA. The number in the upper-left corner of each cell indicates the percent of total moment associated with the corresponding range of TPGA and TPTA. The numbers at upper-right, lower-left, and lower-right corner in each patch indicate percent of interface area, number of earthquakes, and number of large earthquakes ($M_w \geq 7.5$), respectively. CMT solutions are given a quality factor ranging from A to H and only events with the best quality factor (A and B) are considered and a 10 MPa stress drop is assumed when estimating the slip area for each event. Results using all CMT events, 1 MPa stress drop or different combination of catalogs are shown in Figs. 1.7- 1.10.

TPGA and TPTA (> 750 m) are relatively quiescent.

Most remarkably, 14% of the area with strongly negative TPGA and TPTA corresponds to 44% of total moment released, while equivalent areas with strongly positive TPGA and TPTA only represent 2% of total moment. Seismic moment density (moment per unit area) in areas with strongly negative TPGA and TPTA (Fig. 2B, Fig. 1.10, blue bin), is over 40 times that occurring in areas with strongly positive TPGA and TPTA (Fig. 1.2B and Fig. 1.10, red bin).

Geodetic observations of strain accumulation complement inferences based on earthquake locations by constraining the extent of coupling in a given subduction zone. For instance, a GPS array installed in 1994 to investigate strain accumulation in the Shumagin gap and on Kodiak Island in the Alaska-Aleutian subduction zone indicates that Kodiak Island, a region of negative TPGA, overlies a strongly-coupled segment of the subduction zone (22, 23) with an implied potential for large earthquakes (Fig. 1.1B). GPS data for the Shumagin gap, a region of positive TPGA, shows much less strain accumulation (24, 25) and is inferred to overlie a segment of the subduction zone that is relatively uncoupled.

Fore-arc basins off the Nankai Trough in Japan are known to coincide with the size and spatial extents of areas of significant moment release during great earthquakes (26). The Kermadec subduction zone, normally considered to be relatively aseismic, contains a spatially restricted region several hundred kilometers long, which has experienced several large earthquakes (Fig. 1.11A). This seismically active zone occurs within a much broader region of negative TPGA, but more importantly, as with Nankai, it conforms to a fore-arc basin characterized by a 1.5 km increase in sediment thickness (Fig. 1.11A) (27). Such a strong correlation between topographic depressions and the locations of great earthquakes (28) is equivalent to the correlation with large amplitude negative TPTA.

Along-strike variations in the position of the coastline (29) relative to the trench can also be considered as a form of TPTA. For instance, models of co-seismic slip from the 1995 M_w 8.1 Antofagasta earthquake (30) show that the region of significant co-seismic slip terminated just south of the Mejillones Peninsula. It remains to be seen

if slip in the seismic gap to the north (last rupture in 1877) will extend under the peninsula, or stop just north of it. Similarly, no significant co-seismic slip is inferred to have occurred below Cape Muroto during the 1946 Nankai earthquake (31), and during the 1960 Chilean earthquake, co-seismic slip is inferred to have significantly decreased before reaching the peninsula south of the city of Conception (Fig. 1.6A) (19). The correlation of bathymetric highs with the absence of great earthquakes (32) is equivalent to the correlation with large amplitude positive TPTA.

We find that TPGA and TPTA are positively correlated in most areas, with little area in regions where TPTA and TPGA are uncorrelated (Fig. 1.2B, Fig. 1.10). This correlation is expected because gravity anomalies are intrinsically tied to topographic variations via a given compensation mechanism. Results from viscous models (4, 5), visco-elastic models (6, 7), and laboratory experiments (8) suggest that spatial variations in the magnitude of shear tractions on the plate interface can modulate surface topography and gravity in the fore-arc. In particular, these models indicate that increasing shear tractions on the plate interface induce a decrease in vertical compressive stress, thereby depressing fore-arc topography and gravity. Consistent with these models, we interpret our observations of TPGA and TPTA as indications of variations in shear tractions on the plate interface, with strongly negative TPGA and TPTA associated with relatively high shear tractions, and strongly positive TPGA and TPTA associated with relatively low shear tractions (Fig. 1.3, left panel).

Laboratory studies of the frictional behavior of sliding rock surfaces show that the tendency for stick-slip behavior (i.e., earthquakes) increases with increasing applied shear tractions (Fig. 1.3, right panel) (33), where shear tractions are a function of the applied normal stress on the sliding block and the coefficient of friction on the contact surface. The effective coefficient of friction on the plate interface is sensitive to many factors including differences in material properties, presence or absence of fluids, seafloor roughness, slab geometry, temperature, and contact time.

Subduction zones have been classified between two end-member groups, Chilean- and Mariana-type (34), and large scale inter-arc differences in seismogenic behavior are usually attributed to variations in age and convergence rate of the subducting

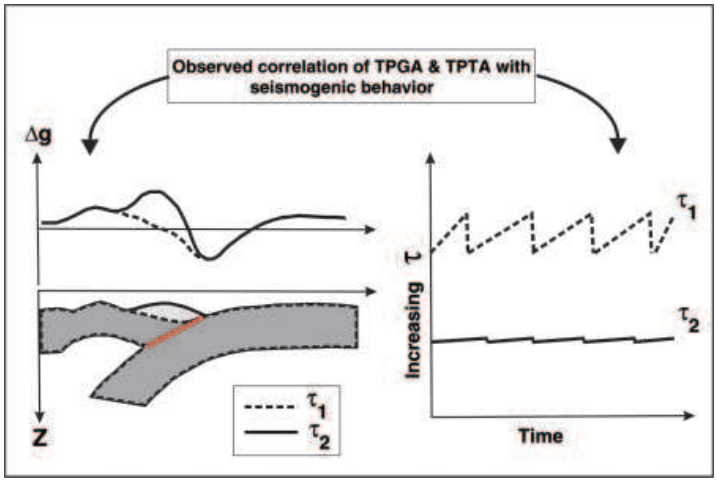

Figure 1.3: Left panel schematically shows variations in gravity and topography due to changes in shear tractions on the plate interface (red line). Solid and dashed lines indicate gravity and topography anomalies corresponding to lower (τ_1) and higher (τ_2) shear tractions on the plate interface. Right panel schematically indicate changes in seismogenic behaviors with changes in shear tractions. Large shear tractions tend to produce stick-slip behaviors and small shear tractions tend to produce stable-sliding behaviors.

plate (35), or normal tractions on the plate interface (36). However, our observed correlations between smaller scale intra-arc variations in TPGA and TPTA and seismogenic behavior suggest that variations in normal tractions within a given subduction zone are probably not the dominant factor. Negative TPGA and TPGA are associated with a reduction in normal tractions, which would on its own reduce the tendency for stick-slip behaviour. The observed correlation of negative TPGA and TPTA with the location of great earthquakes, suggests that the implied increases in shear tractions must be primarily due to increases in the effective coefficient of friction as opposed to increases in normal tractions. Likewise, positive TPGA, TPTA, and aseismic behavior are associated with relative decreases in the effective coefficient of friction.

Based on the observed correlation of TPGA and TPTA with seismogenic behavior, numerical modelling of fore-arc gravity and topography, and laboratory experiments on frictional behavior of sliding surfaces, we conclude that along-strike variations

in frictional properties of material on the plate interface within a given subduction zone are as important in controlling seismogenic behavior as those factors that differ between subduction zones. These variations must be sufficiently large within a given subduction zone to cause a transition between stick-slip and stable sliding behavior.

The amplitude of the variations in gravity and topography addressed here are many orders of magnitude larger than temporal variations over the seismic cycle. Thus, the observed spatial pattern of TPGA and TPTA must persist over time periods much longer than the typical inter-earthquake time ($10^2 - 10^3$ years) at a given segment of a subduction zone, and great earthquakes should be observed to consistently occur in areas with large amplitude negative TPGA in the fore-arc region.

Based on the observed TPGA, we make a few testable predictions for the seismogenic behavior of different segments of several subduction zones. We predict that the western Shumagin gap, Unalaska gap, and western Aleutians are expected to be accumulating elastic strain at shallow depths, while the eastern Shumagin gap, western Aleutians at depths greater than 25 km, and Kurile trench gap should have less strain accumulation (Fig. 1.1, Fig. 1.6B). In the northern South American subduction zone, segments between 1°N and 8°S show no occurrences of great earthquakes (37). Based on the value of TPGA in this region, we would predict low elastic strain accumulation in the northern segment ($1°N - 3°$S) and higher elastic strain accumulation in the southern segment ($4°S - 8°$S) (Fig. 1.11B). Future geodetic measurements (both on land and on the sea floor) can test our TPGA-based predictions of which seismic gaps are accumulating elastic strain, and which are associated with relatively uncoupled plate interfaces (38, 39).

Refining the details of the relationship between the gravity field and large earthquakes requires progress in several directions: (1) The simultaneous use of geodetic observations, tsunami waveforms, and seismological data to determine the absolute location of co-seismic slip of large subduction zone earthquakes; (2) the use of both marine and continental gravity data accounting for sediment thickness, and local shallow compensation effects above the plate interface; and (3) a suite of models investigating the mechanics of the subduction zone process that extend from the time

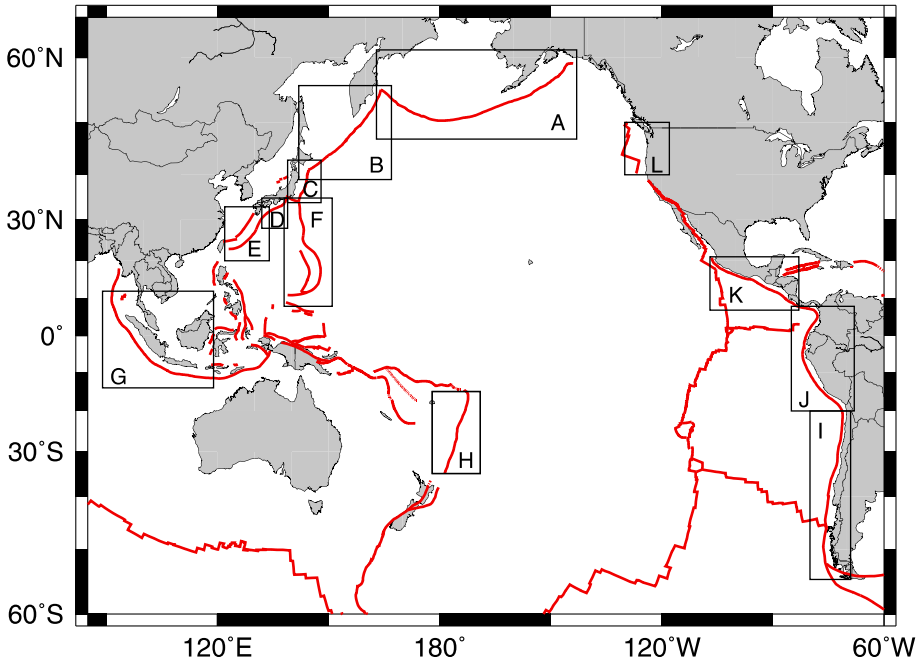

Figure 1.4: (A) Alaska-Aleutian (B) Kamchatka-Kurile (C) Japan (D) Nankai (E) Ryukyu (F) Izubonin-Mariana (G) Sumatra-Java (H) Tonga-Kermadec (I) Chile (J), northern South America, (K) Central America and (L) Cascadia. Average trench-normal profiles are computed using the regions as outlined.

scales of the seismic cycle to millions of years, with attention placed on the long term topography of the fore-arc.

1.2 Supplementary Materials and Methods

1.2.1 Construction of TPGA

The choice of the along-strike extent of the region used to calculate the local average trench-normal gravity profile is non-unique. Our choice corresponds to the regions outlined in Fig. 1.4.

Each region incorporates at most the entire extent of a given subduction arc, and at a minimum, the rupture zone of several great earthquakes (Fig. 1.1B, Figs. 1.4, 1.6, 1.11). By construction, the TPGA in a given region will integrate to zero along any

path a constant distance from the trench. In general, the gradients of TPGA discussed in this study are visible in the original free-air gravity data (compare Figs. 1.1A and 1.1B). The removal of the average trench normal profile serves to put all subduction zone s on a more comparable footing. The resulting TPGA primarily reflects short wavelength variations in shallow fore-arc structures (Fig. 1.1B), and can vary strongly in directions both parallel and perpendicular to the strike of the trench. There is no obvious systematic dependence of TPGA on the age of subducting plates or the type of overriding plate (continental or oceanic). We have used different sub-regions to calculate TPGA, and found very similar estimate of TPGA (Fig. 1.5).

1.2.2 Estimation of TPGA associated with subduction zone earthquakes

Because events in the relocated ISC and Harvard CMT catalogs are treated as point sources, we must assume a relationship between the size of the earthquake and the area that slipped. We assume a dip-slip rectangular fault with dimensions that scale with seismic moment and stress drop (S1). We consider extremal values of stress drops in the range of 1-10 MPa (S2). The slip area of each event is assumed to be square and centered on the hypocenter. If this assumption results in surpassing the surface or down dip limit of the slab interface, the assumed area becomes rectangular, with the slipping area extending along strike. The CMT location is determined as the centroid of energy release and considered as the best available global dataset of seismic moment and location. The CMT catalogue we use spans the time period from 1976 to 2001, while the relocated ISC catalogue begins in 1900. For events in the ISC catalogue without a corresponding CMT-determined seismic moment, we estimate moment via a moment-magnitude relationship (S3, S4).

The distribution of co-seismic slip for the three largest earthquakes may be complicated and our assumed hypocenter, fault area, and computed mean TPGA, may thus not adequately approximate reality. Therefore, for these three events, we use available distributed slip models (S5, S6, S7) to compute their associated TPGA.

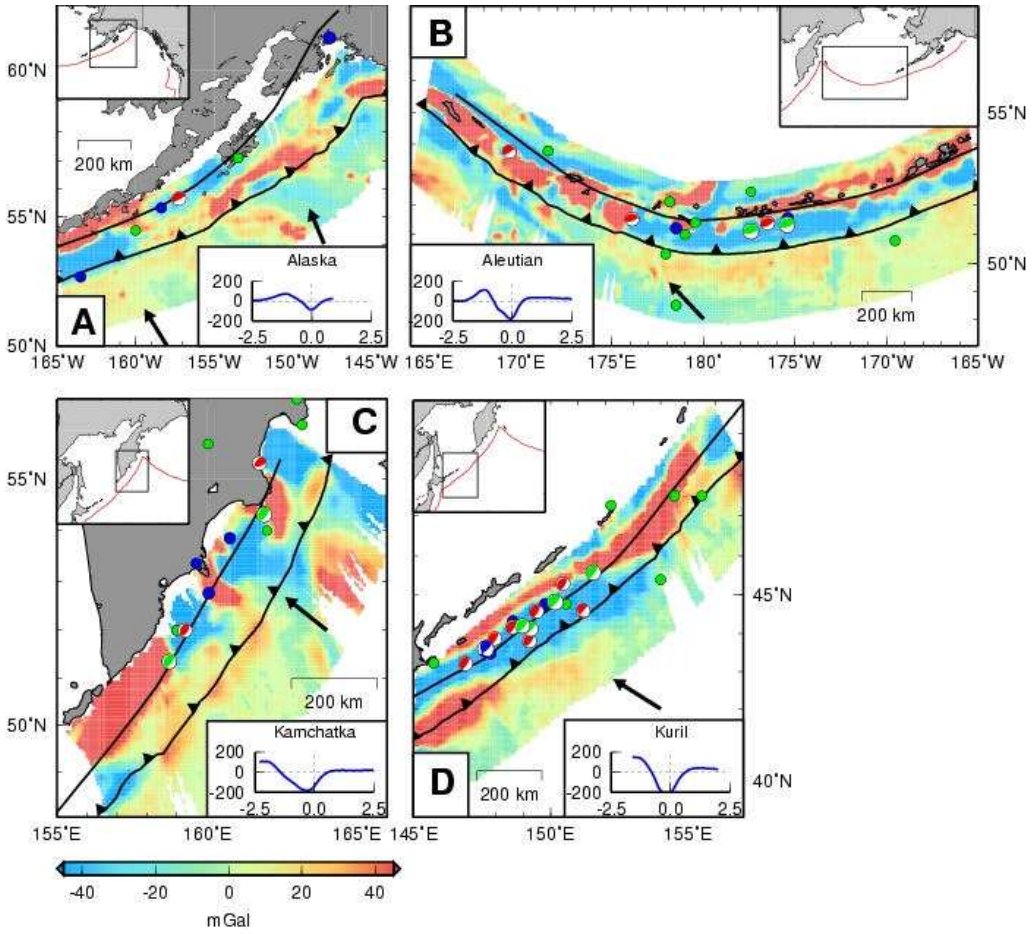

Figure 1.5: (A) Alaska (B) Aleutian (C) Kamchatka (D) Kurile subduction zones, respectively. The average trench-normal gravity profile calculated for the region shown in the upper insets is shown in the lower insets, whose x-axis is trench-normal distance in degrees and the y-axis is gravity in mGal. The color bar shows the amplitude of the free-air gravity anomaly. Subduction zone earthquakes from the ISC (1900-1976) with $M_w = 7.5$ and Harvard CMT (1976-2001) catalogues with $M_w = 7.0$, are plotted as solid circles and moment tensors, respectively. Trench location (S11) and 50-km slab iso-depth contour (S12) are indicated by the barbed and thick black lines, respectively. Directions of relative plate convergence (S13) are shown as arrows.

1.2.3 Construction of TPTA

As with the TPGA, we bin the TPTA in four groups with equal total area in a given range of TPTA. We note that ETOPO-5 data is not as highly resolved as the gravity data (S8, S9). Gravity data is higher resolution with 30 sec grid spacing while ETOPO-5 data is with 5 min grid spacing. Track lines used to construct ETOPO-5 are denser in along the convergent plate boundary (refer to Fig. 1 in S9,) the error due to gridding is not likely to be significant at the scales of interest (several tens of kilometers).

1.2.4 Moment release versus TPGA

We first consider the distribution of moment for individual events versus TPGA (Fig. 1.6).

For events in either the CMT or the ISC catalogues, no great earthquakes ($M_w >$ 8.0) occur in areas with positive TPGA ($>$ 40 mGal). Given the large number of events involved, we find it useful also to consider the distribution of cumulative moment (Fig. 1.7).

We observe that about 80% of the cumulative moment is produced in 30% of total area of subduction zone with TPGA less than -30 mGal, while less than 20% of cumulative moment is produced in the 70% of the area of subduction zone with TPGA greater than -30 mGal. The total cumulative seismic moment is dominated by the three largest earthquakes of the 20th century. When excluding the three largest earthquakes, we find that about 45% of the remaining total seismic moment is produced in about 25% of the total area of subduction zone with highly negative TPGA (< -40 mGal).

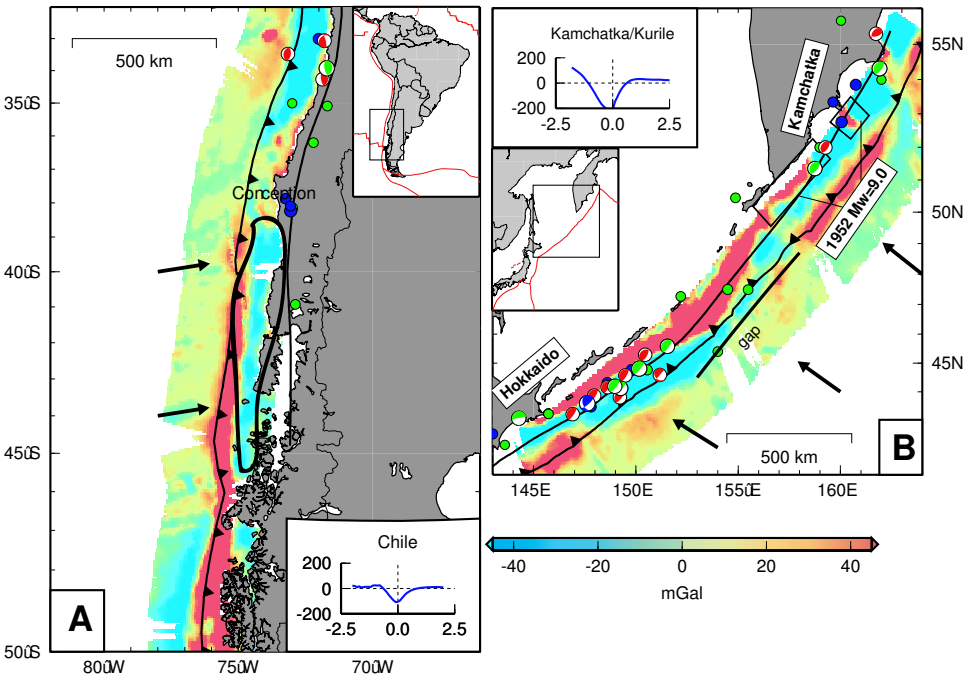

Figure 1.6: (A) Observed TPGA in the Southern Chile subduction zone. Average trench-normal profile is computed in region (I) shown in Fig. 1.4. Black solid line represents 10 m contour of co-seismic slip of the 1960 Chilean earthquake (S14). (B) Observed TPGA in Kamchatka-Kurile. Previously documented seismic gap (S15) is shown by a black bar. Areas with large moment released during 1952 great earthquakes are indicated in black boxes (S16). Symbol descriptions follow Fig. 1.5.

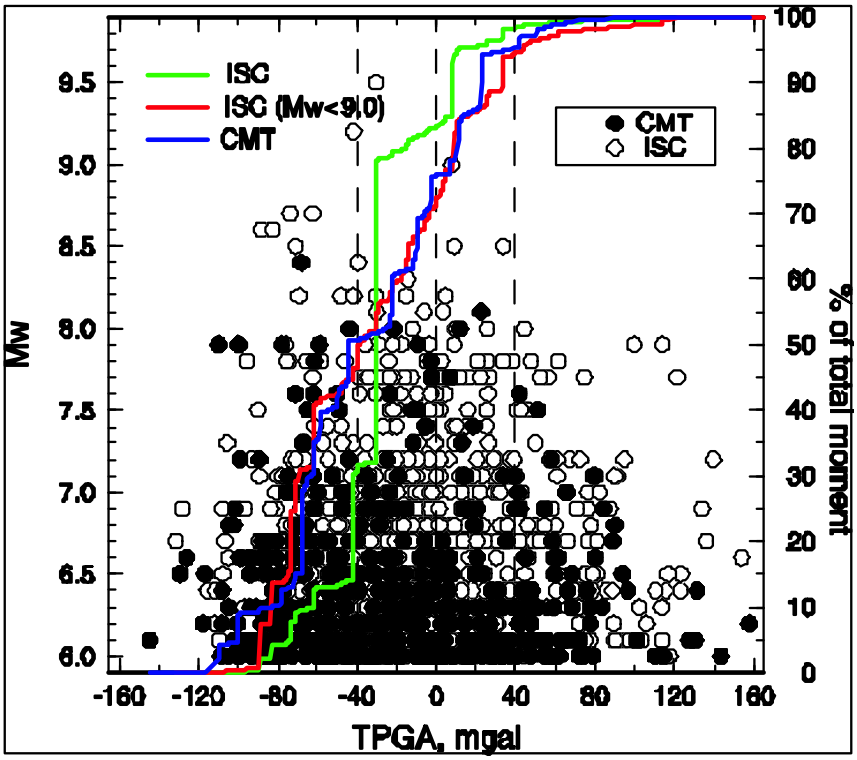

Figure 1.7: Solid and open circles indicate data from CMT and ISC catalogue, respectively. Cumulative precent of total seismic moment with respect to TPGA for the entire ISC catalogue, ISC catalogue with $M_w < 9.0$, and CMT catalogue are shown with green, red, and blue lines, respectively. Mean TPGA for the three giant events are calculated using available slip models (S14, S16, S17). Dashed lines indicate the values of TPGA that divide the total area of subduction zone interface into four bins of approximatedly equal area.

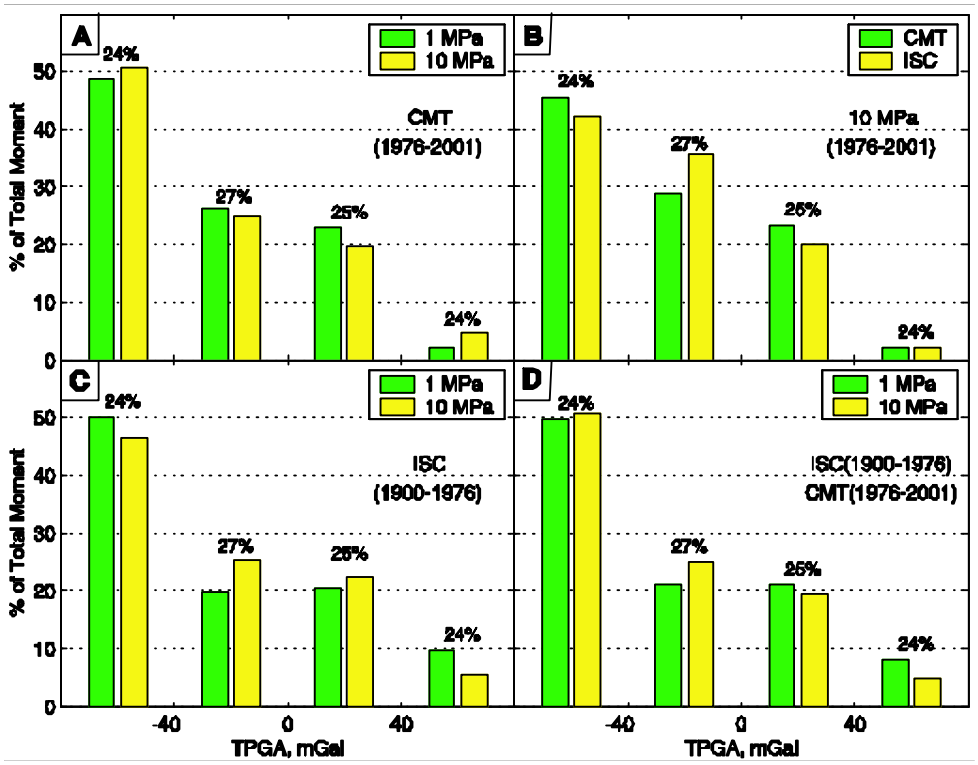

Figure 1.8: (A) All CMT events (1976-2001) with $M_w = 6.0$. (B) All events with $M_w = 6.0$ located in both CMT and ISC catalogues (1976-2001). A 10 MPa stress drop is assumed when estimating slip area. (C) All ISC events in 1900-1976. (D) All CMT events (1976-2001) and ISC events (1900-1976).

1.2.5 Robustness of correlation between TPGA and seismic moment

Despite the inherent limitations of the global earthquake catalogues, such as event mislocation and incompleteness, the correlation between TPGA and the occurrences of large earthquakes does not depend on the assumed magnitude of the stress drop, which catalog is used, or how seismic moment is distributed over a given earthquake's fault area (Fig. 1.8 and Fig. 1.9).

In addition, Monte Carlo permutation tests (S10) indicate that the difference in total seismic moment between areas with strongly negative TPGA ($<$ -40 mGal) and areas with strongly positive TPGA ($>$ 40 mGal) is significant at a 95% confidence level.

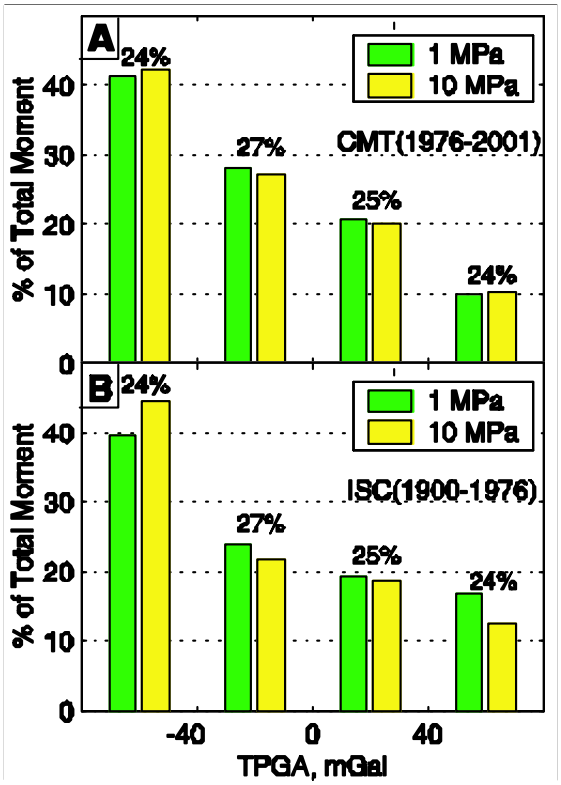

Figure 1.9: Here we do not calculate the average TPGA for a given earthquake. Instead, the plate interface is pixelated into small (about 0.1 x 0.1 deg) cells of constant TPGA, and the seismic moment for a given earthquake is evenly distributed onto the cells within the estimated fault area. We then form the histogram by evaluating the total distributed moment in cells lying within a given range of TPGA. (A) All CMT events (1976-2001) with $M_w = 6.0$. (B) All ISC events from 1900-1976. The percent of the slab interface area represented by each bin is shown above each bar.

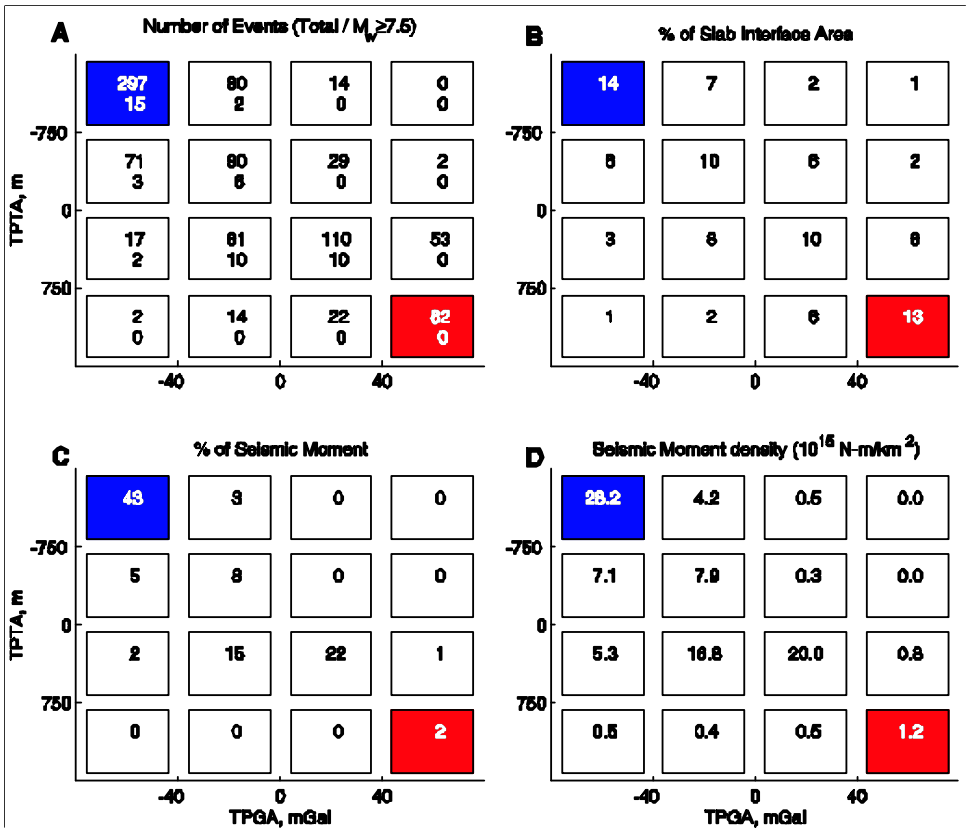

Figure 1.10: Seismic moment release vs. TPGA and TPTA using all CMT events with Mw=6.0 assuming a 1 MPa stress drop to calculate the slip area. (A) Number of event (B) percent of slab interface area (C) percent of seismic moment (D) seismic moment density.

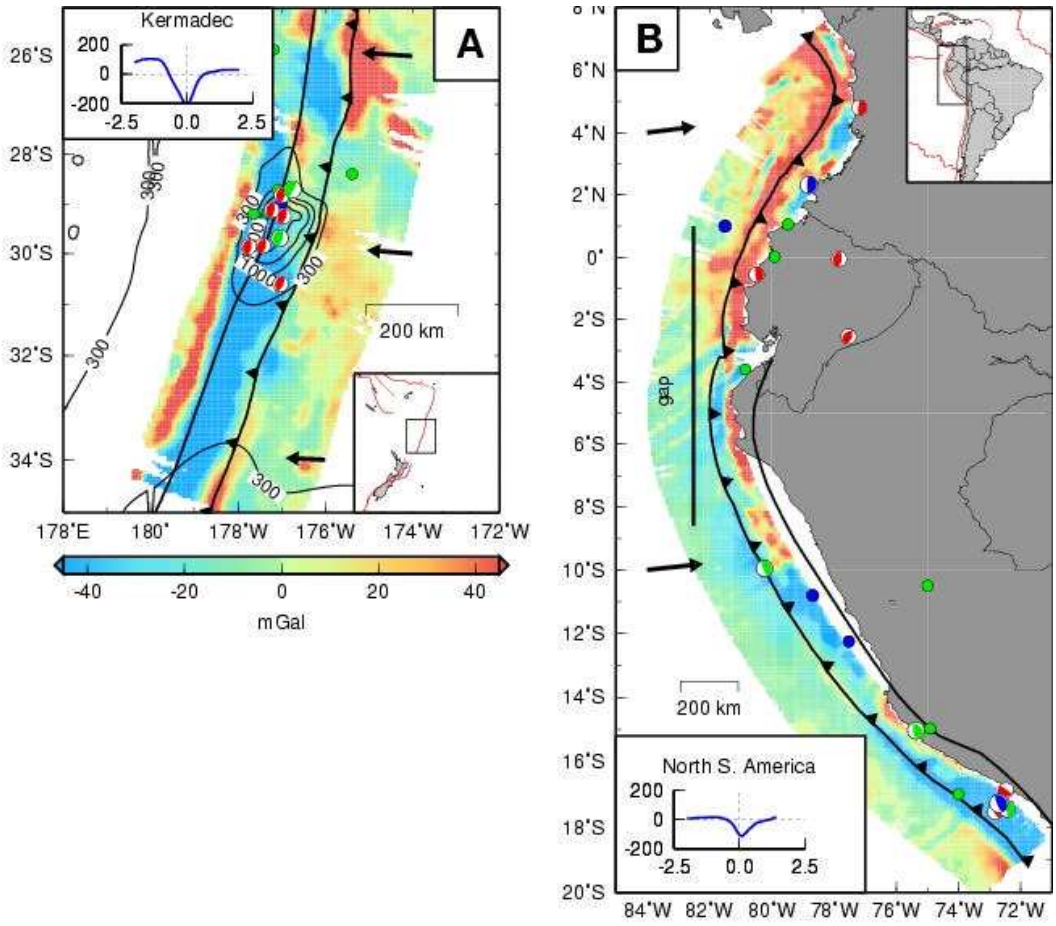

Figure 1.11: (A) Observed TPGA in Kermadec. The average trench-normal profile is computed in region H shown in Fig. 1.4. Contours indicate sediment thickness (S18) in meters. (B) Observed TPGA in northern S. America. The extent of previously determined seismic gap (S15) is shown with a black bar. Symbol descriptions follow Fig. 1.5.

1.3 References

1. B. H. Hager, R. J. O'Connell, A. Raefsky, Tectonophysics. 99, 163 (1983).

2. S. Zhong, M. Gurnis, J. Geophys. Res. 99, 15683 (1994).

3. M. I. Billen, M. Gurnis, Earth Planet. Sci. Lett. 193, 227 (2001).

4. S. Zhong, M. Gurnis, Geophys. Res. Lett. 19, 1891 (1992).

5. S. J. H. Buiter, R. Govers, M. J. R. Worterl, Geophys. J. Int. 147, 415 (2001).

6. S. Wdowinski, J. Geophys. Res. 97, 17651 (1992).

7. R. Cattin, H. Lyon-Caen, J. Chery, Geophys. Res. Lett. 24, 1563 (1997).

8. Shemenda, A. I. in Subduction: insight from physical modeling, Modern approaches in Geophysics, vol. 11, 215pp (1994).

9. D. T. Sandwell, W. Smith, J. Geophys. Res. 102, 10039 (1997).

10. We restrict ourselves to this global dataset to maintain geographic uniformity of the analysis. This restriction implies that we consider only TPGA in offshore areas.

11. Materials and methods are in Section 1.2.

12. We note that the subduction interface can be conveniently classified using TPGA into four about equal area bins associated with the TPGA ranges of less than -40 mGal, -40 to 0 mGal, 0 to 40 mGal and greater than 40 mGal, respectively.

13. A. M. Dziewonski, T. A. Chou, J. H. Woodhouse, J. Geophys. Res. 86, 2825 (1981).

14. E. R. Engdahl, D. R. Van der Hilst, R. P. Buland, Bull. Seis. Soc. Am. 88, 722 (1998).

15. When using these catalogs, we attempt to use only fore-arc thrust events between 0 and 50 km depth in the Benioff zone, where the plate interface is probably coupled.

16. L. Ruff, H. Kanamori, Phys. Earth Planet. Inter. 31, 202 (1983).

17. J. Johnson, Adv. in Geophys. 29, 1 (1998).

18. S. Beck, D. H. Christensen, J. Geophys. Res. 96, 2205 (1991).

19. S. E. Barrientos, S. N. Ward, Geophys. J. Int. 103, 589 (1990).

20. J. M. Johnson, K. Satake, Pure Apply. Geophysics. 154, 541 (1999).

21. National Geophysical Data Center, ETOPO-5 bathymetry/topography data,

Data Announc. 88-MCG-02, Natl. Oceanic and Atmos. Admin. U. S. Dept. Commer., Boulder, Colo. (1988).

22. H. J. Fletcher, J. Beavan, J. Freymuller, L. Gilbert, Geophys. Res. Lett. 28, 443 (2001).

23. C. J. Zweck, J. Freymuller, S. C. Cohen, J. Geophys. Res. 107, 10.1029/2001JB000409 (2002).

24. K. M. Larson, M. Lisowski, Geophys. Res. Lett. 21, 489 (1994).

25. J. T. Freymuller, J. Bevan, Geophys. Res. Lett. 26, 3233 (1999).

26. Y. Sugiyama, Geofisica Internacional 33, 53 (1994).

27. National Geophysical Data Center, Total Sediment Thickness of the World's Oceans & Marginal Seas, Natl. Oceanic and Atmos. Admin. U. S. Dep. Commer., Boulder, Colo. (1996).

28. K. Mogi, Bull. Earthquake Res. Inst. 47, 429 (1969).

29. L. Ruff, B. W. Tichelaar, What controls the seismogenic plate interface in subduction zones? Subduction: Top to Bottom, AGU Geophysical Monograph Volume 96, edited by Gray E. Bebout, David W. Scholl, Stephen H. Kirby, and John P. Platt, pp. 105-111 (1996).

30. M. E. Pritchard, M. Simons, M., P. A. Rosen, S. Hensley, F. H. Webb, Geophys. J. Int. 150, 362 (2002).

31. Y. Tonioka, K. Satake, Earth Planet Space 53, 235 (2001).

32. J. Kelleher, W. McCann, J. Geophys. Res. 81, 4885 (1976).

33. C. Marone, Annu. Rev. Earth Planet. Sci. 26, 643 (1998).

34. S. Uyeda, H. Kanamori, J. Geophys. Res. 84, 1049 (1979).

35. H. Kanamori, Annu. Rev. Earth Planet. Sci. 14, 293 (1986).

36. C. H. Scholz, J. Campos, J. Geophys. Res. 100, 22103 (1995).

37. T. Lay, H. Kanamori, L. Ruff, Earthquake Pred. Res. 1, 1 (1982).

38. S. P. Nishenko, Pure Apply. Geophys. 135, 169-259 (1991).

39. Y. Y. Kagan, D. Jackson. J. Geophys. Res. 100, 3943-3959 (1995).

40. National Geophysical Data Center, Global Relief data (CD-ROM). World Data Center for Marine Geology and Geophysics, Boulder, Colo. (1993).

41. O. Gudmundsson, M. Sambridge, J. Geophys. Res. 103, 7121 (1998).

42. C. DeMets, R. G. Gordon, D. F. Argus, Geophys. Res. Lett. 21, 2191 (1994).

S1. T. Lay, T. Wallace, in Modern Global Seismology, 521pp (1995).

S2. H. Kanamori, D. L. Anderson, Bull. Seis. Soc. Am. 65, 1073-1095 (1975).

S3. P. Chen, H. Chen, Tectonophysics, 166, 53-72 (1989).

S4. H. Kanamori, Tectonophysics, 93, 185-199 (1983).

S5. L. Ruff, H. Kanamori, Phys. Earth Planet. Inter. 31, 202 (1983).

S6. S. E. Barrientos, S. N. Ward, Geophys. J. Int. 103, 589 (1990).

S7. J. M. Johnson, K. Satake, Pure Apply. Geophysics. 154, 541 (1999).

S8. National Geophysical Data Center, ETOPO-5 bathymetry/topography data, Data Announc. 88-MCG-02, Natl. Oceanic and Atmos. Admin. U. S. Dep. Commer., Boulder, Colo. (1988).

S9. W. H. F. Smith, J. Geophys. Res. 98, 9591 (1993).

S10. E. L. Lehmann, in Testing Statistical Hypothesis. Wiley publications in statistics, 369 pp (1959).

S11. National Geophysical Data Center, Global Relief data (CD-ROM). World Data Center for Marine Geology and Geophysics, Boulder, Colo. (1993).

S12. O. Gudmundsson, M. Sambridge, J. Geophys. Res. 103, 7121 (1998).

S13. C. DeMets, R. G. Gordon, D. F. Argus, Geophys. Res. Lett. 21, 2191 (1994).

S14. S. E. Barrientos, S. N. Ward, Geophys. J. Int. 103, 589 (1990).

S15. T. Lay, H. Kanamori, L. Ruff, Earthquake Pred. Res. 1, 1 (1982).

S16. J. M. Johnson, K. Satake, Pure Apply. Geophysics. 154, 541 (1999).

S17. L. Ruff, H. Kanamori, Phys. Earth Planet. Inter. 31, 202 (1983).

S18.National Geophysical Data Center, Total Sediment Thickness of the World's Oceans & Marginal Seas, Natl. Oceanic and Atmos. Admin. U. S Dep. Commer., Boulder, Colo. (1996).

Chapter 2

Excitation of Earth's Free Oscillations by the 26 December 2004 Sumatra-Andaman Earthquake

Abstract

At periods greater than 1000 sec, Earth's free oscillations excited by the 26 December 2004 great Sumatra-Andaman earthquake have anomalously large amplitude when referenced to the Harvard CMT fault mechanism (1), which is estimated from 300−500 sec surface waves (2). On a steeper fault with a time-dependent rupture model that matches seismic body and surface waves in greater detail (3), free oscillation amplitudes can be approximated with a seismic moment ($M_o = 6.5 \times 10^{22}$ N-m) that corresponds to moment-magnitude $M_w = 9.15$, close to the geometric mean of initial estimates from surface waves ($M_w = 9.0$) and the mode ${}_0S_2$ ($M_w = 9.3$). With a rupture duration $\tau = 600$ seconds, the fault-rupture models do not represent well geodetic observations. It argues for larger fault displacement beneath the Nicobar and Andaman Islands (4). As a second author of this paper, I have contributed to most of the source modeling and figures (Fig. 2.2, Fig. 2.3A, Fig. 2.4, Fig. 2.6-Fig. 2.8). *(Originally published Park et al., Science, 308, 1139-1144, 2005)*

2.1 Introduction

The 26 December 2004 Sumatra-Andaman earthquake delivered a hammer blow to our planet, exciting a plethora of vibrational free oscillations that, at periods T>1000 s, remained observable for weeks in broadband seismic data from global networks. The frequencies and decay rates of Earth's free oscillations offer strong constraints on our planet's interior composition, mineralogy, and dynamics (5−14), so analysis of long-period seismic data from this event should offer new perspectives on Earth structure. In this report we discuss how seismic free oscillations also provide information on the remarkable size and duration of this earthquake.

Because Earth is approximately spherical, the geographical patterns of its free vibrational modes can be expressed in terms of the angular harmonics $Y_{lm}(\theta, \phi)$ and their vector gradients, where l is the angular degree, m is the azimuthal order, θ is colatitude and ϕ is longitude. On a simple spherical planet (15), the free oscillations follow either a spheroidal (S) or toroidal (T) vibrational pattern and have spectroscopic notation ${}_nS_{lm}$ and ${}_nT_{lm}$, where n is the radial overtone number (Fig. 2.1).

For a spherical reference model, all $2l+1$ vibrations of ${}_nS_{lm}$ and ${}_nT_{lm}$, have identical frequency. On the real Earth, departures from the symmetries of a spherical reference model cause its free oscillations to couple, hybridize and suffer fine-scale splitting of their vibrational frequencies (16−19). Frequency splitting of free oscillations with periods T>1000 s is caused mainly by Earth's rotation, similar to Zeeman splitting of electron energies in an external magnetic field (20, 21).

Earth's free oscillations were first reported after Fourier analysis of hand-digitized analog seismic records of the megathrust earthquakes of the middle 20th century (22-25), particularly the 22 May 1960 Chilean earthquake (M_w = 9.5). These huge events saturated most seismometers of the time, rendering many hours of data unusable. Frequency estimates from smaller, deeper earthquakes, more amenable to hand-digitization and Fourier analysis, led to accurate spherical-reference models for our planet's interior (5). Detailed study of free oscillation attenuation, frequency splitting, and modal coupling was made feasible by digital recording (6, 7, 26, 27)

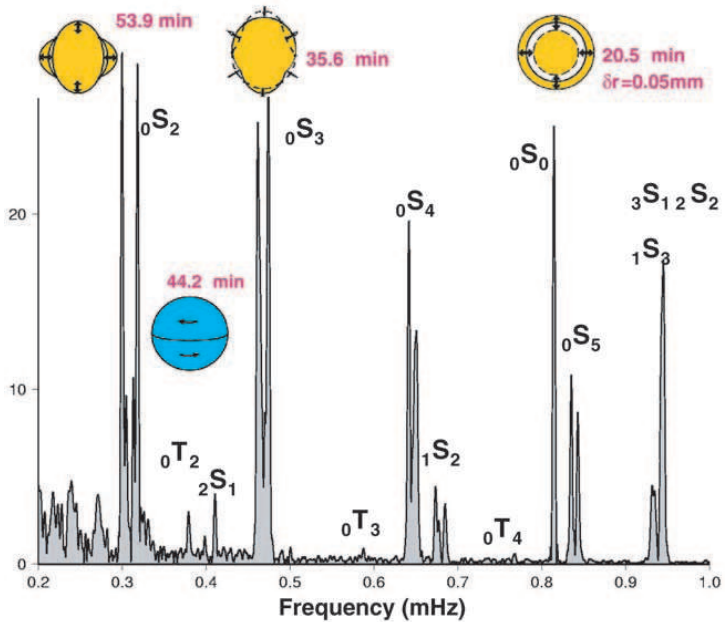

Figure 2.1: Schematic of the motion of free oscillations ${}_0S_2$, ${}_0T_2$, ${}_0S_3$ and ${}_0S_0$, superimposed on a spectrum computed from vertical seismic motions recorded at Station CAN (Canberra, Australia) of the Geoscope Network. For comparison, Fig. 2.9 in section 2.5 plots the acceleration spectrum from the superconducting gravimeter collocated with CAN.

and by the advent of the Federation of Digital Seismic Networks (FDSN) with high-dynamic range induction-feedback sensors capable of recording faithfully the seismic waves from great earthquakes (28).

2.2 Broadband seismography data

The 2004 Sumatra-Andaman earthquake tested broadband seismographic technology on a global scale. Peak ground motions exceeded 1 cm at all locations on Earth's solid surface (29). In one portion of the FDSN, 88% of the 125 stations of the Global Seismographic Network (GSN), operated directly by the U. S. Geological Survey and the IDA Project of the University of California, San Diego (30), recorded data without interruption or distortion (31). Stations of the Geoscope network (32) had similar success.

In all, data records from more than 400 FDSN stations were of sufficient quality to observe Earth's free oscillations with unprecedented signal-to-noise ratios. A broad distribution of stations facilitates using $Y_{lm}(\theta, \phi)$-weighted stacks of data spectra to isolate individual Earth vibrations (Fig. 2.10, Section 2.5). The recent installation of a broadband seismometer in the South Pole Quiet Zone provides natural isolation of the $m = 0$ singlets of long-period modes (Fig. 2.2).

Free oscillations can also be sought in complementary observations (Fig. 2.3) from strainmeters and tiltmeters (33-35), from superconducting gravimeters (36-38), and from continuously-recording GPS receivers (39,40). Superconducting gravimeter data offers an important calibration for seismometer data at periods T>1000 s (41). The amplitude of the "breathing mode" ${}_0S_0$ is geographically constant to high accuracy; station-by-station comparisons of its amplitude in data from the IDA network suggest that a significant minority of seismometers suffer 5-10% deviations from their nominal responses (31).

The largest earthquakes offer the most penetrating and long-lasting seismic probes of Earth's deep interior, revealing behavior predicted by theory, but only rarely observed above ground noise. The coupling between spheroidal and toroidal modes

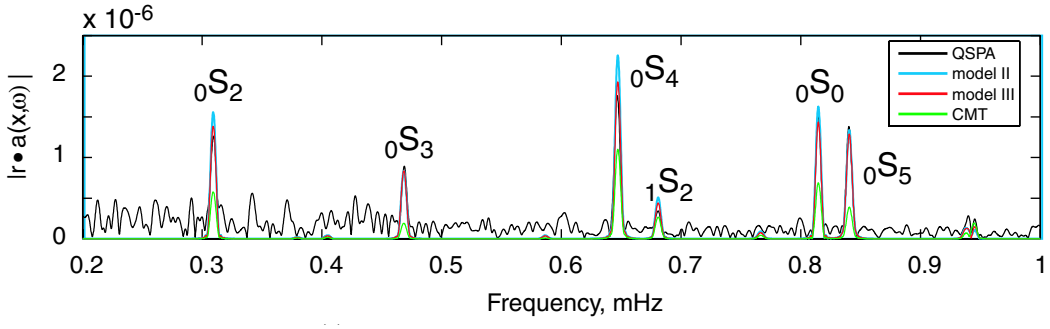

Figure 2.2: Free-oscillation spectra for GSN station QSPA, whose sensor lies within an ice borehole in the Quiet Sector of the South Pole Station. Only m=0 free oscillations are nonzero at Earths poles, leading to sharply-defined single resonance peaks for modes ${}_nS_l$ and ${}_nT_l$ with period T $>$ 1000 s. A vertical-motion data series of 106 hours was analyzed.

associated with Earth's Coriolis force causes them to form hybrid vibrational patterns. The hybridized toroidal modes are predicted to acquire a vertical vibrational component, a feature nominally restricted to spheroidal modes. Although this behavior is readily observable for mode pairs ${}_0S_l - {}_0T_{l+1}$ in the 300-500 s period range that are close in frequency (26,27), at frequencies below 1 mHz the coupling is weaker and was not observed with seismometers before the 2004 Sumatra-Andaman earthquake (Fig. 2.1, ref. 42 and Fig. 2.11 in section 2.5).

The geometry of low-degree modes allows us to constrain the long-period centroid of the earthquake (7,22). For a centroid at the equator, excitation of the $m \pm 1$ vibrations of the mode ${}_0S_2$ would be zero for an earthquake on the east-dipping Sumatra-Andaman thrust fault. The amplitude of the $m = -1, +1$ vibrations, of ${}_0S_2$ relative to the $m = -2, 0$, and $+2$ vibration, indicates how far northward the Sumatra-Andaman earthquake ruptured (Fig. 2.4). The event hypocenter and CMT location lie at $3.2°N$ and $3.1°N$, respectively, displaced east-west by nearly 200 km. The relative excitation of the $m = \pm 1$ vibrational modes of ${}_0S_2$ is significantly underpredicted by this location centroid. Better agreement is obtained for a seismic source centroid closer to $7.5°N$, suggesting a source process that extends into the northern half of the aftershock zone.

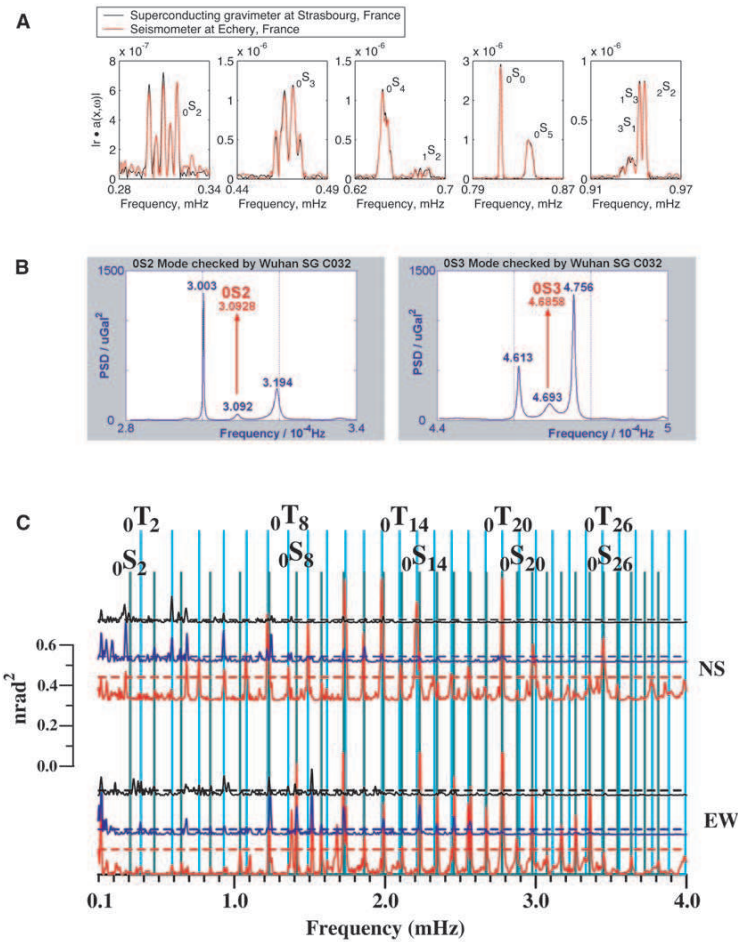

Figure 2.3: (a) Super-conducting gravimeter (Strasbourg, France) and nearby vertical-component seismic data (Echery, France) have almost identical spectra. A Hann taper has been applied to the 230-hour time series from both instruments prior to discrete Fourier transformation, (b) Burg-method spectrum estimates of data from the C032 superconducting-gravimeter (SG) at Wuhan Station, Peoples Republic of China, (c) Blackman-Tukey-tapered spectral estimates of horizontal-component data from the Grotta Gigante pendulum tiltmeter, computed on three sliding time-windows of 24 hours each, shifted by 12 hours. The red, blue, and black lines pertain to the windows starting at days 361.25, 361.75, and 362.25 of 2004, respectively. North-south motion is shown in top three traces; east-west motion is shown in the bottom traces. The broken line indicates the 95% confidence level that a spectral peak is significant.

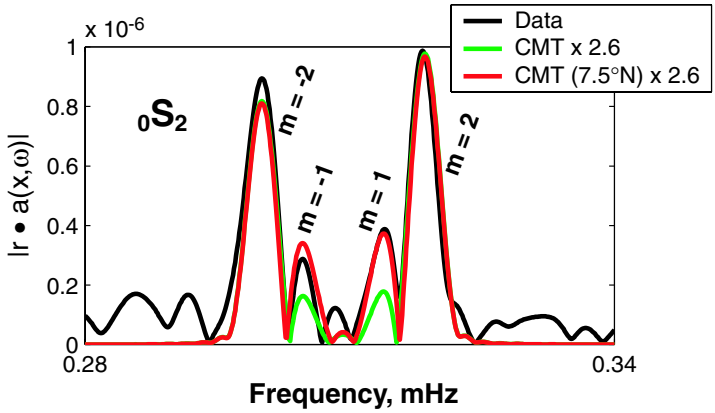

Figure 2.4: Black: data. Red: prediction for the Harvard CMT mechanism and location but at 2.6 times larger scalar moment. Note how the $m = 1$ and $m = -1$ singlets are too small, indicating that the CMT centroid is too close to the equator. Green: prediction from 2.6 times the CMT moment but with a centroid location at $7.5°N$, which improves the fit to the $m = 1$ and $m = -1$ singlets. A Hann taper has been applied to the 144-hour time series starting from the origin time of this earthquake.

2.3 Earthquake size and duration

Since the late 1970s seismologists have estimated magnitude M_w for large earthquakes in terms of the seismic moment M_o (46). As a measure of the average displacement integrated over the ruptured fault zone, seismic moment M_o is associated with its zero frequency behavior. It is therefore logical to estimate M_o from the amplitudes of the gravest Earth free oscillations, such as the modes ${}_0S_2$, ${}_0S_3$, ${}_0S_4$, ${}_0S_0$, and ${}_1S_0$. For nearly all earthquakes these modes are excited too weakly for direct observation, but the Sumatra-Andaman event was different. The "football mode" ${}_0S_2$, the free oscillation with the longest observed period (54 minutes), is expressed strongly in vertical-component spectra computed from a large proportion of individual stations, as are many of the shorter-period modes. The amplitudes of several spheroidal free oscillations with periods T > 1000 s were a factor of 1.25 to 2.6 larger than predicted by the Harvard CMT source (1,2), reaching a maximum for the mode ${}_0S_2$ (Fig. 2.4 and Fig. 2.5).

If this amplitude is related to fault motion with the same geometry as the CMT

solution, i.e., thrusting on a shallow-dipping fault (8° dip), the estimated earthquake magnitude M_w increases from 9.0 to 9.3.

Source spectral amplitude is larger at long period for earthquakes with long time duration. If seismic rupture progresses at a constant rate for a finite duration τ, from a sharp onset to an equally abrupt termination, the source spectrum $M(f) = Mo(\sin \pi f\tau)/(\pi f\tau)$ a function of cycle frequency f (47). The logarithm of $M(f)$ exhibits a low-frequency plateau that transitions to a power-law slope at a corner frequency $f_c = \frac{1}{\pi\tau}$. Fig. 2.5 graphs the source spectra implied by several spheroidal modes against $M(f)$ source spectra for constant-rupture durations $\tau = 800$ s and $\tau = 320$ s. Modal amplitudes do not follow the predictions of a constant-rate source spectrum, suggesting a variable rupture-propagation rate. For example, the rupture of two large fault segments with different orientations, onset times and durations would cause spectral interference at long period. Such complexity aside, the trend of modal amplitudes is consistent with a rupture duration $\tau \leq 800$ s.

The initial phase of ${}_0S_0$, relative to the earthquake onset, supports the inference of long source duration, τ. The initial phase of a free oscillation of period, T, aligns with the time centroid of the rupture process if the rupture duration is relatively small, i.e., $\tau \ll T$. Phase cancellation damps the modal excitation if $\tau \geq T/2$, and the relation of modal initial phases with the source time centroid becomes complicated. We estimate the initial phase of ${}_0S_0$ to average $65° - 66°$ in the Global Seismographic Network and to average 61° over ten records from the Geoscope network (Fig. 2.12). The initial displacement of ${}_0S_0$ is positive (0° phase), so this suggests a time centroid delayed 205 to 225 s relative to the earthquake onset. Rupture duration τ would be between 400 and 450 s if rupture rate were constant. The initial phase of ${}_1S_0$ is 115.7° averaged for ten Geoscope stations, consistent with a time centroid of 197 s. Variable rupture rate will cause scatter in time centroids estimated from different modes.

Free-oscillation observations constrain the Sumatra-Andaman earthquake source, but the constant-rupture model is too simple. A complex earthquake process is suggested by a number of observations, e.g., large bursts of high-frequency seismic radiation occur in the first 200 s of rupture (3, 48); aftershock locations span a 1300 km

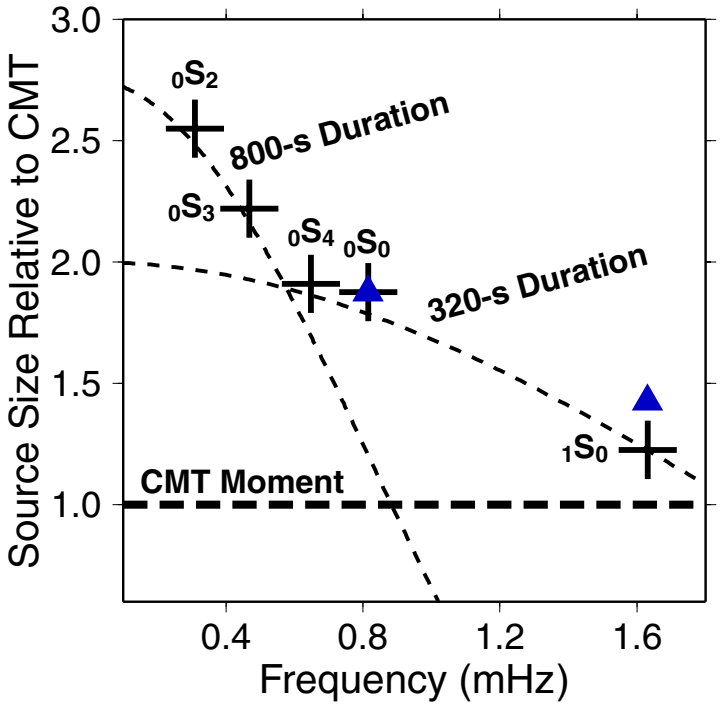

Figure 2.5: The measured amplitudes of several long-period free oscillations, expressed in terms of the seismic moment required for excitation by the shallow-thrust fault geometry of the Harvard CMT solution. Crosses indicate free oscillation amplitudes measured on data from GSN stations; triangles are estimated independently using data from Geoscope stations. The largest amplification is associated with the mode ${}_0S_2$, whose apparent moment is roughly 2.6 times the CMT moment estimated from 300-500 s surface waves. Superimposed on the measurements are theoretical source spectra for constant-rupture sources of duration τ, which follow $\frac{\sin(\pi f \tau)}{\pi f \tau}$ dependence. Deviations in source geometry and fluctuations in rupture rate would cause the source spectrum to depart from this simple model. Nevertheless, modal excitation suggests that the Sumatra-Andaman earthquake involved fault slip on more than one time scale.

segment of plate margin (4), but in the northern 400 km of the zone the aftershocks commence some 85 minutes after rupture onset (49); substantial surface wave directivity at periods approaching 1000 s (3); the dip of the Sumatra-Andaman megathrust in its northern half tends to exceed the 8° dip of the Harvard CMT source mechanism (4); back-arc spreading in the Andaman Sea may have promoted the expression of strike-slip motion as the rupture progressed north (4); modeling suggests that the northern third of the fault zone contributed little to the observed tsunami (4). Many factors suggest that fault motion was larger and faster in the south of the fault zone, where rupture began, and was smaller and slower in the north.

2.4 Modeling the rupture

Drawing on inferences made from these data, we consider here two finite-rupture models based on body and surface waves (Models II and III of reference 3) in which rupture has longer duration (600 s versus 300 s), longer length (1300 km versus 400 km) and larger moment (6.5×10^{22}N-m versus 4.0×10^{22}N-m) than inferred from the CMT solution (Fig. 2.6).

Both models prescribe a spatially varying fault geometry that is, on average, steeper than the CMT solution. A steeper fault is more efficient at exciting the long-period modes, and therefore the finite rupture models can greatly improve the match between predicted and observed modal amplitudes with a far smaller seismic momemt (M_o) than inferred by (2). Model III, which prescribes a peak rate of rupture propagation somewhat earlier than Model II, is more successful at predicting the absolute value of modal vertical-component spectral peaks, typically with average misfit less than 10%, depending on the mode (Fig. 2.7 and Table 2.1 in section 2.5).

Despite the rough success of a single seismic rupture model across the entire seismic spectrum, geodetic evidence for a slow component of Sumatra-Andaman displacement cannot be dismissed. Fault slip of $\sim$ 1 hour in duration, as suggested by tsunami modeling for the Nicobar-Andaman fault segment (4), would excite seismic free oscillations inefficiently due to phase cancellation. Its signature would be

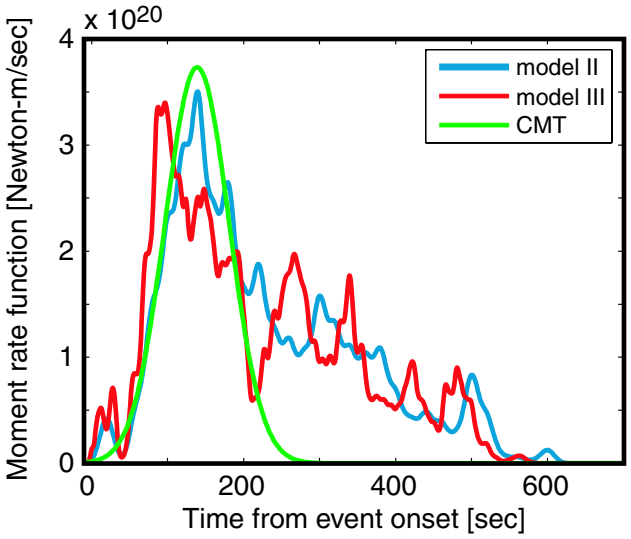

Figure 2.6: Moment-rate functions (MRFs) for the 26 December Sumatra-Andaman earthquake. The MRF associated with the Harvard CMT is given by the green line, the MRF of finite-fault inversion II of (3) is denoted by the blue line, and the MRF of finite-fault inversion III of (3) is denoted by the red line.

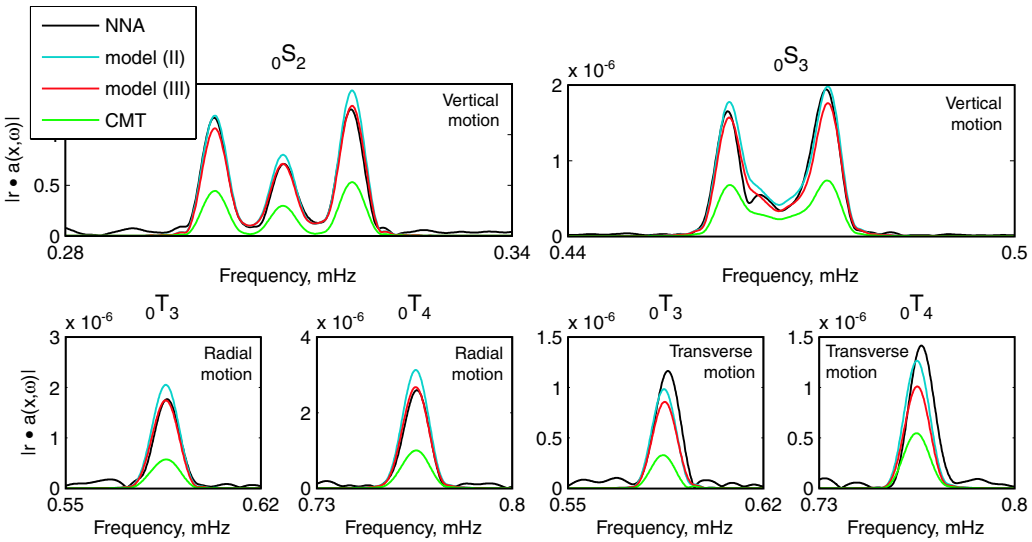

Figure 2.7: Comparison of data (NNA, at Nana, Peru) and synthetics from various models. Low order spheroidal modes ${}_0S_2$, ${}_0S_3$ at vertical component and toroidal modes ${}_0T_3$, ${}_0T_4$ at horizontal component are shown above. A Hann taper is applied to 144-hr time series of vertical motion prior to discrete Fourier transformation. Similar tapering was performed on 44-hr time series of radial and transverse horizontal motion prior to discrete Fourier transformation.

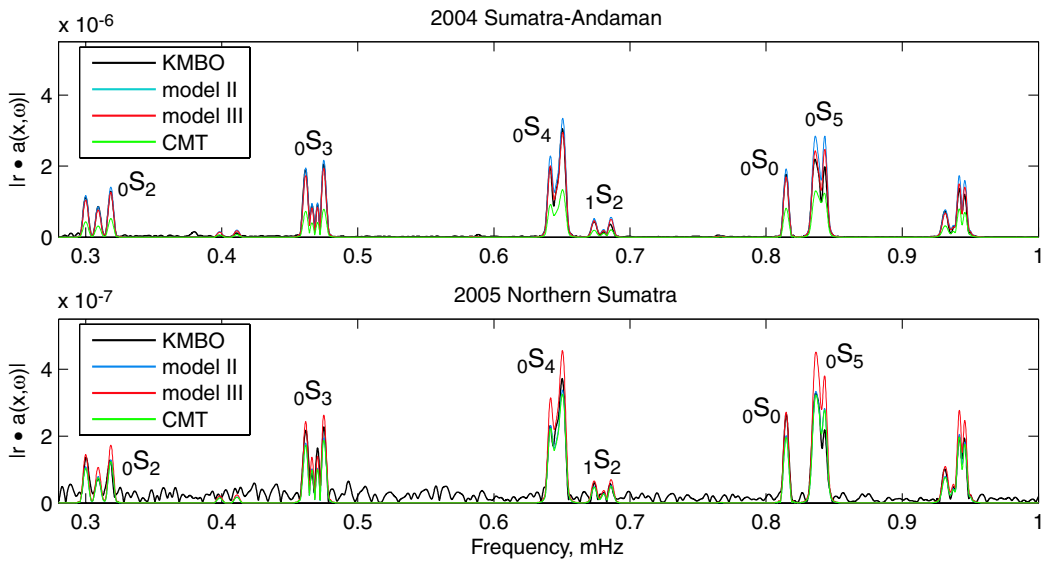

Figure 2.8: Spectrum comparison for the 26 December 2004 Sumatra-Andaman and 28 March 2005 Northern Sumatra earthquakes, using 144-hour records of vertical motion recorded at station KMBO (Kilima Mbogo, Kenya). Spectral predictions of the Harvard CMT solutions are graphed, as well as spectra predicted from finite-rupture models from (3). Note the greater success of the CMT solution for the 2005 event, consistent with a less complex rupture process.

expressed as a complex pattern of modal amplitude and phase anomalies. Modal spectra for the 2004 Sumatra-Andaman earthquake are more difficult to predict with simple parameterized rupture models than modal spectra from the 28 March 2005 Northern Sumatra earthquake ($M_w = 8.6$), despite higher signal-to-noise ratios for the larger event (Fig. 2.8). If amplitude and phase misfits leave unexplained 10% or more of the long period free-oscillation amplitudes of the 2004 event, slow fault motion equivalent to magnitude at least $M_w = 8.4$ would be possible, a geophysical event itself larger than any earthquake between 1965 and 2001.

For both Sumatran earthquakes, modal amplitude and phase anomalies will constrain any additional long-term slip. In this context, the calibration and long-term resilience of global seismographic networks is paramount. A future megathrust earthquake ($M_w \geq 9.0$) is inevitable somewhere along Earth's plate boundaries, but may not occur for a decade or more, after today's seismometers have begun to age and perhaps fail. The broadband vault seismometer most suitable for today's global seis-

mographic networks, the Streckeisen STS-1 (52), is no longer manufactured. It is important for the international seismological community to consider designing the next-generation broadband seismic sensor.

2.5 Supplementary material

Here we present some graphical material to complete the exposition of the main manuscript.

A Note on Mode Coupling at Periods T $<$ 1000 s. The largest earthquakes offer the most penetrating and long-lasting seismic probes of Earth's deep interior, revealing behavior predicted by theory, but only rarely observed above ground noise. The coupling between spheroidal and toroidal modes associated with Earth's Coriolis force causes them to form hybrid vibrational patterns. The hybridized toroidal modes are predicted to acquire a vertical vibrational component, a feature nominally restricted to spheroidal modes. Although this behavior is readily observable for mode pairs ${}_0S_l$ ${}_0T_{l+1}$ in the 300-500-s period range that are close in frequency (26,27), at frequencies below 1 mHz the spectral separation between modes is quite large and the coupling effects are weaker and more difficult to observe. Furthermore, the instrumental self-noise of the broad-band seismometers used in global seismic networks increases at low frequencies. Earths gravest free oscillations have therefore been studied primarily with gravimeter records, not seismometer records, after correction for fluctuations in atmospheric pressure (42-45). The signal-to-noise ratio for seismometer records of the 23 June 2001 Peru event (until Sumatra-Andaman the largest digitally recorded earthquake) was not high enough to allow the observation of hybridized toroidal modes on the vertical components. Such vertical motion has been reported previously from a gravimeter record. Vertical components of the toroidal modes ${}_0T_3$ and ${}_0T_4$ were observed after the strike-slip $M_w = 8.2$ 1998 Balleny earthquake (27). This was only possible after correction for atmospheric pressure effects. The mode ${}_0T_2$ was not observed.

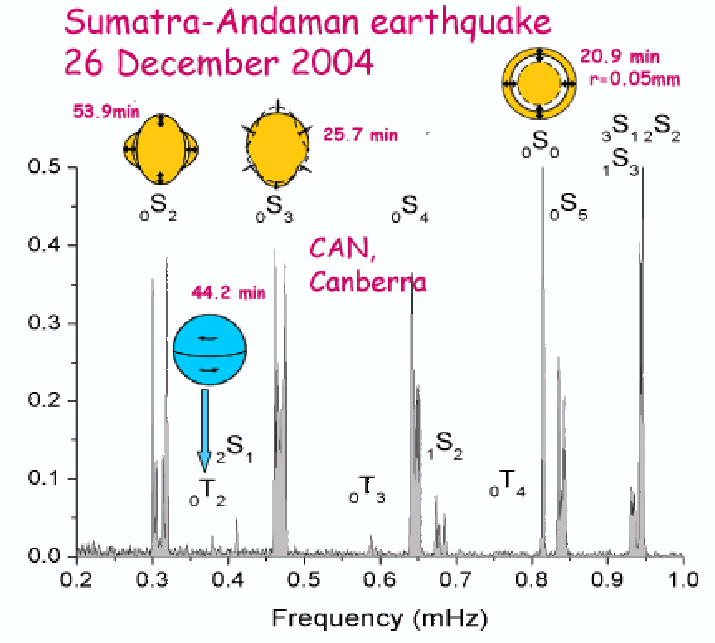

Figure 2.9: Sc[illegible] superimposed on a spectrum co[illegible]ed in Canberra, Australia, nea[illegible]cord of vertical acceleration is

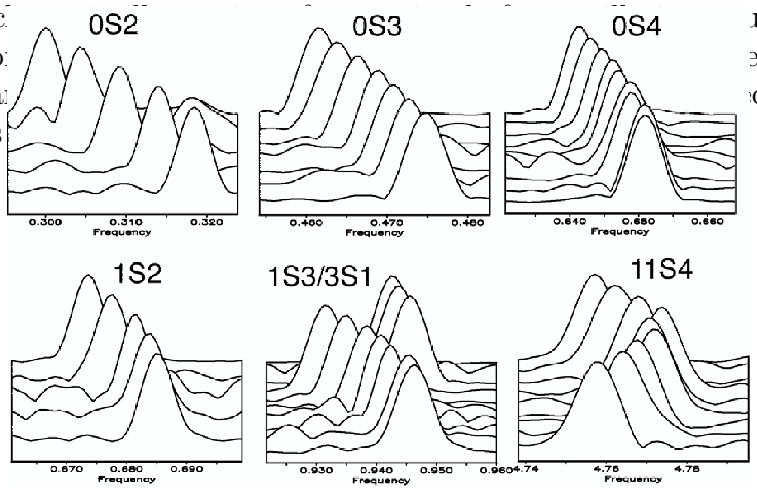

Figure 2.10: Gilbert and Dziewonski (5) showed that spectrum estimates from a global network could be summed with spherical-harmonic weights to enhance signal-to-noise ratios for specific Earth free oscillations. A further processing step, called "stripping", isolates modal spectral peaks associated with a single spherical harmonic. For the 2004 Sumatra-Andaman earthquake, the modes ${}_0S_2$, ${}_0S_3$, ${}_0S_4$ and ${}_1S_2$ were observed with an unprecedented signal-to-noise ratio. The mode pair ${}_1S_3/{}_3S_1$ has been observed with similar quality most recently during the 4 October 1994 Kuril Island earthquake which, until the great 21 June 2001 Peru earthquake, was the largest earthquake since the 19 August 1977 Sumbawa earthquake. Though its source was shallow, the 2004 Sumatra-Andaman earthquake also excited inner core sensitive modes such as ${}_11S_4$.

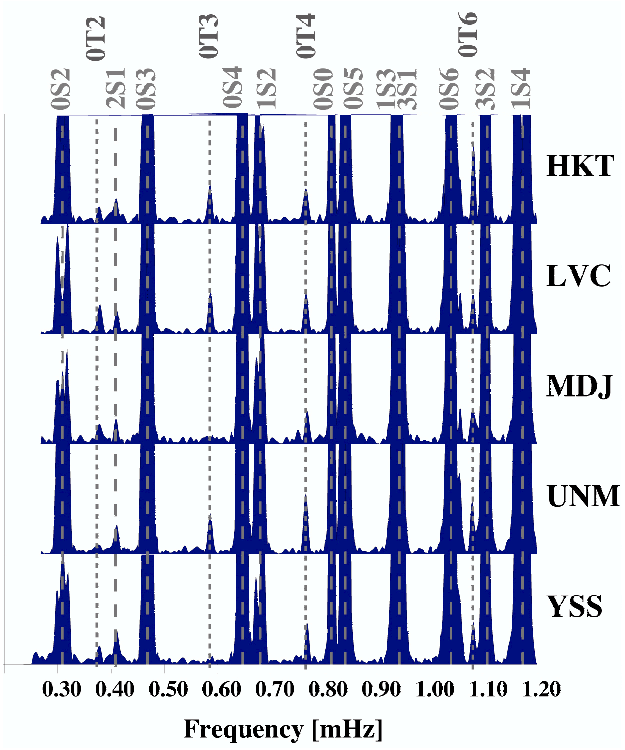

Figure 2.11: Vertical seismometer amplitude spectra of 58-hour time series from five stations of global seismic networks (HKT.IU: Hockley, Texas; LVC.GE: Limon Verde, Chile; MDJ.IC: Mudanjiang, China; UNM.G: Unam, Mexico; YSS.IU: Yuzhno Sakhalinsk, Russia). The spectral peaks at the frequencies of spheroidal modes are about ten times larger than peaks at the frequencies of toroidal modes, and have been clipped for better display. Earths Coriolis force induces the toroidal and spheroidal modes to hybridize, leading to vertical motion at the frequencies of toroidal modes, obeerved well above the noise floor.

Mode Type	CMT	Model II	Model III
${}_0S_2[0.295-0.325mHz]$	0.655 ± 0.025	0.005 ± 0.062	0.094 ± 0.057
${}_0S_3[0.455-0.480mHz]$	0.603 ± 0.032	-0.054 ± 0.067	0.056 ± 0.057
${}_0S_4[0.635-0.660mHz]$	0.534 ± 0.069	-0.158 ± 0.117	-0.030 ± 0.100
${}_1S_2[0.665-0.660mHz]$	0.483 ± 0.073	-0.358 ± 0.195	-0.180 ± 0.168
${}_0S_0[0.665-0.695mHz]$	0.517 ± 0.036	-0.138 ± 0.084	-0.005 ± 0.074
${}_0S_5[0.830-0.850mHz]$	0.505 ± 0.107	-0.169 ± 0.191	-0.042 ± 0.162
${}_2S_{2,1}\, S_{3,3}\, S_1[0.925-0.955mHz]$	0.450 ± 0.066	-0.234 ± 0.107	-0.078 ± 0.095

Table 2.1: Normalized spectral misfits for predicted seismic motion from the CMT solution and finite-rupture models II and III (3) for selected long-period spheroidal free oscillations. The misfit is defined as the normalized difference between absolute values of the Hann-tapered discrete Fourier transform. Although this misfit definition does not address phase errors in predicted seismic motion, it allows one to assess whether a mode spectral peak amplitude has been over- or underpredicted.

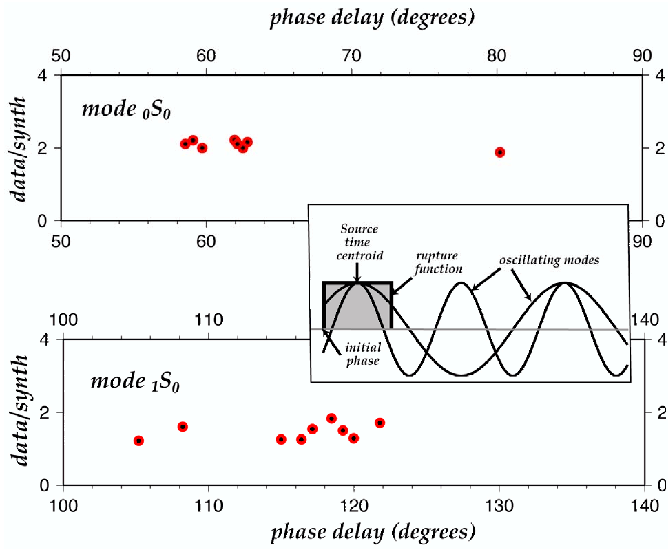

Figure 2.12: Ecitation parameters for the radial modes ${}_0S_0$ and ${}_1S_0$. For 9 Geoscope stations, we plot the amplitude magnification relative to the Harvard CMT solution, against the initial phase of the oscillation at rupture onset. The cartoon panel illustrates how the shifted phase of a free oscillation estimates the time centroid of a simple rupture model.

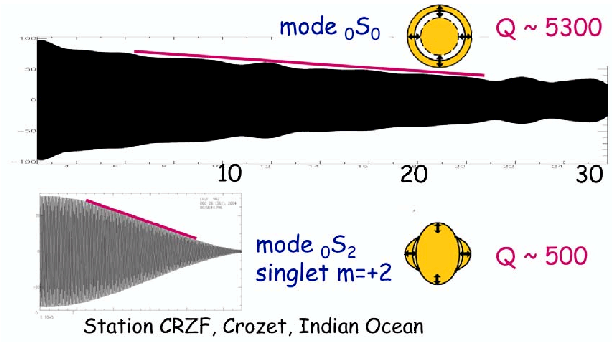

Figure 2.13: The unprecedented signal-to-noise ratios observed globally for high-Q free oscillations allows seismologists to follow their frictional decay over days, weeks and months. Shown here are narrow-band filtered modal oscillations for data from Geoscope station CRZF (Crozet, Indian Ocean). The decaying envelope of the modes ${}_0S_0$ and ${}_0S_2$ are clearly evident, extending for weeks. The horizontal axis is time, measured in days. The attenuation rates of these modes are quite similar previously estimated values.

2.6 References

1. G. Ekström, A. M. Dziewonski, N. N. Maternovskaya, M. Nettles, Phys. Earth Planet.Inter. 148, 327 (2005). Harvard CMT solutions can be accessed at http://www.seismology.harvard.edu/CMTsearch.html.

2. S. Stein, E. Okal, Nature, 434, 581-582 (2005).

3. C. J. Ammon et al., Science, 308, 1133-1139 (2005).

4. T. Lay et al., Science, 308, 1127-1133 (2005).

5. F. Gilbert, A. M. Dziewonski, Phil. Trans. Roy. Soc. London, A278, 187-269 (1975).

6. R. Buland, J. Berger, F. Gilbert, Nature, 277, 358-362 (1979).

7. R. J. Geller, S. Stein, Bull. Seism. Soc. Am., 69, 1671-1691 (1979);

8. J. P. Davis, Geophys. Res. Letts., 12, 141-144 (1985).

9. D. Giardini, X. Li, J. H. Woodhouse, Nature, 325, 405-411 (1987).

10. M. Ritzwoller , G. Masters, F. Gilbert, J. Geophys. Res., 93, 6369-6396 (1988).

11. R. Widmer, G. Masters, F. Gilbert, Geophys. J. Int., 104, 541-553 (1991).

12. G. Laske, G. Masters, Nature, 402, 66-69 (1999).

13. M. Ishii, J. Tromp, Science, 285, 1231-1236 (1999).

14. G. Roult, E. Clavede, Phys. Earth Planet. Int., 121, 1-37, 2000.

15. F. A. Dahlen, J.Tromp, Theoretical Global Seismology, Princeton (1998). A spherical reference model describes a non-rotating planet whose stress-strain relation is elastic and either isotropic or else exhibits anisotropy with a radial axis of symmetry.

16. J. H. Woodhouse, Geophys. J. Roy Astron. Soc., 61, 261-283 (1980).

17. F. A. Dahlen, Geophys. J. Roy Astron. Soc., 66, 1-22 (1981).

18. J. Park, F. Gilbert, J. Geophys. Res., 91, 7241-7260 (1986).

19. P. Lognonne, B. Romanowicz, Geophys. J. Int., 102, 365-395 (1990).

20. G. Backus, F. Gilbert, Proc. Nat. Acad. Sci. USA, 47, 362-371 (1961).

21. F. A. Dahlen, R. V. Sailor, Geophys. J. Roy Astron. Soc, 58, 609-623 (1979).

22. H. V. Benioff, F. Press, S. W. Smith, J. Geophys. Res., 66, 605-619 (1961).

23. N. F. Ness, J. C. Harrison, L. B. Slichter, J. Geophys. Res., 66, 621-629 (1961).

24. L. E. Alsop, G. H. Sutton, M. Ewing, J. Geophys. Res., 66, 631-641 (1961).

25. S. W. Smith, J. Geophys. Res., 71, 1183-1193 (1966).

26. G. Masters, J. Park, F. Gilbert, J. Geophys. Res., 88, 10285-10298 (1983).

27. W. Zürn, G. Laske, R. Widmer, F. Gilbert, Geophys. J. Int., 143, 113-118 (2000).

28. B. A. Romanowicz, D. Giardini, Science, 295, 2000-2001 (2001).

29. J. Park et al., EOS, Trans. Amer. Geophys. Un., 86, 57 (2005).

30. R. Butler et al., EOS, Trans. Amer. Geophys. Un. 85, 225 (2004).

31. J. Park et al., Seism. Res. Lett., 76, 329-340, (2005) All broadband seismic data is available via the Internet at http://www.iris.edu.

32. G. Roult et al., Phys. Earth Planet. Int., 113, 25-43 (1999); http://www.iris.edu, http://www.fdsn.org, http://geoscope.ipgp.jussieu.fr.

33. N. R. Goulty, G. C. P. King, A. J. Wallard, Nature, 246, 470 (1973).

34. B. A. Bolt, R. G. Currie, Geophys. J. Roy. Astron. Soc., 40, 107-114 (1975).

35. M. Zadro, C. Braitenberg, Earth Science Reviews, 47, 151-187 (1999). The Grotta Gigante pendulum tiltmeter recorded both the 1960 Chile and 2004 Sumatra-Andaman earthquakes.

36. M. Van Camp, Phys. Earth Planet. Int., 116, 81-92 (1999).

37. K. Nawa et al., Phys. Earth Planet. Int., 120, 289-297 (2000).

38. X. Lei, H. Xu, H. Sun, Kexue Tongbao, 47, 1573-1578 (2002).

39. K. M. Larson, P. Bodin, J. Gomberg, Science, 300, 1421-1424 (2003).

40. Free oscillations may be resolvable if GPS data from a global network are stacked and corrections for second-order ionospheric effects remove biases that are spatially broad, see S. Kedar, G. A. Hajj, B. D. Wilson, M. B. Heflin, Geophys. Res. Letts., 30, 1829, doi:10.1029/2003GL017639 (2003).

41. To calibrate gravimeter and seismometer spectra the free-oscillation spectral peaks must be corrected for the motion-induced gravitational forces on the seismic sensor (15). The breathing mode ${}_0S_0$ involves only motion parallel to Earths radius, and the free-air correction to local gravity magnifies its apparent motion by 12%. For data from the Sumatra-Andaman earthquake an apparent initial amplitude of 55

microns for 0S0 shrinks to 49 microns after this correction. Similar corrections must be made for all modal amplitudes at frequencies f < 1.0 mHz (T > 1000 s), including corrections for motion-induced accelerations associated with tilt and redistribution of Earths mass. For instance, the true vertical motion of the football mode ${}_0S_2$ is 81.2% that computed from the seismometer response alone.

42. The instrumental self-noise of the broadband seismometers used in global seismic networks increases at low frequencies. Earth's gravest free oscillations have therefore been studied primarily with superconducting gravimeter data, not seismometer records, after correction for fluctuations in atmospheric pressure (27, 43-45). The signal-to-noise ratio for seismometer records of the 23 June 2001 Peru event (M_w 8.4) was not high enough to allow the observation of hybridized toroidal modes on the vertical seismic components, but they are clearly evident for the 2004 Sumatra-Andaman earthquake.

43. W. Zürn, R. Widmer, Geophys. Res. Let., 22, 3537-3540 (1995).

44. M. Van Camp, Phys. Earth Planet. Int., 116, 81-90 (2000).

45. S. Rosat, J. Hinderer, L. Rivera, Geophys. Res. Let., 30, 2111, doi:10.1029/2003GL018304 (2003).

46. Such vertical motion has been reported previously from a gravimeter record. The toroidal modes ${}_0T_3$ and ${}_0T_4$ were observed after the strike-slip $M_w = 8.2$ 1998 Balleny earthquake, see W. Zrn et al., reference (27). This was only possible after correction for atmospheric pressure effects. The mode ${}_0T_2$ was not observed.

47. T. C. Hanks, H. Kanamori, J. Geophys. Res., 84, 2348-2350 (1979).

48. S. Stein, M. Wysession, An Introduction to Seismology, Earthquakes, and Earth Structure, Blackwell (2003).

49. M. Ishii, P. Shearer, H. Houston, J. Vidale, Nature, in press (2005).

50. R. Bilham, E. R. Engdahl, N. Feldl, S. P. Satyabala, Seism. Res. Letts., in press (2005).

51. R. Pillet, N. Florsch, J. Hinderer, D. Rouland, Phys. Earth Planet. Int., 84, 161-178 (1994).

52. Synthetics are computed according to normal-mode perturbation theory (15).

Perturbations from a spherical non-rotating Earth model, such as rotation, ellipticity and lateral heterogeneity are included. We adopt mantle model S20RTS (52) and crustal model crust2.0 (53) to account for lateral heterogeneity. The latest estimates of spheroidal and toroidal eigenfrequencies and quality factors are used in the calculation (54). Modal splitting and coupling due to rotation, ellipticity, and lateral heterogeneity are accounted for based upon a group coupling scheme using 36 subgroups of 117 modes below 3 mHz (55).

53. J. Ritsema, H. J. van Heijst, Science Progress, 83, 243-259 (2000).

54. C. Bassin, G. Laske, G. Masters, EOS Trans AGU, 81, F897 (2000).

55. Reference Earth Model: http://mahi.ucsd.edu/Gabi/rem.html.

56. A. Düess, J. Woodhouse, Geophys. J. Int. 146, 833-842 (2001).

Chapter 3

Low Velocity Zone atop the 410 km Seismic Discontinuity in the Northwestern US

Abstract

The 410 km seismic discontinuity (the 410) in the mantle is generally attributed to a phase transition from olivine to wadsleyite structure of $(Mg, Fe)_2SiO_4$ while the 660 seismic discontinuity (the 660) is presumably due to a phase transition from $(Mg, Fe)_2SiO_4$ ringwoodite to perovskite and magnesiowustite[1,2]. Their depths are often taken as proxies for variations in mantle temperature due to their opposite responses to a thermal anomaly. A cold anomaly will elevate the 410 because of its positive Clapeyron slope and depress the 660 because of its negative Clapeyron slope, while a hot anomaly will do the reverse. But tradeoffs between velocity heterogeneity and discontinuity topography often prevents high resolution of fine structure near these discontinuities and their dynamic implications. Particularly, the structure near the 410 appears to be very complicated. We simultaneously model seismic refracted waves and scattered waves from the 410 to constrain fine structures near the 410. We find a low velocity zone (LVZ, shear wave velocity drop of 5 %) atop the 410 beneath the northwestern United States, extending from southwestern Oregon to the northern Basin and Range. The LVZ has thickness varying from 20 up to 90 km with rapid lateral variations. The spatial extent of the LVZ coincides with anomalous receiver function determinations and the region with distinct high-alumina-olivine-tholeiite (HAOT) volcanism. We interpret the LVZ as a compositional anomaly, possibly due to a dense partial-melt layer, which may be linked to prior Farallon plate subduction and back-arc extension. The existence of such a layer could be indicative of high water content in the Earth's transition zone. *(Originally published as Song, Helmberger and Grand, Nature, 427, 530-533, 2004)*

3.1 Introduction

Spatial variations in topography of the 410 and the 660 are often inferred from SS precursors (lengthscale of about 1500-2000 km[3,4]), near subduction zone depth phase precursors[5], and receiver function analyses (lengthscale of about 100-300 km[6–8]). The latest efforts consider simultaneously inverting for both mantle velocity and discontinuity topography[3]. In general, the 660 is depressed under cold regions (slabs) as expected, but the 410 appears far more complicated[3–5]. The stacked converted P-to-S phase (Ps) (receiver function) from the 410 is rather weak, complicated, and sometimes shows negative pulses above the 410[7].

3.2 Data and Modeling

We first compute 1-D full waveform synthetics[9] and model the direct S wave triplications at epicentral distances of 14-17 degrees and explain the timing and amplitude of multiple arrivals coming from fine structures near the 410[10]. To resolve the trade-offs between discontinuity topography and mantle velocity directly above or below the discontinuity, we model S wave triplications at epicentral distances of 21-24 degrees. A LVZ atop the 410 produces a secondary pulse not normally seen at these distances. Using this secondary pulse as a proxy for the existence of a LVZ atop the 410, we examine events located offshore of Washington-Oregon, USA, and recorded by the TriNet broadband network and several temporary PASSCAL broadband arrays (Fig. 3.1).

Perturbed velocity structures are shown at the turning point for a given great circle path because the sensitivity to 410 structure is greatest there[11]. The size of the perturbed structure is estimated as the size of the Fresnel zone in both along-path and cross-path direction. We determine a LVZ directly above the 410 in the northwestern US and cross-validate our finding with receiver function profiles[7].

Record section A shows typical waveform characteristics sampling this area at epicentral distances of 14-17 degrees (Fig. 3.2). It samples the region beneath the

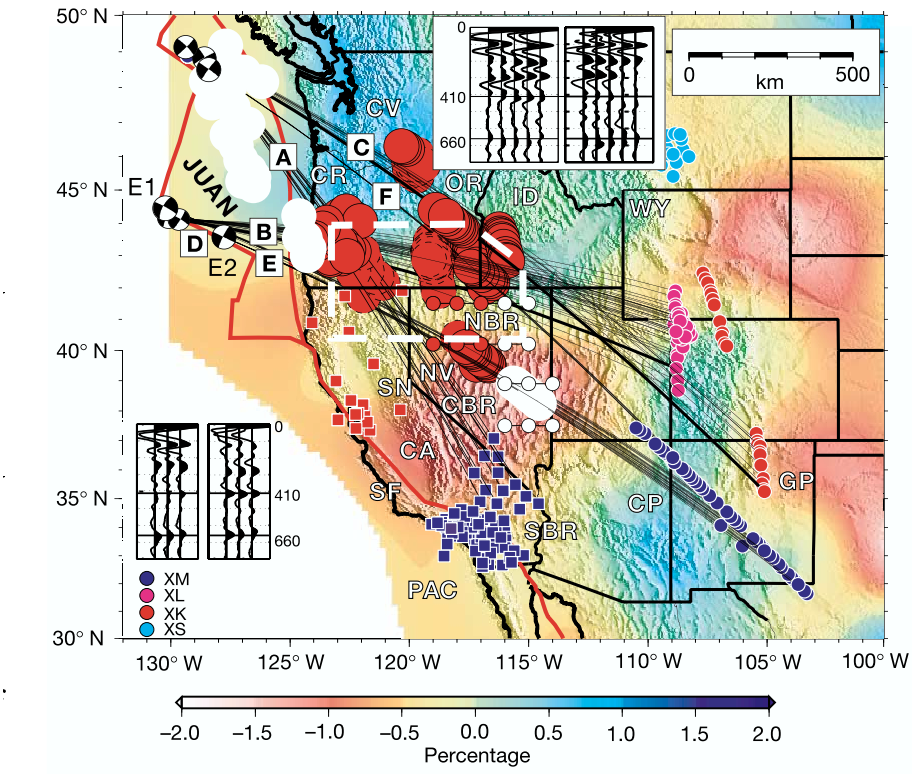

Figure 3.1: Map of western US displaying samples of fine structure near the 410 km seismic discontinuity. Events off the coast of Oregon and Washington are recorded by several PASSCAL arrays (small circles), TriNet (blue squares), and Berkeley network (red squares). Ray-paths of record sections A−F are shown in black lines. Color patches display areas sampled by the triplication data; white (normal, no detectable LVZ), red patches outlined with dashed line (anomalous 410 with a possible LVZ), red patches outlined with solid line (clear LVZ). The areal extent of HAOT[13] is indicated by a heavy white dashed line. The base-color map shows the variation in SV-shear velocity (relative to the 1-D reference model) at a depth of 370 km[12]. Thick red lines show the plate boundary. An inset at the top shows receiver function determination at 41.5°N, 119° − 115°W (left column) and 40.2°N, 115° − 119°W (right column). An inset in the lower left shows receiver function determination at 38.9°N, 116° − 114°W (left column) and 37.5°N, 114-116°W (right column). Red dots shown in the map (within Nevada) indicate the location where receiver functions show strong negative pulse above the 410, while white dots represent the location where receiver functions show no negative pulse above the 410 and relatively strong simple 410 peaks. Abbreviations are: GP, Great Plain; YW, Yellow Stone; NBR, northern Basin and Range; CBR, central Basin and Range; SBR, south Basin and Range; SN, Sierra Nevada; CV, Cascadia Volcanic Arc; CR, Coast Ranges; JUAN, Juan de Fuca plate; PAC, Pacific plate; SF, San Andreas Fault; CA, California; NV, Nevada; OR, Oregon; ID, Idaho; XM, Rio Grande Rift Seismic Transect array (99/07-01/05); XL, Deep Probe array (97/05-97/11); XK, CDROM (Colorado) array (99/04-00/09); XS, Montana Broadband array (99/11-00/09).

California-Oregon border (Fig. 3.1).

Relative to the 1-D reference model (section 3.4), we observe a considerable increase of separation in timing between the branch AB and the branch CD of about 4-6 seconds (Fig. 3.3, Fig. 3.4). At these ranges, the branch AB represents the S wave propagating through the upper mantle and turning at about 200-300 km and the branch CD represents the S wave bottoming near the 410 (Fig. 3.3).

Synthetics calculated from a perturbed 1-D model with the 410 depressed by 60 km improve the differential time between the AB and CD branches considerably (model Topo in Fig. 3.2). However, other models can also fit the data equally well (Fig. 3.2, Fig. 3.8).

Record section B (Fig. 3.9) trends more east-west and samples the region beneath the northern Basin and Range including eastern Oregon, northern Nevada, and western Idaho (Fig. 3.1). This record section shows similar waveforms to those in record section A and previously introduced models can be used to fit the data (Fig. 3.4, Fig. 3.9). These record sections indicate that the mantle structure near the 410 is relatively slow beneath the northern Basin and Range. The anomalous structure is probably distributed over areas from the California/Oregon border to the northwestern Basin and Range.

Although it is clear that seismic velocity is slow near 410 km depth, we can not distinguish between these models including a topographic depression of the 410, a modest decrease in velocity gradient above the 410, a LVZ above the 410, or a hybrid model (LVZA) with the 410 depressed and a LVZ atop the 410 (Fig. 3.2, Fig. 3.8). It is difficult to explain this anomaly with current 3-D velocity models[12] because variations in shear wave velocity at these depths are generally small (Fig. 3.1).

At the longer epicentral distances of 21-24 degrees, however, it is the branch AB that is bottoming near the 410 (Fig. 3.3). In combination with ray paths at the shorter distances, they provide strong constraints on the structure near the 410. Travel time curves from model LVZA atop the 410 not only explain the differential time of branch AB and branch CD at epicentral distance of 14-17 degrees, but also extend the branch AB from a maximum epicentral distance of 21 degrees to 23 degrees (Fig.3.4).

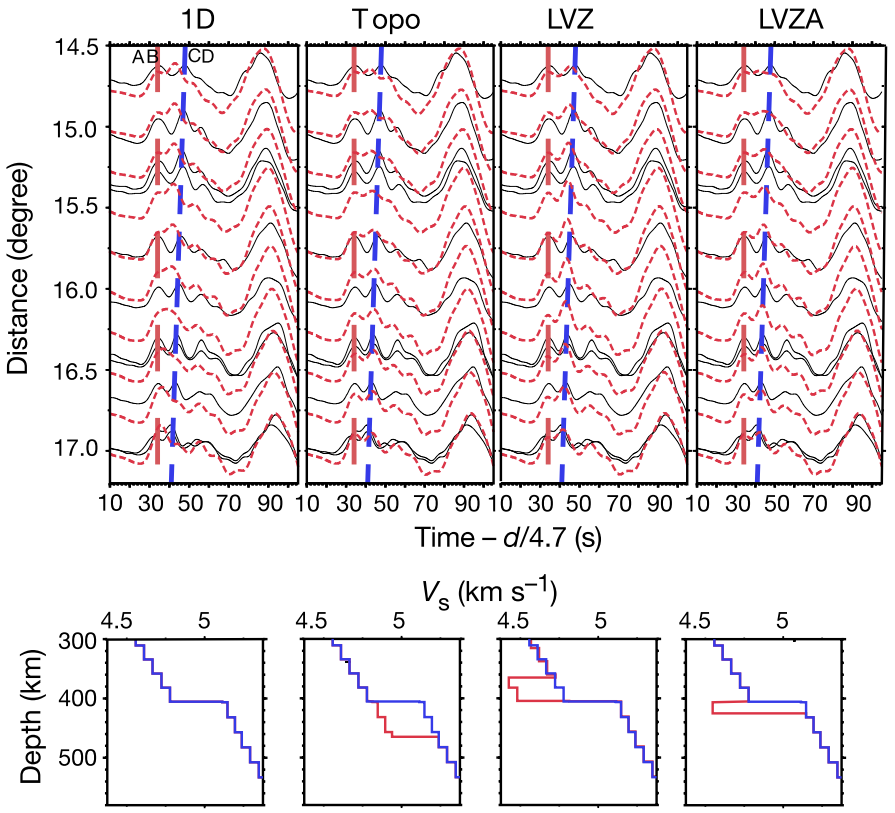

Figure 3.2: record section A (recorded by TriNet, see Fig. 3.1). Data (black traces) are compared with synthetics (red traces) generated from various models, starting from the left: 1-D model, model Topo (60 km topography depression), model LVZ (40 km LVZ) and model LVZA (20 km LVZ + 20 km topography depression). Dashed and dash-dotted lines indicate observed triplication branches AB (red) and CD (blue), respectively. Large amplitude and long period waves at the end of these traces are Love waves, which is sensitive to the shallow structure. Velocity models used to compute the synthetics are directly shown below these waveforms. The perturbed model is shown in red line and the reference model is shown in blue line. The time scale is shown with reduced velocity of 4.7 km/sec.

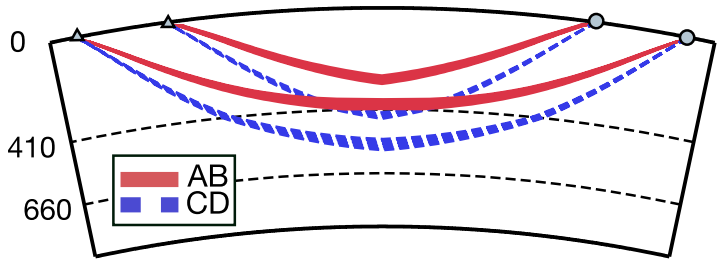

Figure 3.3: Ray paths of triplication branches AB (red line) and CD (blue dashed line). The 410 and 660 seismic discontinuities are given in dashed lines. Note that, at the shorter distance (ex. 16 degrees), the branch CD is primarily sensitive to the structure at the turning point near the depth of 400 km. However, at the longer distance (ex. 22 degrees), the branch AB is primarily sensitive to the same structure.

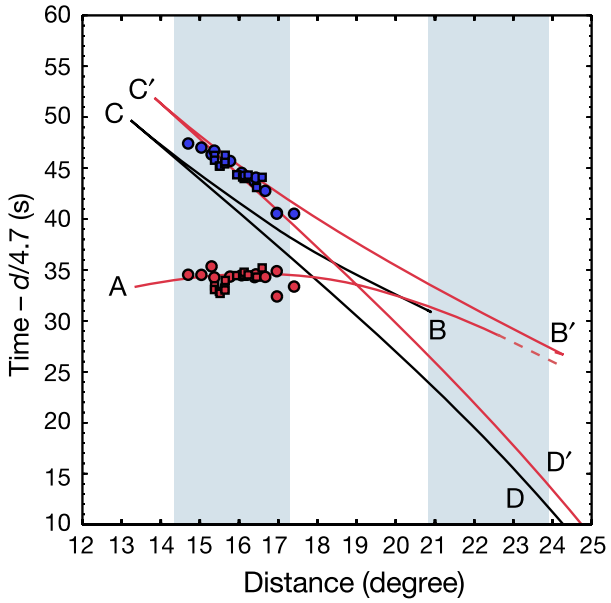

Figure 3.4: Triplication curves computed from 1-D model (black line) and model LVZA (thick red line). Observed branches AB and CD of record section A (circle) and record section B (square) are projected with red symbols and blue symbols, respectively (see also Fig. 1 for ray paths). Note that model LVZA delays the branch CD to fit the above observations but also extends the appearance of the branch AB to epicentral distance of 21-23 degrees.

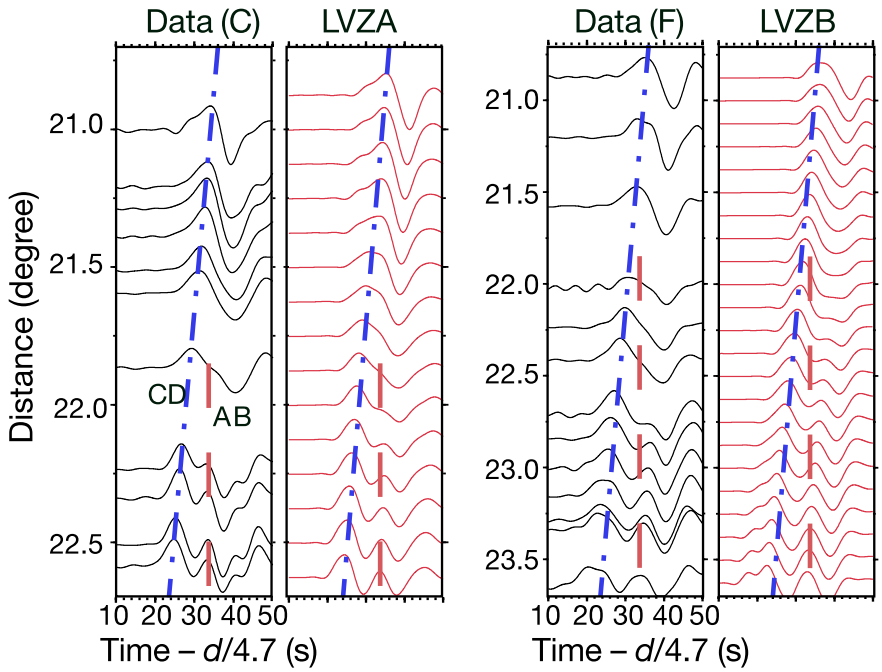

Figure 3.5: Record section C (recorded by XK PASSCAL stations, see Fig. 3.1) and synthetics from a hybrid model LVZA (20 km LVZ + 20 km topography depression) are shown on the left two columns. Record section F (recorded by XM PASSCAL stations, see Fig. 3.1) and synthetics from a hybrid model LVZB (70 km LVZ + 60 km topography depression) are shown on the right two columns. Note that the separation between branches AB and CD is larger in record section F than that in record sections C, indicating a thicker LVZ. Dashed and dash-dotted lines indicate observed triplication branches AB (red) and CD (blue), respectively (see also Fig. 3.3). The time scale is shown with reduced velocity of 4.7 km/sec.

Record section C (Fig. 3.5) samples the northern Basin and Range province and shows an anomalous secondary pulse emerging at epicentral distances of 22-23 degrees, which is also seen in record sections D and F (Fig. 3.5, Fig. 3.6).

The model with a large topographic depression (60 km) of the 410 does not reproduce this feature. The model with a 40 km thick LVZ containing a 5% reduction in shear velocity produces the observed secondary pulse, but the separation between the first and secondary pulse appears too large (Fig. 3.10). We prefer a hybrid model (LVZA) which explains these record sections in both amplitude and timing. This model has the 410 depressed by 20 km and a 20 km thick LVZ atop the 410 with a

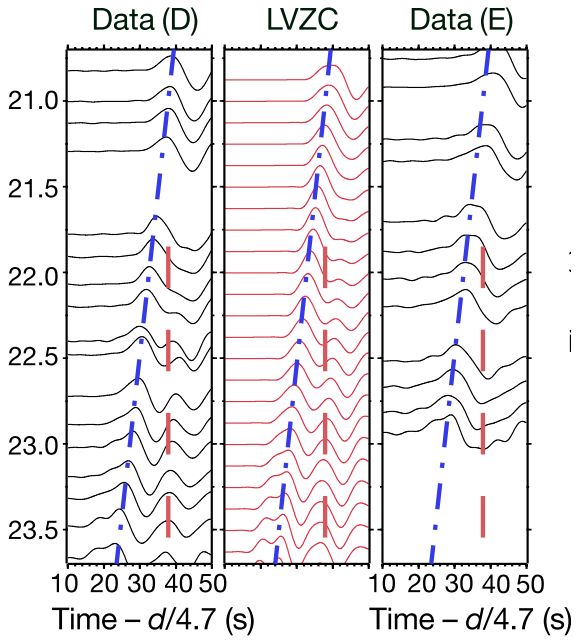

Figure 3.6: Record section D (recorded by XM PASSCAL stations, see Fig. 3.1) and synthetics from a hybrid model LVZC (90 km LVZ + 60 km topography depression) are shown on the left two columns. Record section E (recorded by XM PASSCAL stations) is shown on the right column. Dashed and dash-dotted lines indicate observed triplication branches AB (red) and CD (blue), respectively (see also Fig. 3.3). The time scale is shown with reduced velocity of 4.7 km/sec. Triplication branch bottoming beyond the 660 arrives at or even ahead of the CD branch at these ranges. Note record sections D and E sample regions only 100 km apart (see also Fig. 3.1). No secondary pulse branch AB is observed in record section E at these distances.

5% reduction in shear velocity.

Due to the relatively long period of the S waves (about 6-8 seconds), a tradeoff between the thickness and strength of the LVZ still exists. Therefore, we can not completely exclude a model having a LVZ of 10 km with 10% velocity drop, or a model having a LVZ of 40 km thick with a 2.5% velocity drop. However, record sections at epicentral distances of 14-17 degrees shows that the amplitude of the branch CD predicted by a model having a LVZ with a 10% velocity drop appears too large. Furthermore, receiver function synthesis discussed later indicates that the amplitude of a negative converted pulse due to the existence of a LVZ with only a

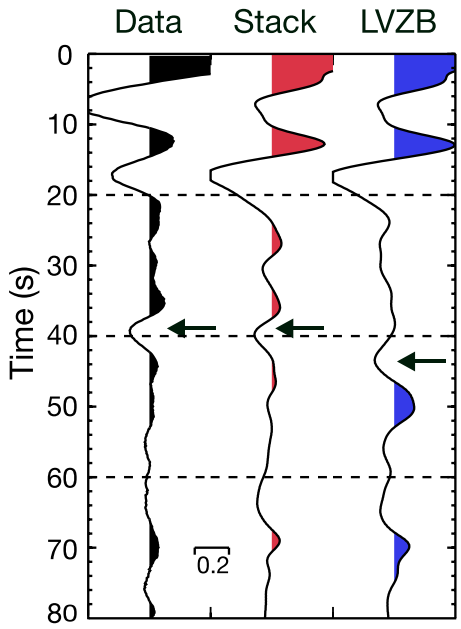

Figure 3.7: Comparison of stacking receiver function profile[7] and forward calculations. All traces are normalized by the amplitude of P wave and shown with a ray parameter of 0.06 sec/km. The left trace shows the receiver function profile, which samples similar regions as record section F (see also Fig. 3.1). The right trace shows the synthetic receiver function from model LVZB. The middle trace shows a synthetic receiver function by stacking receiver functions computed from multiple 1-D models, which have variations in the 410 and the thickness of LVZ. The arrow points out the negative converted pulse due to the existence of the LVZ atop the 410.

2.5% velocity drop can not explain observed receiver functions. Thus, our preferred model has a 20 km LVZ with a 5% reduction in velocity.

3.3 Discussion

The spatial extent of the LVZ includes regions beneath northern California, Oregon, northern Nevada, and southwestern Idaho, corresponding to an area of about 100,000 km^2 (Fig. 3.1). The thickness of the LVZ is about 20 km (Fig. 3.5, model LVZA) but appears thicker beneath the Oregon-Nevada-Idaho border up to 70 km (Fig. 3.1,

Fig. 3.5, model LVZB). In central Nevada, the thickness of the LVZ is up to 90 km (Fig. 3.1, Fig. 3.6, model LVZC). However, when examining record section E, we find no evidence for a LVZ atop the 410 beneath the central Basin and Range in eastern Nevada (Fig. 3.1, Fig. 3.6). These observations imply that the spatial variation of the LVZ in thickness is very rapid. This conclusion is supported by receiver function determination[7], where strongly negative pulses directly above the 410 converted pulses suddenly disappear in profiles east of 116° (Fig. 3.1). In addition, we note that record sections sampling regions beneath the Juan de Fuca plate show no signs of a LVZ atop the 410 (Fig. 3.1).

To validate our result, we produce a synthetic receiver function and compare to the published result[7] for areas closest to that sampled by record section F. The synthetic receiver function from the preferred model LVZB indeed produces a negative pulse associated with the LVZ atop the 410, but the predicted onset of the negative pulse is late and the converted pulse from the 410 is too strong (Fig. 3.7). The observed receiver function determination is constructed through stacking multiple receiver function profiles from various azimuths where both the thickness of the LVZ and the depth of the 410 are probably changing. Under such circumstances, we can produce the complicated converted pulse from the 410 and the negative pulse from the LVZ atop the 410 (Fig. 3.7, see section 3.4). We could not reproduce receiver functions with a strong negative pulse without inserting a LVZ atop the 410.

We note that strongly negative pulses are absent in areas where we detect no LVZ (Fig. 3.1, white patches), while converted pulses from the 410 are rather strong and simple (Fig. 3.1). In general, we expect the amplitude of the converted phase from the 410 to be smaller than that from the 660 because of its smaller velocity contrast. One possible explanation is that these relatively strong converted pulses from the 410 could be related to the existence of a very thin LVZ atop the 410, which increases the velocity contrast but is too thin to be detected.

Geographically, the anomalous region discussed above coincides with a unique type of mantle-derived basalt exposed in the northwestern United States: low-potassium, high-alumina olivine theoleiites (HAOT)[13,14]. Noticeably, HAOT is on average 10

times more depleted in incompatible elements than any other type of basalt found in the rest of the Basin and Range and the western US[13–16]. It is generally believed that formation and eruption of HAOT are strongly linked to extensional tectonics in the back-arc regime. The geographical coincidence between the unique HAOT and the LVZ atop the 410 in the northwestern Basin and Range might suggest that they are probably linked to tectonic processes such as subduction of the Farallon plate and surface extension in the back-arc regime[17]. Other reports of such LVZs directly above the 410 are usually associated with back-arc regimes of ongoing subduction or ancient subduction[5,18–21].

If the LVZ is primarily due to variations in mantle temperature, the thickness of the LVZ is expected to vary gradually. However, the thickness of the LVZ varies rapidly over length scales of about 100-200 km. Therefore, we argue against a thermally dominant origin and prefer a compositional anomaly. The presence of partial melt could considerably lower the velocity[22] but this interpretation is directly linked to the water content actually brought into the deep upper mantle[23,24]. If the water content is sufficiently high in the transition zone, the LVZ may form directly above the 410 in upwelling material as a result of dehydration melting[25].

For an anhydrous silicate melt, the density of melt can be equal to or larger than that of ambient mantle at depths close to the 410[26–29]. For a hydrous silicate melt, however, not much information is currently available on its density. If the effect of water on the bulk modulus of solids is considered similar to that on the bulk modulus of melts while the linear relationship between bulk modulus and density holds[30], hydrous melts may be still denser than hydrous solids. Therefore, the LVZs would be relatively stable for long periods of time.

3.4 Supplementary information

The 1-D reference S model is modified from TNA model10. We adopt an average upper mantle velocity from 3-D mantle velocity model constructed for the western United States112. The reference depth of the 410 is at 405 km with 5% jump in

shear velocity. In addition, the thickness of the crust is fixed at 30 km while we vary the thickness of lithosphere (20-40 km) to match the entire waveforms from the AB branch to the Love wave. Synthetics are computed by the FK reflectivity method[9] with earthquake parameters from Harvard Centroid Moment Tensor solutions.

The synthetic receiver function is computed with reflectivity method via a given 1-D velocity model. We simulate stacked receiver function by randomly stacking synthetic receiver functions. Those synthetic receiver functions are computed from velocity models with variations in the thickness (20-90 km) of a LVZ atop the 410 and discontinuity topography (20-60 km). A Gaussian filter of 0.5 Hz is applied to each synthetic receiver function.

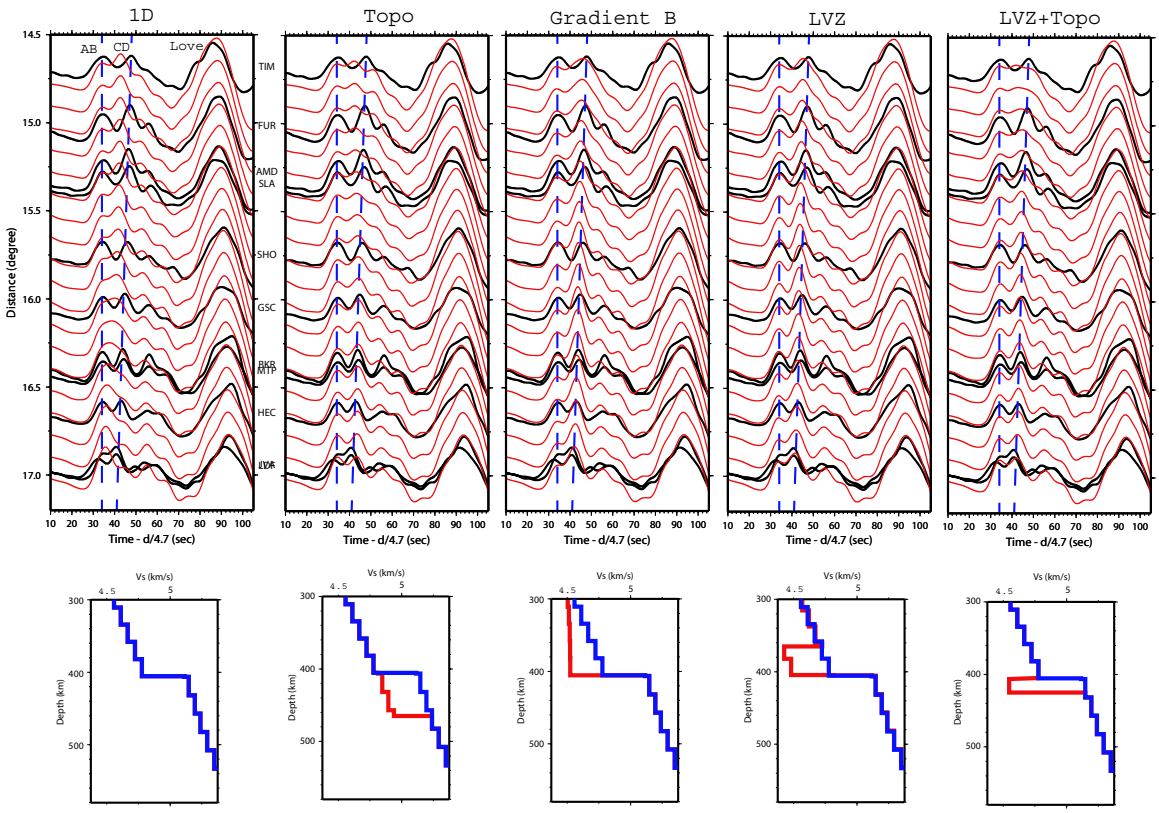

Figure 3.8: Sensitivity test at 14°-17° along path A. The top panels show the comparison of observed tangential displacement records (in black) and synthetics (in red). The lower panels show the corresponding velocity models. From left to right: 1D (dep_{410} = 405 km), Topo (dep_{410} = 465 km), Gradient B, LVZ ($dV_S = -5\%$, H_{LVZ} = 40 km) and LVZ+Topo ($dV_S = -5\%$, H_{LVZ} = 20 km, dep_{410} = 425 km).

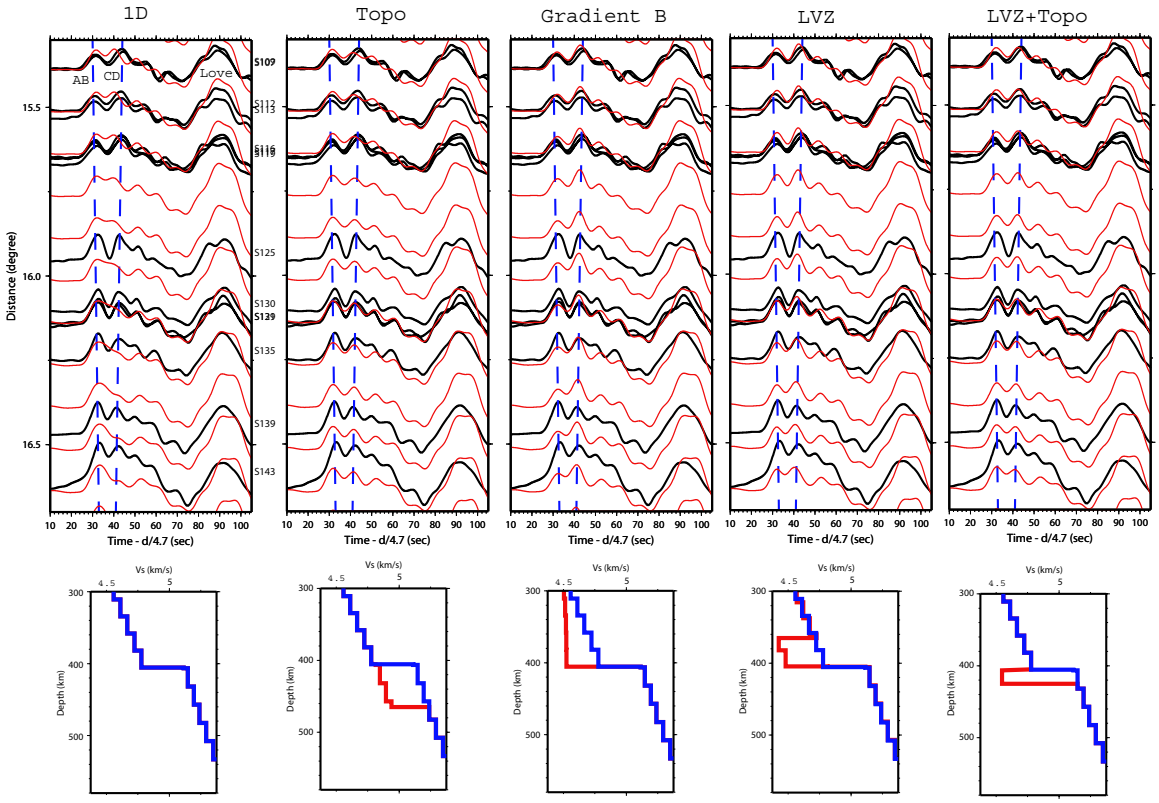

Figure 3.9: Sensitivity test at 14°-17° along path B. The top panels show the comparison of observed tangential displacement records (in black) and synthetics (in red). The lower panels show the corresponding velocity models. From left to right: 1D (dep_{410} = 405 km), Topo (dep_{410} = 465 km), Gradient B, LVZ ($dV_S = -5\%$, H_{LVZ} = 40 km) and LVZ+Topo ($dV_S = -5\%$, H_{LVZ} = 20 km, dep_{410} = 425 km).

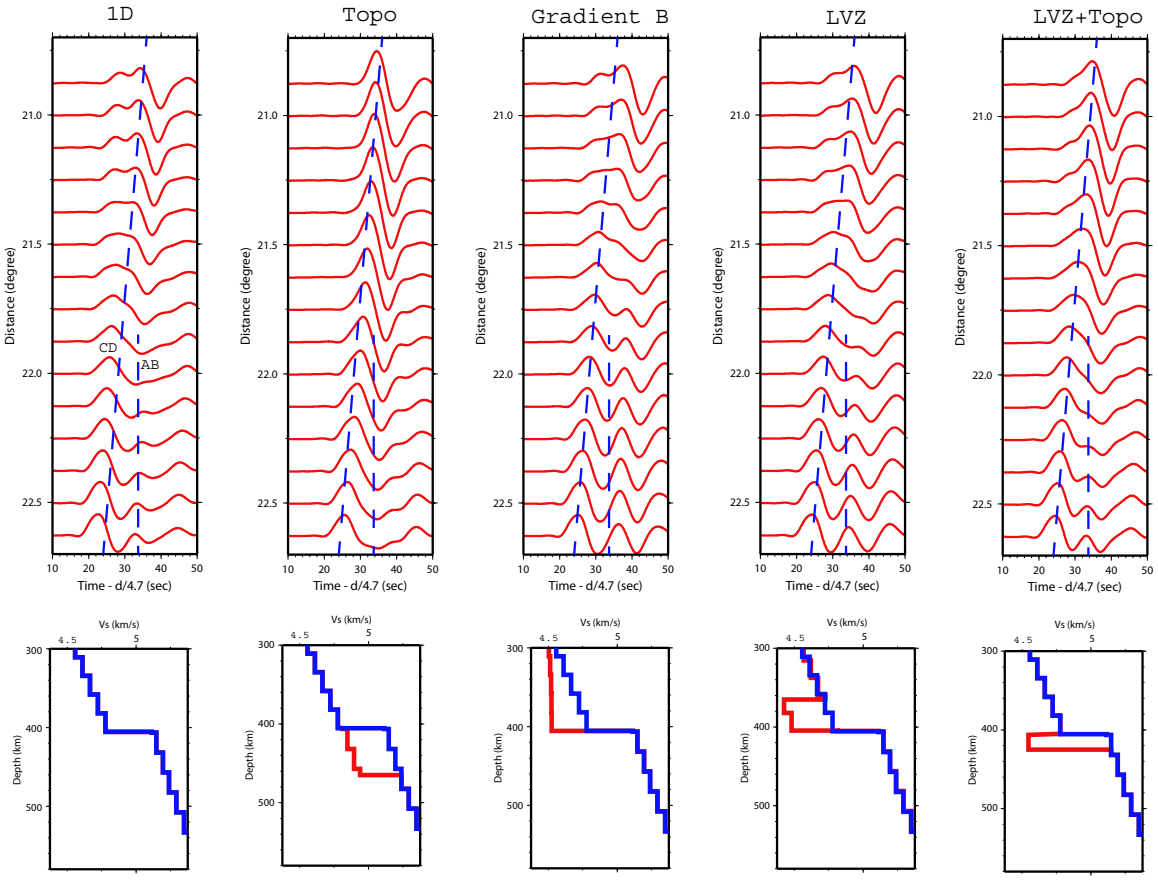

Figure 3.10: Sensitivity test at 20.7°-22.7° along path C. The top panels show the comparison of observed tangential displacement records (in black) and synthetics (in red). The lower panels show the corresponding velocity models. From left to right: 1D (dep_{410} = 405 km), Topo (dep_{410} = 465 km), Gradient B, LVZ ($dV_S = -5\%$, H_{LVZ} = 40 km) and LVZ+Topo ($dV_S = -5\%$, H_{LVZ} = 20 km, dep_{410} = 425 km).

3.5 References

1. Helffrich, G. Topography of the transition zone seismic discontinuity. Rev. Geophys. 38, 141-158 (2000).

2. Shearer, P. M. Upper mantle seismic discontinuities, Earth's Deep Interior: Mineral Physics and Tomography from the Atomic to the Global scale, AGU Geophysical Monograph Volume 117, edited by Shun-Ichiro Karato, A. M. Forte, R. C. Liebermann, G. Master, L. Stixrude, pp. 115 (2000).

3. Gu, Y., Dziwonski, A. M. & Ekstrom, G. Simultaneous inversion for mantle velocity and topography of transition zone discontinuities. Geophys. J. Int. 154, 559-583 (2003).

4. Flanagan, M. P. & Shearer, P. M. Global mapping of topography on transition zone velocity discontinuities by stacking SS precursors. J. Geophys. Res. 103, 2673-2692 (1998).

5. Flanagan, M. P. & Shearer, P. M. Topography on the 410 km seismic velocity discontinuity near subduction zones from stacking of sS, sP, and pP precursors. J. Geophys. Res. 103, 21165-21182 (1998).

6. Ramesh, D. S., Kind, R. & Yuan, X. Receiver function analysis of the North America crust and upper mantle. Geophys. J. Int. 150, 91-108 (2002).

7. Gilbert, H. J., Sheehan, A. F., Dueker, K. G. & Molnar, P. Receiver functions in the western United States, with implications for upper mantle structure and dynamics. J. Geophys. Res. 109, No. B5, 2229, doi:10.1029/2001JB001194 (2003).

8. Dueker, K. G. & Sheehan, A. F. Mantle discontinuity structure from midpoint stacks of converted P to S waves across the Yellowstone hotspot track. J. Geophys. Res. 102, 8313-8327 (1997).

9. Saikia, C. K. Modified frequency-wave-number algorithm for regional seismograms using Filons quadrature-Modeling of Lg waves in eastern North America. Geophys. J. Int. 118, 142-158 (1994).

10. Grand, S. P. & Helmberger, D. V. Upper mantle shear structure of North America. Geoophys. J. R. Astr. Soc. 76, 399-438 (1984).

11. Kennett, B. L. N. & Bowman, J. R. The velocity structure and heterogeneity of the upper mantle. Phys. Earth Planet. Inter. 59. 134-144 (1990).

12. Van der Lee, S. High-resolution estimates of lithospheric thickness from Missouri to Massachusetts, USA. Earth Planet. Sci. Lett. 203, 15-23 (2002).

13. Hart, W. K., Aronson, J. L. & Mertzman, S. A. Areal distribution and age of low-K, high-alumina olivine tholeiite magmatism in the northwestern Great Basin. Geol. Soc. Am. Bull. 95, 186-195 (1984).

14. Hart, W. K. Chemical and isotopic evidence for mixing between depleted and enriched mantle, northwestern U. S. A. Geochimica. et. Cosmochimica Acta, 49, 131-144 (1985).

15. Fitton, J. G., James, D. & Leeman, W. P. Basic magmatism associated with late Cenozoic extension in the western United States: Compositional variations in space and time. J. Geophys. Res. 96, 13693-13711 (1991).

16. Kempton, P. D., Fitton, J. G., Hawkesworth, C. J. & Ormerod, D. S. Isotopic and trace element constraints on the composition and evolution of the lithosphere beneath the southwestern United States. J. Geophys. Res. 96, 13713-13735 (1991).

17. Awater, T. & Stock, J. Pacific North America plate tectonics of the Neogene southwestern United States. Int. Geol. Rev. 40, 375-402 (1998).

18. Sacks, I. S. & Snoke, J. A. The use of converted phases to infer the depth of the lithosphere-asthenosphere boundary beneath South America, J. Geophys. Res. 82, 2011-2017 (1977).

19. Revenaugh, J. & Sipkin, S. A. Seismic evidence for silicate melt atop the 410-km mantle discontinuity. Nature, 369, 474-476 (1994).

20. Nolet, G. & Zielhuis, A. Low S velocities under the Tornquist-Teisseyre zone: evidence for water injection into the transition zone by subduction. J. Geophys. Res. 99, 15813-15820 (1994).

21. Vinnik, L., Kumar, M. R., Kind, R. & Farra, V. Super-deep low-velocity layer beneath the Arabian plate. Geophys. Res. Lett. 30, no. 7, 1415, doi:10.1029/2002GL016590 (2003).

22. Hammond, W. C. & Humphreys, E. D. Upper mantle seismic wave velocity: Ef-

fects of realistic partial melt geometries. J. Geophys. Res. 105, 10975-10986 (2000).

23. Williams, Q. & Hemley, R. J. Hydrogen in the deep Earth. Annu. Rev. Earth. Planet. Sci. 29, 365-418 (2001).

24. Dixon, J. E., Leist, L. Langmuir, J. & Schilling, J-G. Recycled dehydrated lithosphere observed in plume-influenced mid-ocean-ridge basalt. Nature, 420, 385-389 (2002).

25. Bercovici, D. & Karato, S. Whole-mantle convection and the transition-zone water-filter. Nature, 425, 39-44 (2003).

26. Stolper, E. M., Walker, D., Hager, B. H. & Hays, J. F. Melt segregation from partially molton source regions: the importance of melt density and source region size. J. Geophys. Res. 86, 6261-6271 (1981).

27. Rigden, S. M., Ahrens, T. J. & Stolper, E. M. Densities of liquid silicates at high pressure. Science, 226, 1071-1074 (1984).

28. Agee, C. B. Crystal-liquid density inversions in terrestrial and lunar magmas. Phys. Earth Planet. Inter. 107, 63-74 (1998).

29. Chen, G. Q., Ahrens, T. J. & Stolper, E. M. Shock-wave equation of state of molton and solid fayalite. Phys. Earth Planet. Inter. 134, 35-52 (2002).

30. Angel, R. J., Frost, D. J., Ross, N. L. & Hemley, R. Stabilities and equations of state of dense hydrous magnesium silicates. Phys. Earth Planet. Inter. 127, 181-196 (2001).

Chapter 4

Low Velocity Zone atop the Transition Zone in the Western US from S Waveform Triplication

Abstract

? modeled regional S wave triplications in the northwestern US and found a low velocity zone atop the 410 seismic discontinuity. Strong azimuthal variation in waveforms associated with paths sampling the western edge of this structure are observed on the TriNet array for several events. Here, We model this data with a new 3D simulation technique which combines 2D finite-difference with Kirchhoff diffraction operators to include responses off the great circle. To reconcile such sharp changes in waveforms require a sharp western edge less than 100 km across a boundary with a change of 3-5 % in velocity. Though the geometry of the LVZ is not unique due to limited data analyzed, the sharp edge of the LVZ is robustly constrained with available array data. Such a LVZ is consistent with the existence of water in Earth's transition zone, at least locally. *(Original published Song and Helmberger, 2006, Earth's Deep Water Cycle, Geophysical Monography Series 168, 195-213)*

4.1 Introduction

Melt segregation is one of the most important processes involved in understanding the chemical evolution of the Earth's mantle (**?**). High pressure experiments indicate that dry basaltic melt produced by partial melt of peridotite is neutrally buoyant at conditions of the 410-km discontinuity (**???**). However, it is not clear if hydrous silicate melt also behaves in the same manner. One of the most recent studies indicates that the effect of water on the density of silicate melt under high pressure is small enough that the melt can be trapped in the deep upper mantle (**?**), if the water content is less than 2%. To form such a molten layer near the 410, dehydration melting across the 410 can generate the melt due to the difference in solubility between the deep upper mantle (Olivine-rich) and the transition zone (Wadsleyite-rich) (**?**). Furthermore, **?** suggested that hydrous melting can continue to generate small amounts of melt as the material ascends through the upper mantle, while its depth extent would depend on the storage capacity profile of the upper mantle. In any case, the presence of such molten layers provide evidence for a dissolved water component in the transition zone (**??**), if not globally. Therefore, it is important to seismically constrain the geometry of such layers.

The structure near the 410 is known to be complicated beneath the western US from receiver function analysis (**?**). These receiver functions are constructed by stacking multiple profiles from various azimuths. Normally, a clear positive peak near 410 km and 670 km appears, indicating the expected polarity of a P to S conversion (fast to slow velocity jump). However, some abnormal results occur where a strong negative pulse appears suggesting a low velocity zone (**?**). These samples essentially establish locations of LVZs from vertically traveling paths. As demonstrated in **?**, the observed abnormal samples also occur where there are abnormal wide-angle reflections or triplication shifts. In order to sample the deep upper mantle with complementary horizontal paths, which forms the upper mantle triplications and have great sensitivity near the 410, we analyze body waves propagating at distances of 14°-24°. A more complete review of these types of data will be addressed here.

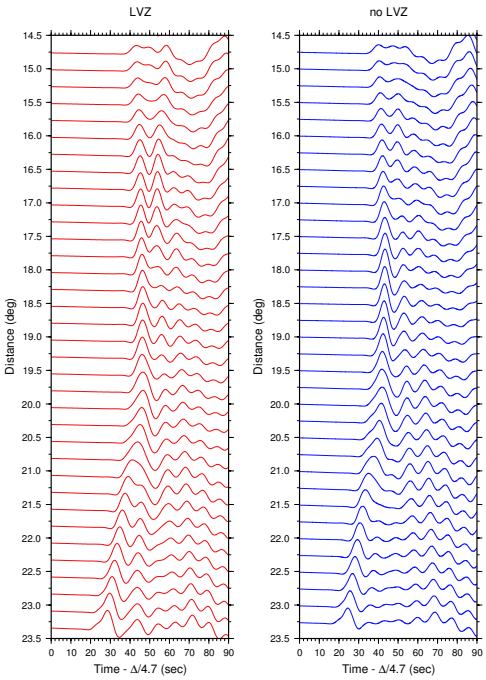

Figure 4.1: Synthetics displacement waveforms from models with (left)/without LVZ (right). The LVZ contains a dV_S = -5%, H_{LVZ} = 40 km layer just above the 410.

Upper mantle triplications were one of the first observations used to constrain the upper mantle seismic discontinuity structure (**??**). Because of the relatively sharp increase in velocity, the seismic wavefield bifurcates into multiple branches (see Fig. 4.1A, Fig. 4.1B). The 410 seismic discontinuity produces the secondary arrival before 17°, which are refraction/reflections from the 410, named the CD and BC branches, respectively, while the waves traveling shallower in the upper mantle are called the AB branch. While most current studies focus on travel time tomography and receiver function studies, it is a useful complement also to analyze seismic triplications, which are very sensitive to mantle structure where seismic waves travel horizontally. Introducing a low velocity zone not only increases the separation of AB and CD branches, but also extends the AB branch beyond 22°. We illustrate an example of an upper mantle triplication at 16°-23° to display the usefulness of these data in constraining the velocity structure near the 410 (Fig. 4.1C).

Two relevant branches will be discussed here, AB (slow) and CD (fast). The separation of these two branches is very useful to constrain the velocity, while their

relative amplitude is helpful in determining the velocity gradient. The crossover of the AB and CD branches is used to determine the depth and size of the discontinuity. The back-branch AB is particularly useful in determining the velocity and its gradient near the 410 (**???**). The moveout and amplitude of the forward CD branches beyond the crossover of the AB and CD indicates the velocity and its gradient below the 410 seismic discontinuity.

One important aspect of the AB branch is the position of triplication point B, since it is relevant to where the velocity gradient starts to decrease or whenever the low velocity zone exists atop the 410. It was observed that the AB branch crosses over with the CD branch and appears from 19°-20°. It disappears near 22° (**?**) because the velocity gradient is relatively steep, forcing shallow turning depths. However, if the AB branch crosses over with the CD branch at larger distances and emerges at 22°, it indicates a decrease in velocity gradient occurring at depth, which provides the best evidence of a low velocity zone atop the 410, along with timing of the CD and AB branches. In other words, we can potentially determine the thickness of the low velocity zone. With the help of the timing between the AB and CD branches, we can determine the velocity reduction of the LVZ and its thickness although there are trade-offs. Note that the uncertainty of the depth of shallow earthquakes produces relatively small differences in the frequency band of 0.01-0.2 Hz (**?**) and does not obscure the delayed AB branch. In addition, the source mechanisms for the events we used are primarily strike-slip events and the radiation pattern is favorable for observing SH waveforms even if minor differences in source mechanisms are allowed. However, observing these relatively subtle differences requires dense arrays with station spacing less than 30 km.

PASSCAL broadband seismic experiments have been greatly increasing during the past decades. Mostly these data are used to study regional crust and mantle structure, with the help of receiver functions (**?**) and travel time tomography (**?**). Sometimes, surface wave tomography is also performed to understand the regional tectonics (**?**). In most cases, the spacing of the arrays is much shorter than global and permanent regional networks. Such arrays in fact provide dense sampling in the

regions of interest. We have first analyzed broadband waveform data for the permanent TriNet seismic broadband array in southern California and several PASSCAL arrays, including La Ristra array, CDROM array, and with example observations displayed in **?**. In general, the spacing of the temporary arrays is about 20 km or less and the spacing of the TriNet is on average 50 km and sometimes less than 30 km. Detailed descriptions about the purpose of these passive source seismic experiments (PASSCAL) are summarized in **?**. We will illustrate how to model such dense arrays to retrieve information about the velocity structure from the waveform modeling of upper mantle triplications. Note, also, that we use triplications of direct S waves, which give a better spatial constraint than using triplications of multiple S waves, such as SS, SSS and SSSS (**????**). In addition, we benefit from the dense networks with station spacing less than 20 km, which is an order of magnitude better than that in previous studies. We review some of the 1D modeling results supporting the existence of the LVZ (**?**)) (Fig. 4.2) followed by 2D simulations from the 3D tomographic study by **?** of paths passing through the anomalous region. Next, we introduce a new 3D hybrid method for waveform modeling and model the TriNet data producing a 3D image of the western edge of the proposed LVZ beneath the western Basin and Range.

4.2 Data and Waveform Analysis

4.2.1 Waveform modeling with 1D layered models

We first compute full 1D (ωk) frequency-wavenumber waveform synthetics (**?**), and model the direct S wave triplications at epicentral distances of 14°-17° and explain the timing and amplitude of multiple arrivals coming from fine structures near the 410. We apply the 1D attenuation structure suited for the Western United States and East Pacific Rise (**?**). At these distances, we first modify the shallow mantle structure from the 1D model to fit the timing and amplitude of S waves and Love waves (**?**). By adding a 20 km lid of 4.55 km/s, we are able to fit most recorded sections collected

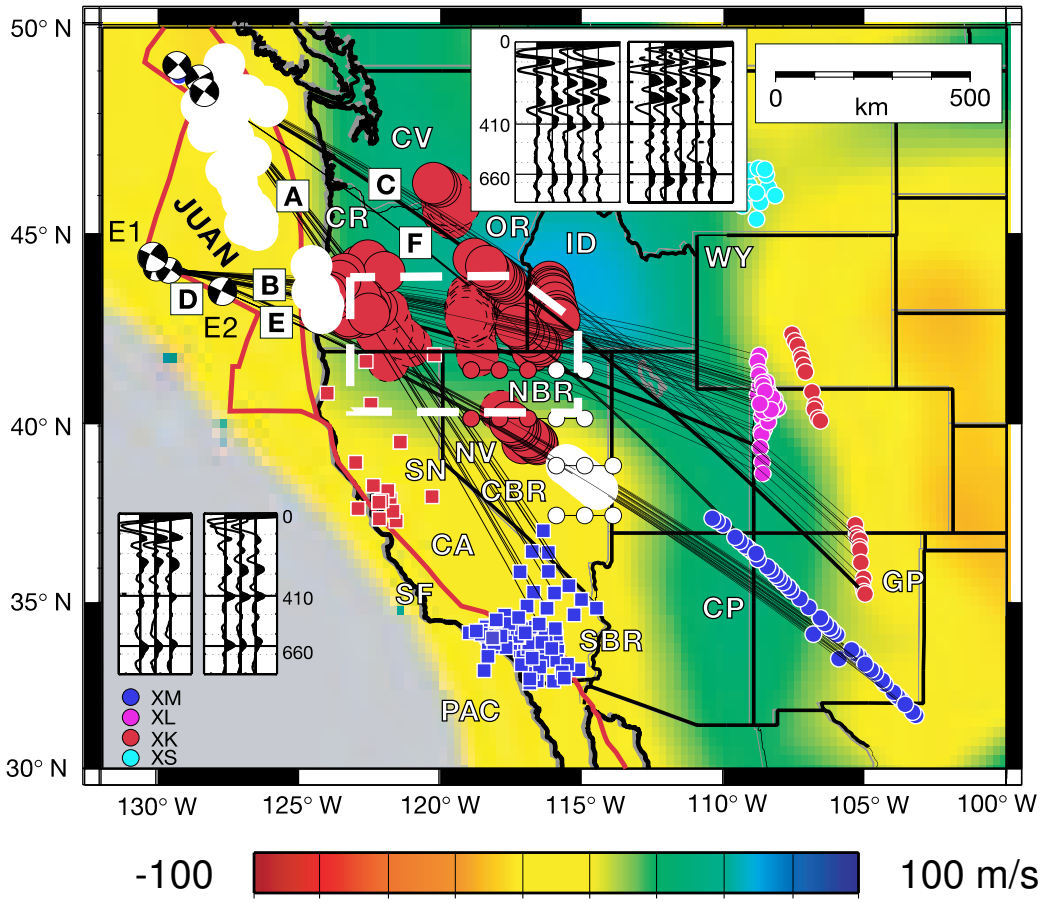

Figure 4.2: Low velocity region atop the transition zone in the western US (**?**). Velocity anomaly imaged by **?** at 400 km is shown in color. Red patches indicated the sampled low velocity zone and their size corresponds to the Fresnel zone of 6 secs S wave. Small red dots are locations where anomalous negative pulses are observed in receiver function profiles (**?**). White patches and white dots show no sign of LVZ in triplication study and receiver functions.

Path	Event date	Lon	Lat	Depth	Strike	Dip	Rake	Mw
A	01/09/14	-128.59	48.82	6.0	330	84	-176	5.9
B	97/07/11	-129.65	44.11	6.0	301	87	-172	5.4
C	99/07/02	-129.38	49.13	6.0	315	81	176	5.9

Table 4.1: Source parameters

in the Western United States (?). With a better constraint on the shallow mantle structure, we then further model the differences in the CD branch between data and synthetics. To resolve the tradeoffs between discontinuity topography and mantle velocity directly above or below the discontinuity, we model S wave triplications at epicentral distances of 21°-24°. A LVZ atop the 410 produces a secondary pulse not normally seen at these distances, as discussed earlier. Using this secondary pulse as a proxy for the existence of a LVZ atop the 410, we examine waveforms recorded by the TriNet broadband network and several temporary PASSCAL broadband arrays from evens offshore of Washington-Oregon, United States. Perturbed velocity models near the turning point of the CD branch are generated as a sensitivity study. The size of the perturbed features are estimated as the size of the Fresnel zone in both along-path and cross-path directions. These zones are represented by the colored circles in the mapping (Fig. 4.2). This issue will be addressed later in 3D simulations. Here we discuss modeling results along path A, B, and C (Fig. 4.2).

Record section A (event 010914, Table. 4.1) shows typical waveform characteristics sampling this area at epicentral distances of 14°-17° (Fig. 3.8). It samples the region beneath the California-Oregon border. Relative to the 1D reference model (on the left), we observe a considerable increase of separation in timing between the AB branch and the CD branch of about 5 seconds. At these ranges, the branch AB represents the S wave propagating through the upper mantle and turning a depths between 200-300 km and the CD branch represent the S wave bottoming near the 410. Record section B (event 970711, Table. 4.1) trends more east-west, samples the same regions and shows similar waveforms to those in record section A.

Synthetics calculated from a perturbed 1D model with the 410 depressed by 60

km (model Topo) improves the differential time between the AB and CD branches considerably but disagrees with the receiver functions addressed earlier. Model gradient B produces reasonable fits except the CD branch is too strong near 16° as is the case for model LVZ. Model LVZ+Topo fits data well both in timing and amplitude.

These two paths sample regions close together in space and appear to have a common explanation, namely, a low velocity zone. Although it is clear that the velocity is slow just above the 410, it is not easy to distinguish which model explains the waveform data better with only data in this limited range. The synthetic predictions at larger ranges sampling the extended AB branch is effective for this purpose (Fig. 3.10). Here we illustrate how the long range data can be used to distinguish different models. As an example, we compute the synthetics along path C and the detailed comparison between data and synthetics has been presented by **?** earlier. In this example, Model Topo does not produce the observed secondary AB branch along record section C (event 990702, Table 4.1) at the distance range. Though a gradient model such as model Gradient B does produce the secondary AB branch, the amplitude and timing are different depending on which model we use. After crossover of the AB and CD branch, the gradient model often predicts an earlier emergence of the the AB branch near 21.5°. The differences between Model LVZ and Model LVZ+Topo are that the AB branch, emerging from the crossover with the CD branch, appears at shorter ranges while the CD branch is delayed near 21° due to a deeper 410.

4.2.2 Modeling complex structures

To characterize the origin of the velocity anomaly, it is useful to examine the geometry of the anomaly testing for lateral sharpness. Smooth features are usually attributed to variations in temperature. A velocity anomaly with a sharp edge is often considered to be chemically distinct or due to a partial melt (**?**). There are several cases where the velocity structure is shown to be relatively 1D within the Pacific plate (**??**). However, in this section, we will discuss the structure underneath the plate boundary in the western Basin and Range, where the velocity structure changes rapidly both in the

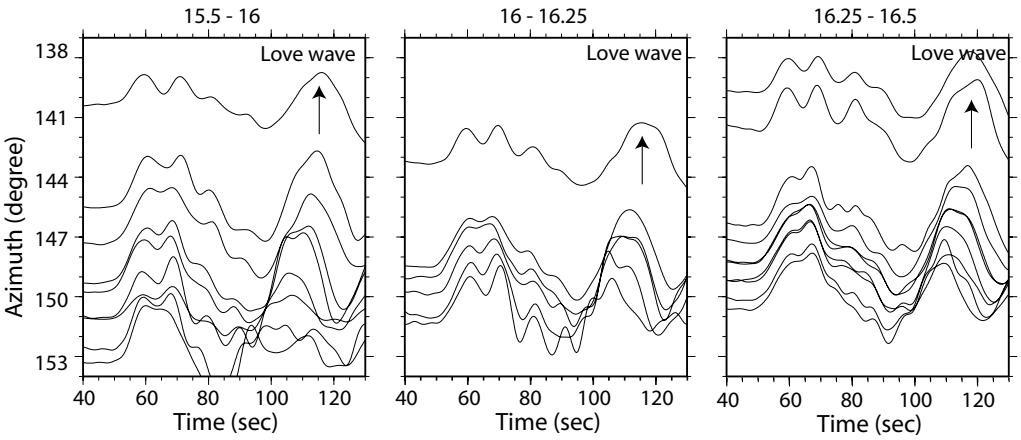

Figure 4.3: Azimuthal variations of tangential displacements (path A) recorded at the TriNet array. Azimuth sections are shown at three distance ranges: 15.5°-16°, 16°-16.25°, 16.25°-16.5°. Arrows indicate the Love wave.

shallow upper mantle and above the transition zone.

In this section, we have increased the time window to include the beginning of the Love wave as displayed in Fig. 4.3. Note that the later arriving Love wave is delayed by about 10 to 12 secs along inland paths (Az = 141°) compared to coastal paths (Az = 150°). This observation is consistent with a model where the lid increases its thickness from inland California to coastal California (**?**). At 15°-17°, a slower, thinner lithosphere should slow down AB more than CD and make the phases closer together. However, the data indicates that CD is delayed more than the AB at inland paths, requiring variations in deep upper mantle structure.

We pick the AB and CD travel times and construct a map of differential times as a function of distance and azimuth (Fig. 4.4). With some complexities in mind caused by the slow uppermost mantle structure beneath the Sierra Nevada (**?**), we see

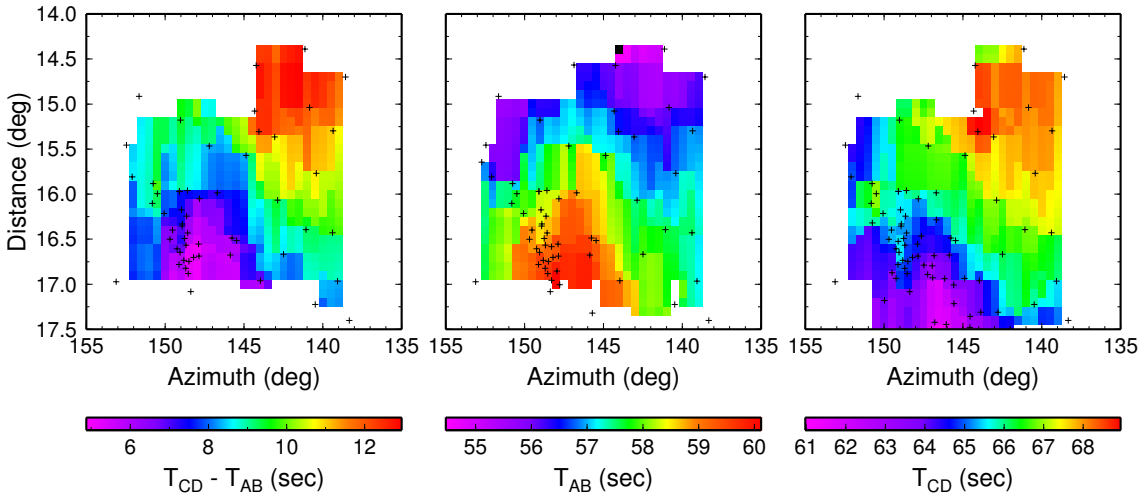

Figure 4.4: Azimuthal variations in handpicked travel time of AB branch (T_{AB}), CD branch (T_{CD}) and T_{AB}-T_{CD} at epicentral distances of 14°-17° (path A). Crosses indicate the positions of stations.

similar separations moving along constant distance or azimuth, except for the data near 15° where the CD branch becomes difficult to pick.

We introduce some TriNet data sampling the western edge of this interesting structure (Fig. 4.5). The blue and green traces are observations along record sections of constant azimuth while the red traces are along constant distance. The latter style of plotting data is commonly referred to as a "fan shot", a technique used to detect low velocity salt plugs in exploration. These recordings contain two pulses associated with an earlier shallow upper mantle arrival with a slow move-out (labeled AB) and a secondary arrival (CD) with a fast move-out, bottoming below the 410 discontinuity.

To model these records requires accounting for significant shallow structure and including 2D and 3D models. We found the 2D finite-difference (FD) code with embedded earthquake sources quite useful for this purpose (**??**). If we applies the moving window approach introduced by **?**, one can generate FD synthetics with computation times faster than 1D ωk synthetics. This approach allows us to propagate waves efficiently through 2D sections of tomographic models to generate synthetics. We note that a particular choice of a tomography model is likely to introduce some bias in

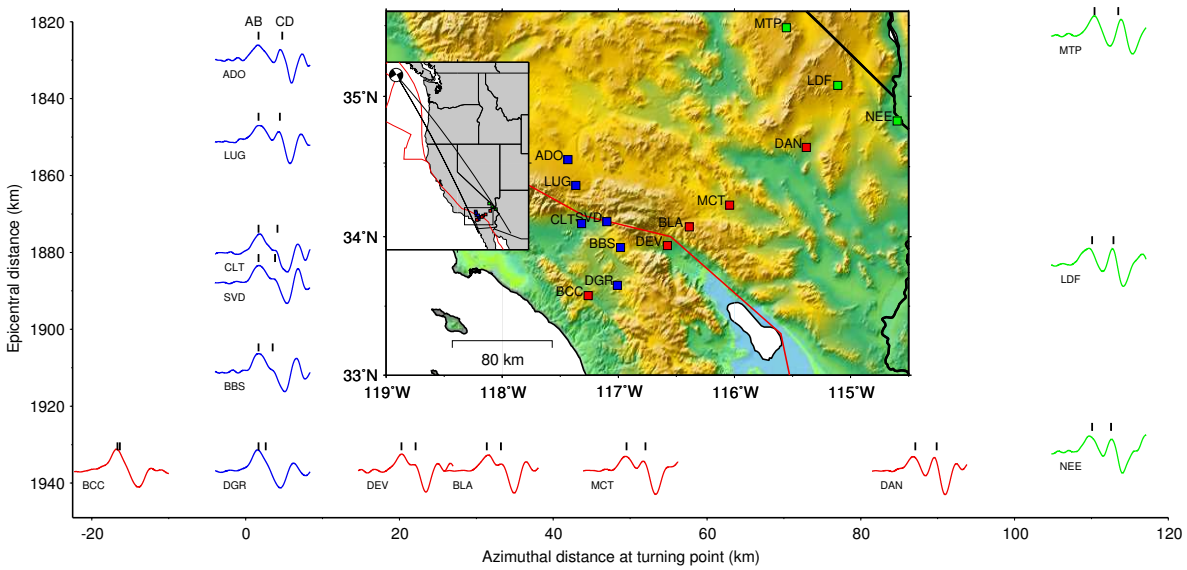

Figure 4.5: 3D variations in upper mantle triplications recorded at TriNet (path A). A subset of data is plotted against azimuth (138°-155°) and epicentral distance (16.3°-17.5°, 1820-1950 km). Blue traces indicate a distance section with normal moveout of AB and CD branches. Green traces indicate a distance section with anomalously delayed CD branches. Red trances show an azimuth section where the interferences of AB and CD branches are very similar to a distance section but changing in azimuth. Each trace is 40 secs and vertical bars mark the arrivals of AB and CD branches. The locations of these stations are shown in the topographic map of Southern California, with a inset showing great-circle-paths from the source to the east and west California.

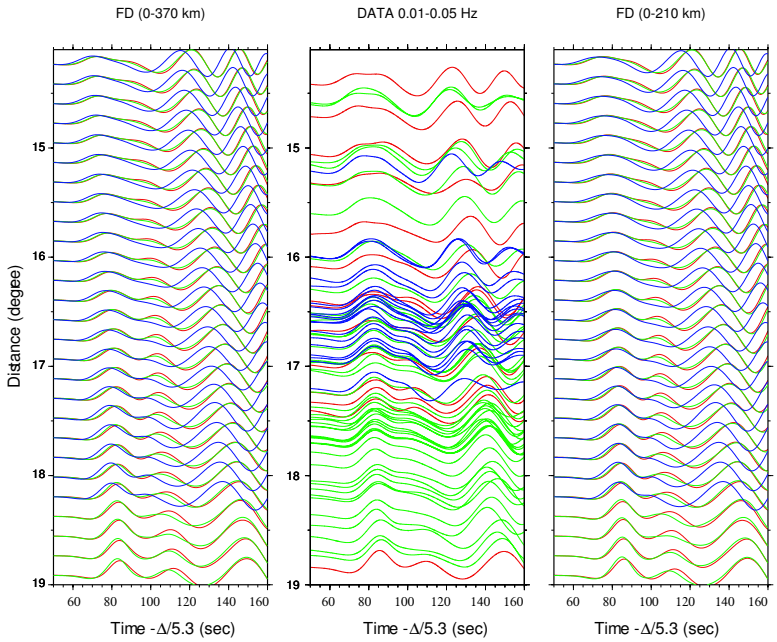

Figure 4.6: Comparison of data and finite difference (FD) synthetics at long periods (0.01-0.05 Hz). Coastal, middle and inland sections are plotted in blue (Az = 145°-147°), green (Az = 143°-145°) and red (Az = 137°-143°) (middle panel). FD Synthetics are computed for the 2-D slice cut from surface wave tomography model (**?**). Left panel: Velocity anomaly at the top 370 km of upper mantle is included in the FD synthetics. Right panel: Velocity anomaly at the top 210 km of upper mantle is included in the FD synthetics.

constructing our model. But the modeled velocity contrast across different azimuths should be rather robust. The recent tomographic model by **?** predicts the changes in Love waves across the array well, which serves a reasonable correction for shallow structure (Fig. 4.6). The data are color coded to emphasize the difference between eastern and western paths. Since this particular tomographic model was constructed from fundamental surface wave modes only, with limited depth resolution, we have generated two models. The first (left) contains their model down to 370 km and then becomes TNA, while the model on the right changes at a depth of 210 km. Since they produce similar results, we will adopt the (210) version on the right as a reasonable correction for shallow structure.

Below this depth, we used TNA for West Coast stations and the model displayed in Fig. 4.7 for the easternmost stations. We note that there is a tradeoff between

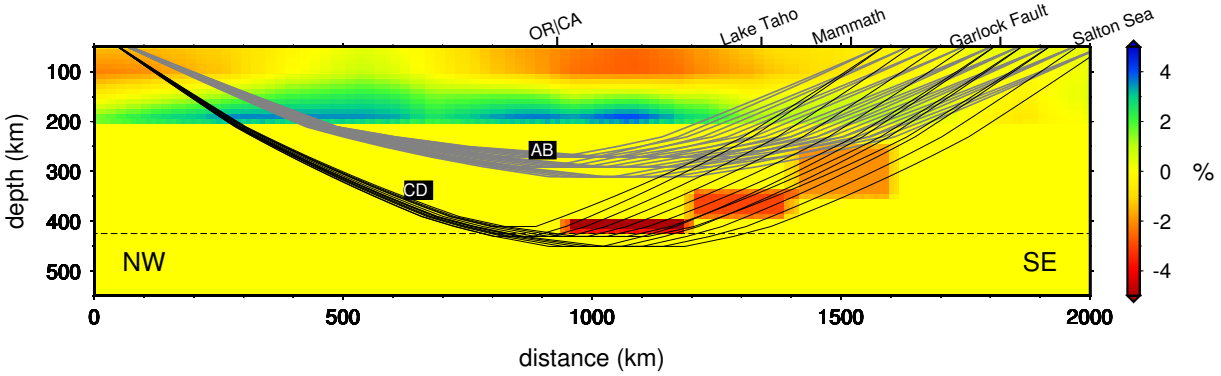

Figure 4.7: 2-D low velocity zone model along inland California (Az = 137°-143°). Velocity anomaly at each block from the bottom to the top: $dV_S = -5\%$, $dV_S = -4\%$, $dV_S = -3\%$. Raypaths of AB and CD branches are shown for references.

the spatial location of LVZ and the depth of the 410. When the 410 is deeper by 10 km, the LVZ structure moves further to the source side by 100 km. When the 410 is shallower by 10 km, the LVZ structure moves further to the receiver side by 100 km. In this case, we set the 410 at the depth of 420 km, which is very similar to other estimates near the region (**?**).

Our preferred model has been slightly modified from the LVZ model discussed earlier to explain the southernmost TriNet stations better. In particular, stations in the Owens Valley are less anomalous although they are late relative to coastal stations probably caused by shallow mantle structure beneath the Sierra Nevada (**?**). These two models fit the data along the east and west pure paths as displayed in record sections given in Fig. 4.8. We have included a comparison of the more inland data with the model lacking the LVZ to show the obvious mismatch.

The observations at mid-azimuths (Fig. 4.5, red traces) fit neither model although they appear to be a combination of the two models or essentially involving 3D propagation. To correct for these effects, we generate four 2D synthetics, which are weighted according to their position in the extended Fresnel zone (Appendix A, Fig. 4.16). The method is similar to that introduced in **?** except it uses numerical synthetics instead of analytical ones. Thus, the contribution from the lit region is broadband while those

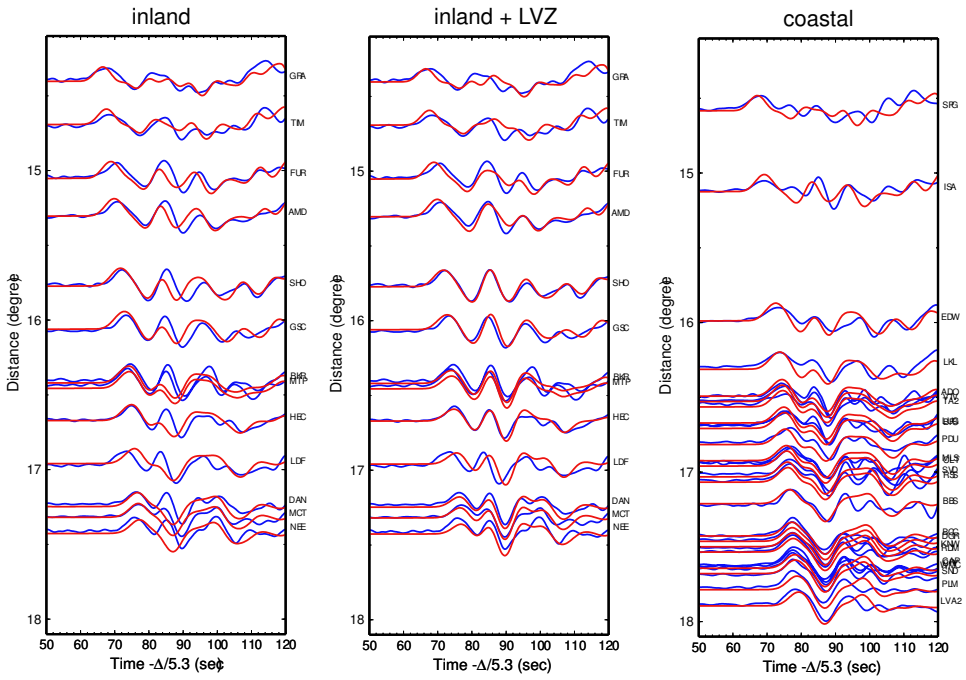

Figure 4.8: Comparison of data sections and FD synthetics along inland paths (Az = 137°-143°) and coastal paths (Az = 145°-147°). Left panel: synthetics from 2D slices without LVZ. Middle panel: synthetics from 2D slice with LVZ. Right panel: synthetics from 2D slices without LVZ. Data are plotted in blue and synthetics in red.

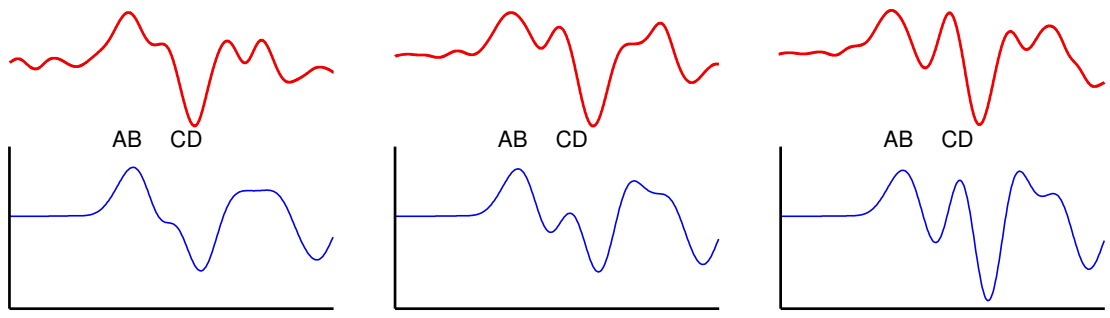

Figure 4.9: Data (top panel) vs. Diffracted finite difference synthetics (DiFD (bottom panel). From left to right: DEV (Δ=17.3°, Az=144.5°), MCT (Δ=17.3°, Az=142.7°) and DAN (Δ=17.2°, Az=140.5°). Each trace is 40 secs long.

outside sample the diffracted zone and have their high frequencies removed. We refer to these approximate 3D synthetics as DiFD for convenience. This technique has been validated against SEM (**?**) in a similar application by **?** and produces satisfactory results. Here we generate DiFD synthetics at a constant distance, 1960 km, and compare with data recorded at different azimuths (Fig. 4.9).

The data show systematic changes in the timing and amplitude of the CD branch. The westernmost record (DEV) can be explained with the tomographic model by **?** while the easternmost station (DAN) can be explained with the low velocity zone model. The middle trace (station MCT), however, cannot be explained by either model since the CD branch arrives slightly earlier with smaller amplitude. Instead of generating more 2D models, we explore the synthetics by combining the two models into a 3D structure using the DiFD. The 3D model has a sharp edge, which separates the western side (normal velocity structure) from eastern side (low velocity zone model). For a station sitting directly above the boundary, each side contributes about half of the response and this synthetic explains the middle trace quite well (Fig. 4.9). We display typical comparisons against observations with the middle traces in Fig. 4.10. Though few recordings are shown in this swath, we find the DiFD synthetics predict the separation of the AB and CD branches better near 15.5° and generate a shoulder near 17°-18° compariable to the data.

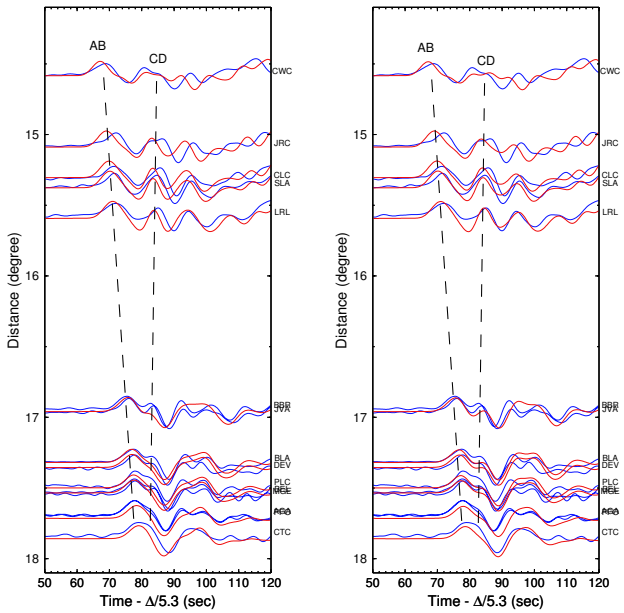

Figure 4.10: Comparison of data sections and DiFD synthetics along complex middle paths (Az = 143°-145°). Left panel: synthetics from 2D slice without LVZ. Right panel: LVZ/no LVZ boundary directly below the section. Data are plotted in blue and synthetics in red.

Model Type	az 137-143 (11)	az 143-145 (15)	az 145-147 (24)	az 137-147 (50)
2D	0.58±0.09	0.79±0.14	0.82±0.10	0.76±0.15
2D+LVZ	0.73±0.16	0.69±0.19	0.63±0.16	0.67±0.17
3D	0.69±0.12	0.76±0.14	0.74±0.11	0.80±0.12

(): No. of stations

Table 4.2: Correlation coefficient between data and synthetics

The boundary separating these two structures is obviously more complicated than modeled here but the general behavior appears to be explained. To systematically locate the boundary of such low velocity zone structure, we compute five synthetics for each station according to their position relative to the boundary (Fig. 4.16) and cross-correlate with the data (Fig. 4.11). Following this modeling strategy, we are able to delineate the likely location of the boundary since the total contribution from the lit zone and the diffraction zone is different depending on the location of the boundary. Also, we assume the boundary is simply vertical in this analysis.

The best-fitting synthetic is given in the middle and the poorest-fitting synthetic on the right. We have included a cross-correlation measure as a goodness-of-fit criterion (Table. 4.2).

In general, the first 25 secs fits quite well, which is controlled by the AB-CD interference which is our primary interest. Also, we perform Kruskal-Wallis non-parametric one-way analysis to test the significance of the differences among different models (Table. 4.3). Clearly, the 2D model with LVZ fits the inland data (Az = 137°-143°) significantly better than the 2D model at the 95% confidence level (Table. 4.3). However, it fits the coast data (Az = 145°-147°) much worse at the 95% confidence level (Table. 4.2). Overall, the 3D LVZ model with a vertical boundary fits the whole dataset significantly better than 2D model with LVZ at the 99% confidence level (Table. 4.3). The 2D model with no LVZ seems to fit the whole data almost equally well simply because a large number of stations (24) is located within the coastal swath.

In general, data recorded on the eastern side of the Californa shear zone can be explained with a boundary of low velocity zone located north of Lake Tahoe. Some

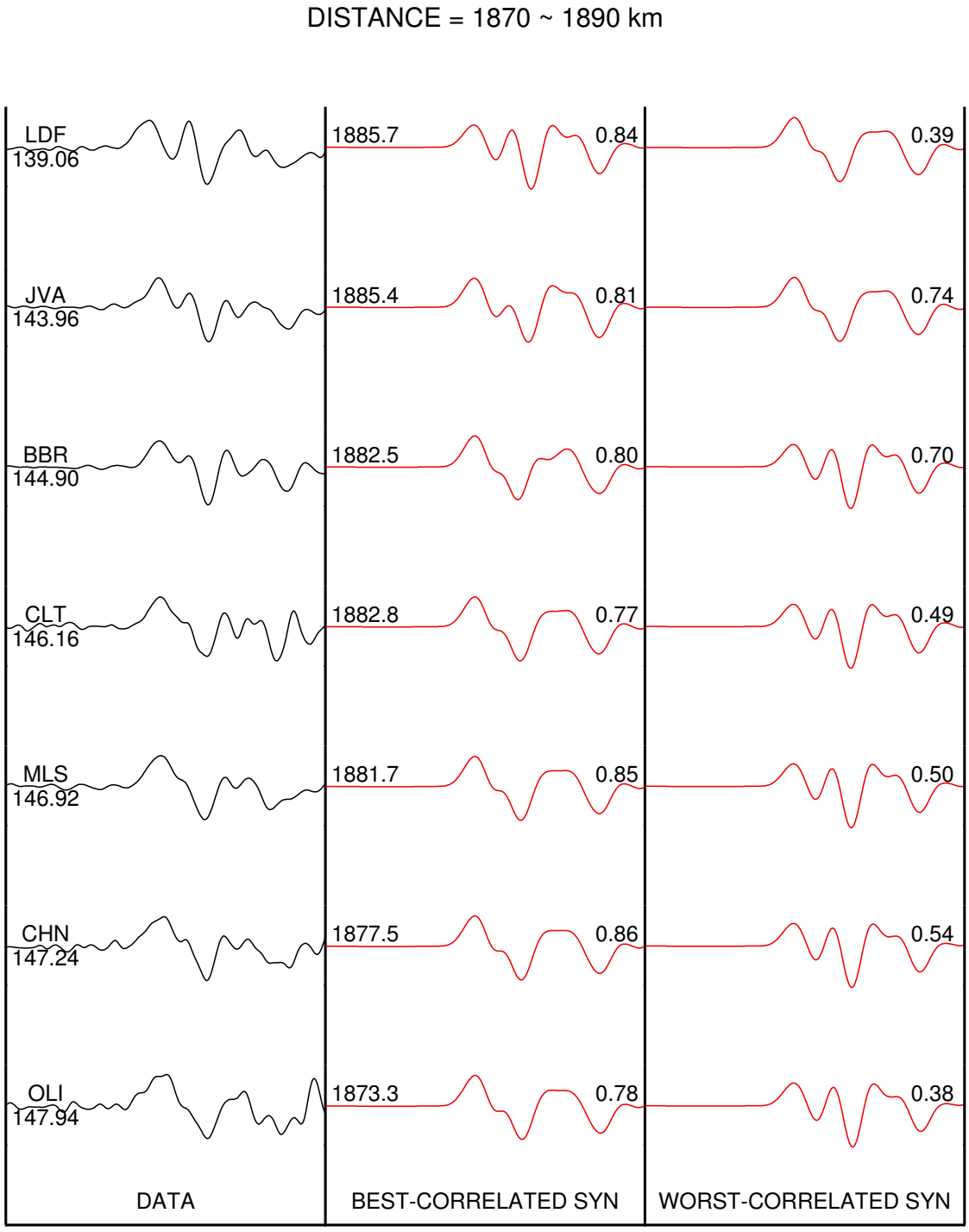

Figure 4.11: Cross-correlation between data and synthetics at epicentral distance of 16.8°-17°. Left panel: Data. Middle panel: Best correlated DiFD synthetics. Right Panel: Worst-correlated DiFD synthetics. Azimuth of each station is shown below the trace. Cross-Correlation coefficient is shown above each synthetic.

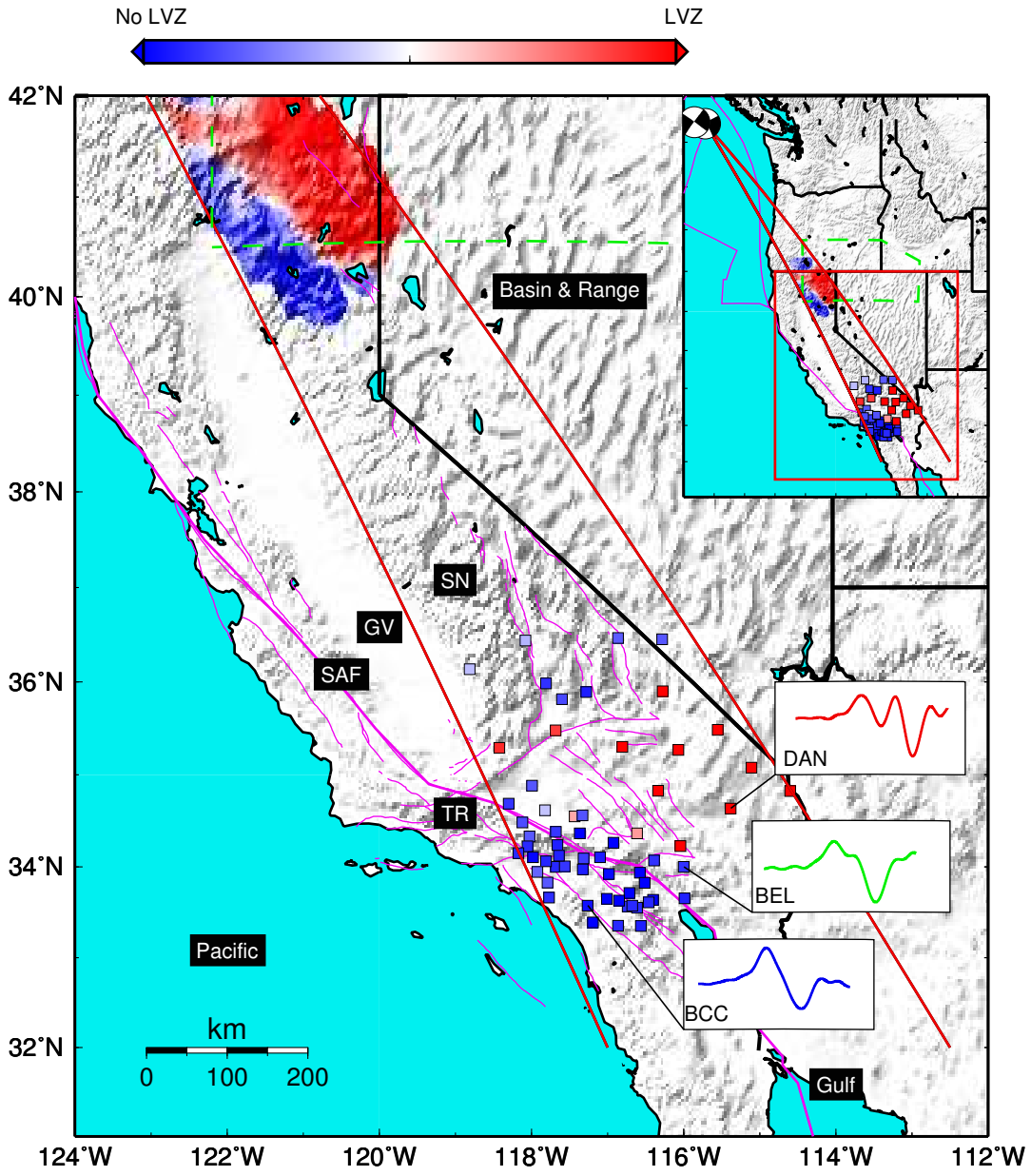

Figure 4.12: Map of low velocity zone atop the 410 beneath the western Basin and Ranges. Typical waveform recored across TriNet are shown for station DAN (Δ=17.3°, Az=140.5°), BEL (Δ=17.5°, Az=143°), BCC (Δ=17.4, Az=146.7°). Data best fitted by the 3D LVZ model where the edge of LVZ is on the eastern/western side of the station beyond the lit zone are plotted in dark blue/dark red. Data best fitted by the 3-D LVZ model where the edge of LVZ is on the eastern/western side of the station within the lit zone are plotted in light blue/light red. Inset on the upper right includes the source-receiver geometry.

Model Type	az 137-143	az 143-145	az 145-147	az 137-147
2D, 2D+LVZ	95%	94%	95%	97.5%
2D+LVZ, 3D	30%	69%	95%	99%
2D, 3D	80%	30%	84%	62%

Kruskal-Wallis nonparametric one-way analysis of variance

Table 4.3: Confidence level of model differences

of the stations north of the Garlock fault plot as blue suggesting they might sample the structure to the north of the anomalous zone. These paths primarily sample regions beneath southern Oregon, northern California and the western end of the Basin and Range. We conclude that this sharp velocity contrast in the deep upper mantle between easternmost and central northern California is very robust and the velocity decreases rapidly from the east to the west at the scale of less than 100 km.

4.3 Discussion

Recently, **?** analyzed receiver function profiles across Nevada-Idaho-Montana and found a negative polarity pulse approximately 30 km above the converted pulse from the 410. This section is very close to the area sampled by the path C discussed earlier. **?** also presents similar results beneath NW Colorado suggesting a 5% velocity reduction 30 km atop the 410. As we have shown previously (Fig. 3.10), a low velocity gradient in the deep upper mantle can also produce a secondary AB branch at the distance of 21°-23°. However, the onset of the AB branch appears earlier than the LVZ model and its amplitude is too large. Also, the gradient models are not consistent with the receiver function profiles in the western US ((**?**), Fig. 4.2, where a negative pulse appears before the converted phase from the 410. Our analysis indicates that the western margin of the LVZ is sharp, less than 100 km. An alternative interpretation of our findings is that the deeper upper mantle in fact is faster along the coastal path due to the existence of dipping Gorda slab (**?**) beneath the northern California, although this would not produce negative peaks observed in receiver function profiles (**?**). If it is true, the dipping fast slab will advance CD branch more than AB branch

and decrease their separation, which has been modeled well with current tomographic model (**?**). Therefore, we prefer the LVZ model but do not rule out this alternative interpretation

However, low velocity zones atop the 410 have been suggested in many other regions. **?** constructed reflectivity profiles in China and found 5% impedance decrease underneath northeast China and the Sea of Japan, where the flattened slab is stagnant in the transition zone (**?**). **?** produced a tomography image beneath the Tornquist-Teissyre zone in the western boundary of the Russian platform. They found a low velocity zone exists beneath this ancient subduction of a wide Tornquist ocean plate between the Baltica and Avalonia shields. These observations are consistent with the idea that these low velocity zones are related to subduction zones, including Farallon plate subduction underneath the Westen US. **?** suggest that the trailing edge of the Farallon plate that subducted beneath the wester US is currently flat-lying in the transition zone. If such low velocity zones represent some molten layer sitting above the transition zone, dehydration melting could play a very important role in generating these melts. It is possible that some water is transported by downgoing slabs into the transition zone (**?**). In particular, a cold slab can be the likely candidate keeping the hydrous silicates stable and carrying water into the transition zone (**??**). **?** have shown that the average mantle tempeature of 1473 K would pass the dehydration reaction of hydrous wadsleyite, but phase E is a stable phase at cold mantle temperaure of less than 1473 K. Above 1473 K, that is, at normal mantle temperature in the transition zone, the dehydration of hydrous wadsleyite can produce a hydrous plume and affect the chemical differentiation of the upper mantle (**?**). As suggested by **?**, a stagnant slab in the transition zone is a good reservoir in preserving dense hydrous magnesium silicate, phase E, at temperature less than 1473 K. **?** estimated that the edge of the Farallon plate that subducted beneath the western US could currently be 200 K colder than the surrounding mantle, allowing the Farallon slab to dehydrate in the transition zone, consistent with the existence of an LVZ atop the 410-km discontinuity.

4.4 Conclusion

We model the upper mantle triplication associated with the 410 seismic discontinuity and find a low velocity zone (5%) above the transition zone consistent with observations and receiver function profiles in parts of the western US. This zone varies in thickness from 20 to 90 km and covers an area from southwest Oregon to central Nevada and extending into northernmost California, roughly a 10° square. Our analysis indicates that the low velocity zone pinches out beneath the western edge with a relatively sharp boundary. Such a structural model produces synthetics with AB versus CD interferences equally strong in distance and azimuth as observed. In mapping out this LVZ we found that the existence of the AB branch at distances beyond 21° is a particularly useful criterion. Thus, a global search of this portion of the triplication could prove valuable in a mapping exercise and provide constraints on the spatial extent of low velocity zone in the deep upper mantle.

4.5 Appendix

4.5.1 Finite difference

To further constrain the lateral extent of the LVZ, it is necessary to go further beyond 1-D modeling. Here we adopt the 2-D finite difference method developed by **?** and **?**. No attenuation is implemented in the 2D calculation, which might cause over-prediction in the amplitude of AB branches. In the case with no attenuation, the FK wavenumber synthetics produce a very good match with finite difference synthetics (Fig. 4.13). In addition, the finite difference synthetics will over-predict the higher mode associated with the existence of low velocity zone beneath the lithosphere because of the approximate spreading correction. However, we find it is quite useful for our purposes to compute proposed tomographic models and examine their influences on the beginning of the Love waves and the interferences of mantle triplications.

4.5.2 Diffracted Finite difference (DiFD)

While 2-D modeling has shown its usefulness (**?**), however, it can not take into account possible 3-D effect, such as out-of-plane multipathing. To overcome such problems, **?** proposed an approximate algorithm to include responses off the great circle path using 2-D WKM (**?**). Here we illustrate some of the approximations implemented in the 2-D finite difference calculation. We apply the well-known 2D to 3D mapping approximation

$$\Psi(r,z,t)_P = \sqrt{\frac{2}{r}}\frac{1}{\pi}\left[\frac{1}{\sqrt{t}} * \Psi(r,z,t)_L\right] \tag{4.1}$$

where $\Psi(r,z,t)_L$ is essentially a line source response containing a double-couple source (Helmberger and Vidale, 1988) and can be computed with the Finite Difference Method in a 2-D velocity model . To obtain a point source response $\Psi(r,z,t)_P$, simply convolve with an $1/\sqrt{t}$ operator. However, this only accounts for variations in velocities along the Great Circle Path (GCP), where the structure is assumed to be uniform, 2D, at right angles to the plane of propagation.

To estimate the 3D contributions we invoke Huygens' principle, which states the disturbance at some later time can be obtained by summing secondary sources on the reference surface S. In this case, responses off GCP are included. It can be shown that the 2-D Kirchhoff integral over the 3-rd dimension simply represents a $1/\sqrt{t}$ operator if the structure is truly 2D. The procedure is outlined in Fig. 4.14 with the geometry displayed in (A). To add energy coming from paths outsides the GCP, we simply sum-up contributions along the other paths, essentially a line integration (step B). This response can be written as

$$\phi(t) = \frac{1}{2}\frac{d\theta}{dt} + \frac{1}{2}\frac{d\theta}{dt}, \tag{4.2}$$

where the angle θ sweeps out paths to the left and to the right. The strongest response comes from $\theta = 0$, or the geometric arrival time (t_0), namely

$$\frac{d\theta}{dt} = \frac{H(t-t_0)}{\sqrt{t-t_0}}, \tag{4.3}$$

where t equals the travel time from any point on the line to the receiver. If the field along the line Γ is uniform (independent of azimuth), this line integration produce a $\frac{1}{\sqrt{t}}$ convolution which is that given by equation (1). However, if the left is delayed relative to the right, we obtain a split response as discussed in **?**.

Thus, to take into account variations in velocities in the 3-rd dimension, 2-D Kirchhoff line integral is performed to sum all secondary sources at a reference plane S along the line Γ (Fig. 4.15). In short, we replace $\left[\frac{1}{\sqrt{t}} * \Psi(r,z,t)\right]$ in (1) with

$$\frac{1}{2}\sum_{i=1}^{n}\left[\frac{H(t-t_i)}{\sqrt{t+\Delta t_i}} * \Psi_i(t) - \frac{H(t-t_{i+1})}{\sqrt{t+\Delta t_{i+1}}} * \Psi_{i+1}(t)\right], \tag{4.4}$$

where t_i is the arrival time of path i; Δt_i is $t_i - t_o$; t_o is the arrival time along GCP and $\Psi_i(t)$ is the response computed for path i; n is the number of secondary sources considered. $1/\sqrt{t+\Delta t_i}$ becomes a frequency dependent weighting factor. Several assumptions are made:

(a) Reference plane S is placed atop the anomaly interested.

(b) Velocity variations in the domain of interest are effectively 2-D except the anomaly of interest.

(c) The receiver is sufficiently far away from the diffractor ($T \gg \tau$, T is travel time and τ is period of signal).

4.5.3 Estimate zone of influence

Define the Fresnel zone limit as

$$X_f \approx \sqrt{h\alpha T}, \tag{4.5}$$

where h is the depth of reference plane; α is mean velocity between the reference plane and surface and T is the duration of signal. The region inside X_f is defined as the Lit region and the region outside as the Diffraction region. Define the lit operator as

$$O_L(t) \equiv \frac{d}{dt}\left[\left(\frac{H(t)}{\sqrt{t}} - \frac{H(t-t_f)}{\sqrt{t+\Delta t_f}}\right) * \dot{D}(t)\right], \tag{4.6}$$

where t_f is the arrival time corresponding to the Fresnel limit; Δt_f is $t_f - t_o$; t_o is the arrival time for GCP. Define the diffraction operator as

$$O_D(t) \equiv \frac{d}{dt}\left[\frac{H(t-t_f)}{\sqrt{t}} * \dot{D}(t)\right]. \tag{4.7}$$

In this case, the diffraction operator produces the long period signal coming from the secondary sources off GCP along Γ.

To find sharp velocity contrast in the mantle, given a seismic array at the surface, we can use this method to delineate where is the sharp boundary relative to a particular observation. Define

$$u_l^D \equiv O_D(t) * \Psi_l^D \tag{4.8}$$

$$u_r^L \equiv O_L(t) * \Psi_r^L \tag{4.9}$$

$$u_l^D \equiv O_D(t) * \Psi_l^D \tag{4.10}$$

$$u_r^L \equiv O_L(t) * \Psi_r^L, \tag{4.11}$$

where u_l^D, u_l^L the responses from diffraction and lit region along Γ of the left side; u_r^L, u_r^D the response from the lit and diffraction region along Γ of the right side. For an exact 2-D structure along GCP, there is no variations along Γ and $\Psi_l^D = \Psi_r^D = \Psi_l^L = \Psi_r^L$. Displacement at receiver P can be expressed as

$$u(P) = u_l^D + u_l^L + u_r^L + u_r^D. \tag{4.12}$$

If velocity changes abruptly along Γ, line source responses Ψ_l^D, Ψ_r^D, Ψ_l^L, Ψ_r^L are calculated based upon the relative location between the assumed velocity boundary and the receiver (Fig. 4.16). With multiple receivers and multiple events, it is possible to determine the location of the boundary in parallel to locating the epicenter of earthquakes. If the waveforms changes within X_f, then the diffraction surface S has to be shallower to account for the rapid variation, which is similar to determine the

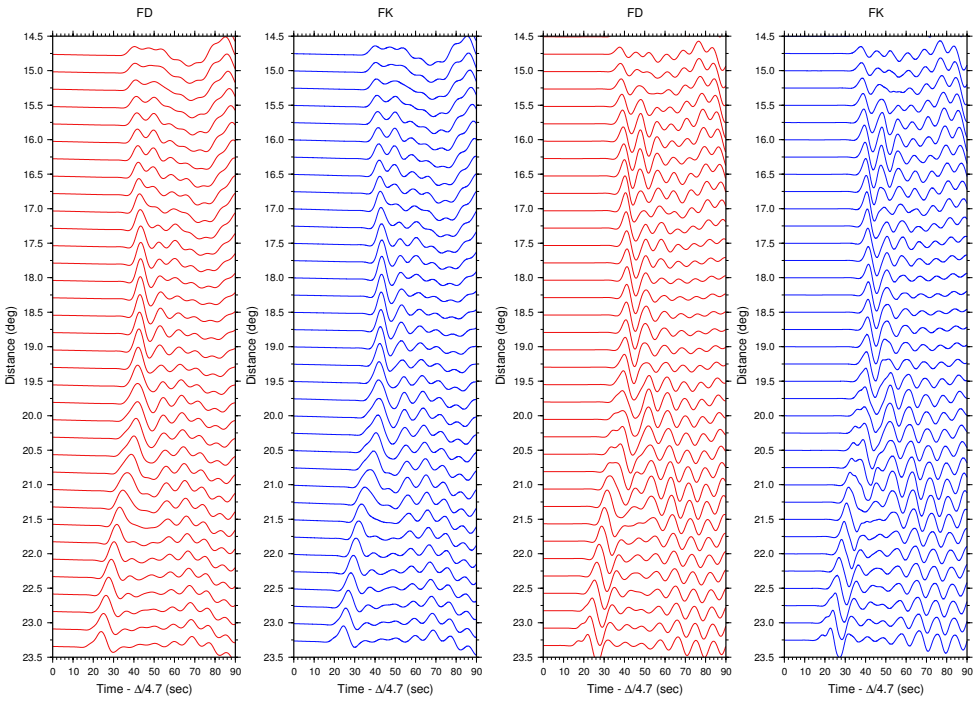

Figure 4.13: Comparison of Finite difference (FD) and frequency-wavenumber (FK) synthetics at epicentral distance of 14.5°-23.5°. Left panel: FD tangential displacement and velocity. Right: FK tangential displacement and velocity.

hypocenter of earthquakes.

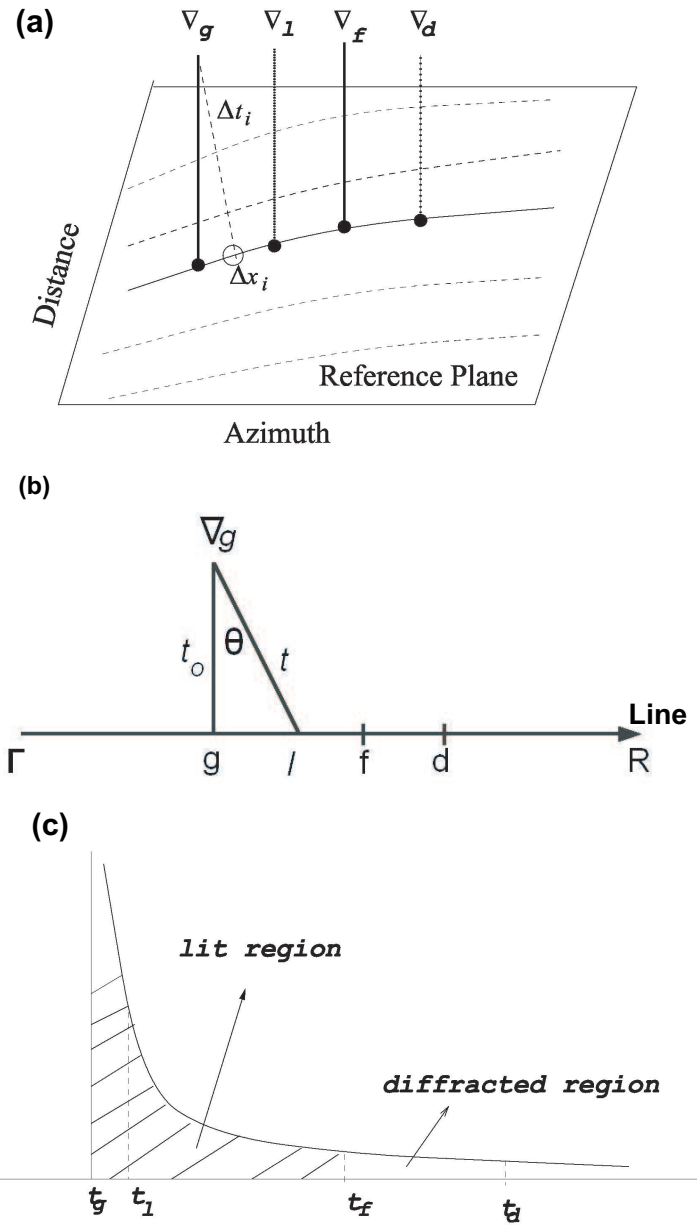

Figure 4.14: A surface of constant depth serving as a reference plane for interfacing Kirchoff solutions is presented in (a). We assume 2D geometry and integrate along the arc (heavy line) which corresponds to constant epicentral distance with variable azimuth. The other dotted lines correspond to other neighboring distances. Four locations are indicated corresponding to the surface of geometric arrival ∇_g, the Fresnel boundary ∇_f, the two virtual stations ∇_l, ∇_d representing the lit-region and the diffracted-region. The middle column (b) illustrates how the energy is added along line Γ, which is at right angle to the GCP. The lower diagram (c) displays the time corresponds to the above four positions relative to the square root weighting.

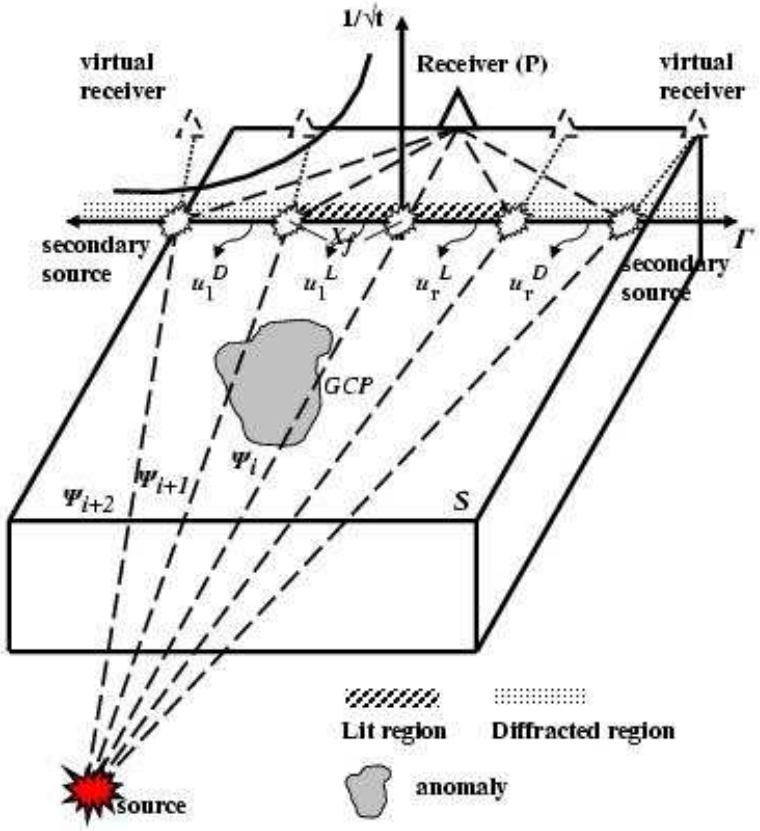

Figure 4.15: Schematic map showing the calculation of Diffracted finite difference.

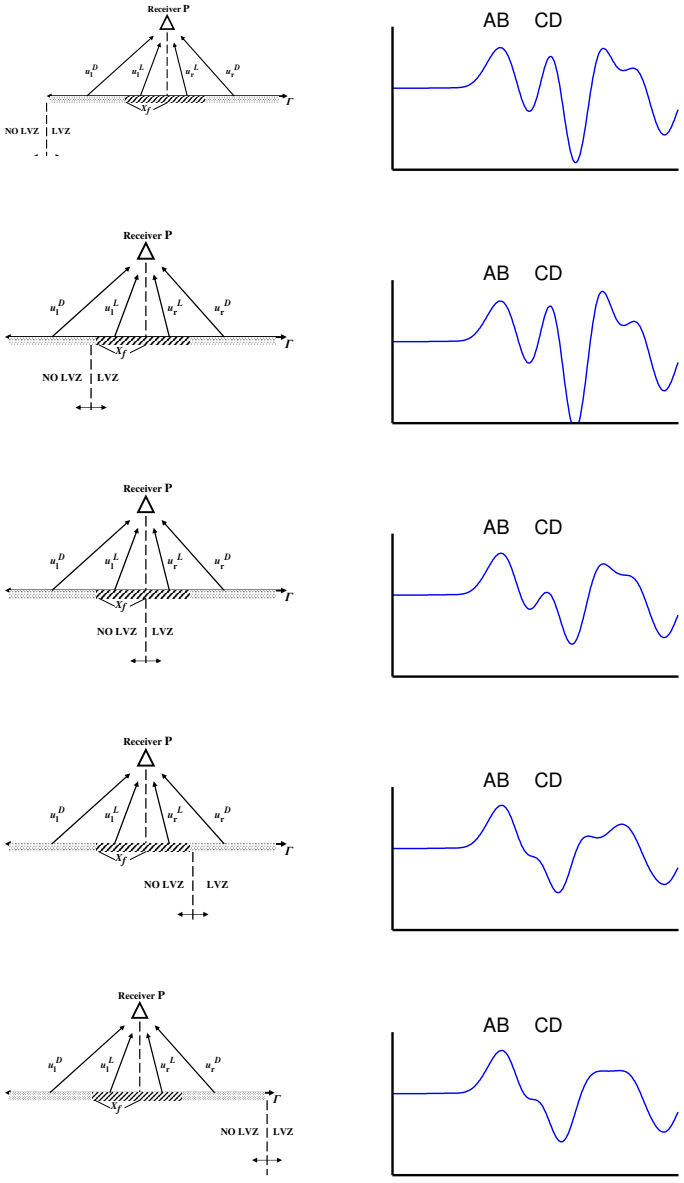

Figure 4.16: DiFD synthetics. Left panels: Cross section view of 3D LVZ model. The boundary of LVZ is shown as vertical bar. Lit region and diffracted region are shown in hatched and Grey color. Right panels: DiFD synthetics corresponds to 3D LVZ model in the left panels.

Chapter 5

Validating Tomographic model with Broadband Waveform Modeling: An Example from the La Ristra Transect in the Southwestern United States

Abstract

Tomographic travel-time models of the La Ristra transect produce excellent waveform fits if we amplify the blurred images into distinct structures. We observe systematic waveform distortions across the western edge of the Great Plains from South American events, starting about 300 km east of the center of Rio Grande Rift zone. The amplitude decreases by more than 50% within array stations spanning less than 200 km while the pulse width increases by more than a factor of 2. This feature is not observed for the data arriving from the northwest. While the tomographic image shows a fast slab-like feature dipping to the southeast beneath the western edge of the Great Plains, synthetics generated from this model do not reproduce the waveform observations. However, once we amplify the tomographic image and increase the velocity contrast between the slab and ambient mantle by a factor of 2-3, the synthetics also produce observed amplitude decay and pulse broadening. In addition to the travel time delay, amplitude variation due to wave phenonema such as slab diffraction, focusing and defocusing provide much tighter constraints on the geometry of the slab and its velocity perturbation and sharpness as demonstrated by grid-search and snapshots of the seismic field. Our preferred model locates the slab 200 km east of the Rio Grande Rift dipping 70°-75° to the southeast, extending to a depth near 600 km with a thickness of 120 km and an amplified velocity of over 4% fast. In short, adding waveform and amplitude components to regional tomographic studies can help validate and establish structural sharpness. *(Geophysical Journal International, in review)*

5.1 Introduction

Travel time tomography has been one of the main tools in studying regional Earth structure. Standard practice for geodynamists is to convert these velocity anomalies into temperature and density and fit geophysical observables such as topography and gravity. Numerical studies have clearly shown significant variations in seismic velocity (**????????**), which has been used to map the temperature and flow field and infer the amount of H_2O and melt. However, tomographic models produced by smooth, damped inversions usually underestimate the amplitude and sharpness of the velocity structure. To validate these tomographic models, it is important to propagate seismic waves through them and compare synthetic waveforms directly with observations, which enables us to enhance and sharpen these models. Body waveform modeling has shown great success in understanding deep mantle structure (**????**), however, it has seldom been used to test against regional tomography models and study lithospheric structure.

It is generally assumed that teleseismic body waves are simple enough to allow cross-correlation techniques to estimate the travel time anomalies. However, as we will show, these waves often display complexity and provide more information about local Earth structure near the recording site. Here we demonstrate how to model the lithospheric structure beneath the eastern portion of the Rio Grande Rift in the southwestern US, one of the major continental rift zones in the world. Understanding the origin and evolution of such continental rifts has generated wide interest in the past several decades. A PASSCAL experiment, La Ristra Transect, was operated in 1999-2001 to investigate the transition from the stable Great Plains, across the Rio Grande Rift zone and on to the Colorado Plateau (**?**) (Fig. 5.1).

Using such a dense linear array, nearly 950 km long with 18 km spacing, enables the imaging of the lithospheric structure in great detail with body wave tomography (**?**), surface wave tomography (**?**) and receiver function analysis (**??**). **?** imaged a linear, southeast dipping slab-like fast velocity anomaly under the western edge of the Great Plains, which is adjacent to the slow Rio Grande Rift (Fig. 5.2).

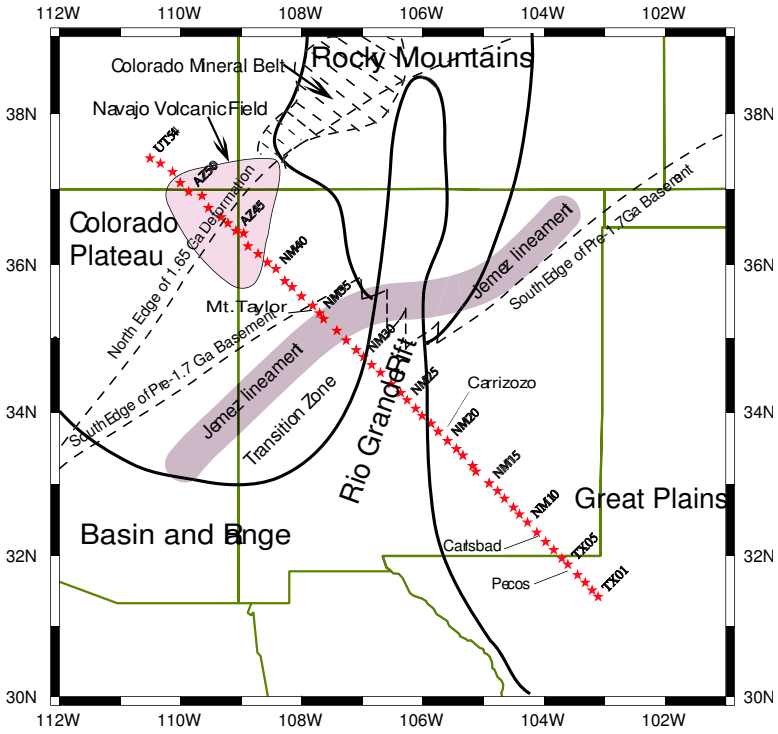

Figure 5.1: Geological settings at La Ristra Transect, southwestern United States (From ?.). The array (red stars) cuts across the Great Plains, the Rio Grande Rift and the Colorado Plateau.

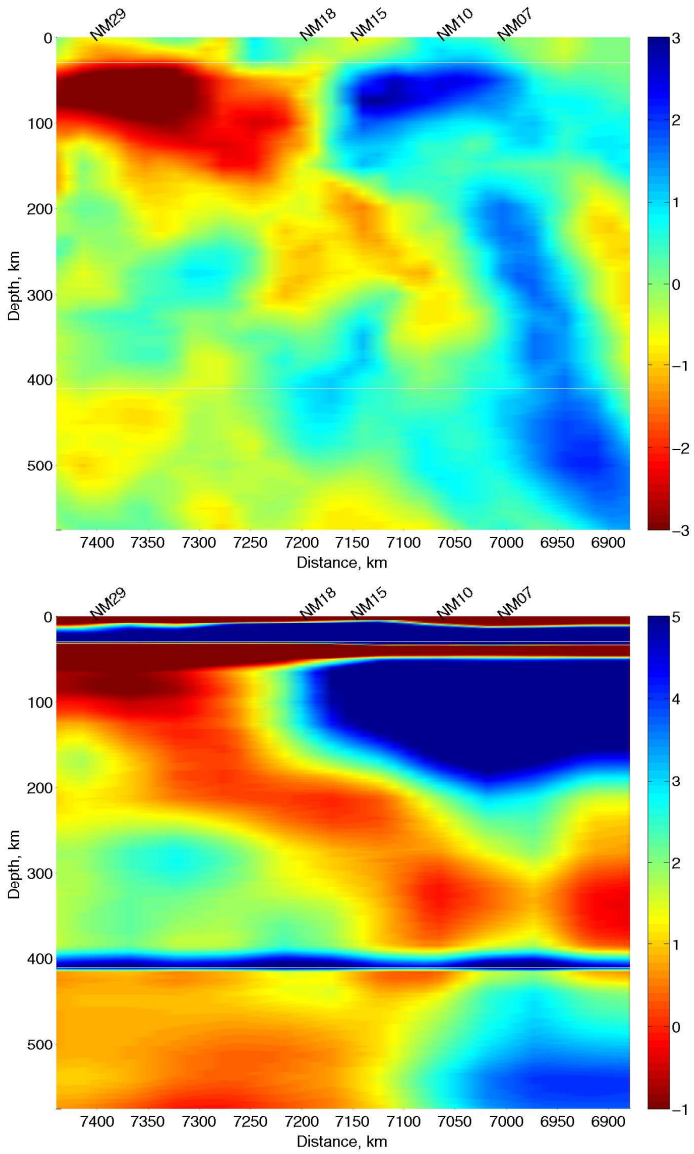

Figure 5.2: S wave tomographic images beneath the array from body waves (upper) **?** and surface waves (lower) (**?**. A fast slab-like anomaly dipping to the southeast is imaged beneath the edge of western Great Plains by **?** but not clear in **?**. The model is plotted with a reference 1-D model, TNA (**?**) removed.

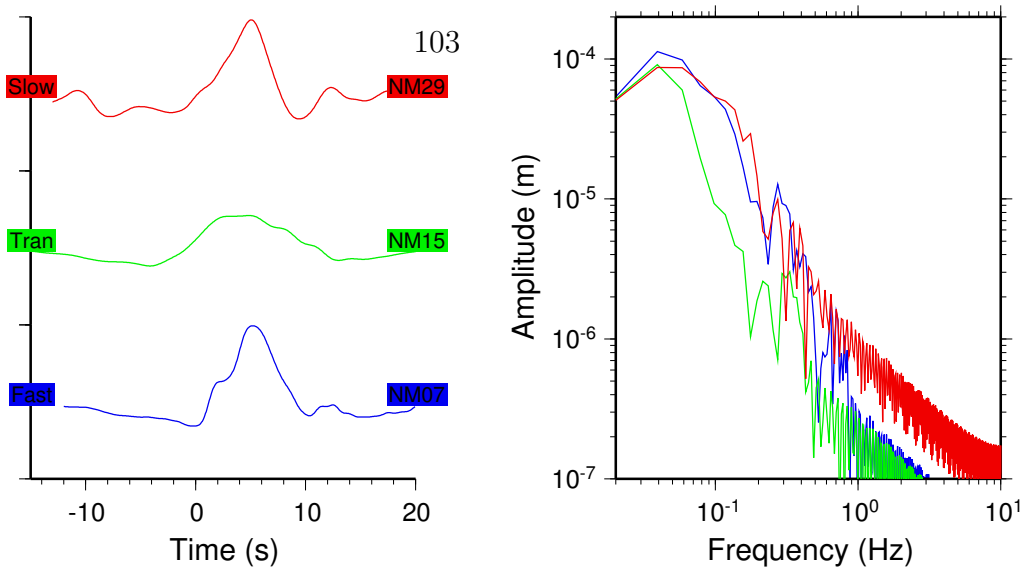

Figure 5.3: Comparison of waveforms recorded at stations NM07, NM15 and NM29 in the time domain (left panel) and frequency domain (right panel). Station NM07 is located on the SE side of the slab structure and station NM29 is located atop the slow region of the Rio Grande Rift. Station NM15, however, is situated near the transition region between the slow rift zone and the fast slab. While the amplitude and frequency content is similar between station NM07 and NM29, the amplitude below 1 Hz at station NM15 is much smaller, by a factor of 2.

? interpreted as downwelling lithosphere produced by small scale convection. The velocity contrast between fast and slow regions reaches up to about 7% in the upper 100 km. **?** performed a surface wave inversion and found complementary results while the slab-like feature is less obvious in their model (Fig. 5.2). In addition, they also argued that the fast lithosphere beneath the Great Plains extends at least to depths of 250 km. Both studies have performed standard resolution tests (checkerboard) to demostrate the robustness of their results, but stop short of a true test by generating the wavefield.

While it is sometimes considered that high attenuation is related to low velocity regions, which lowers amplitudes and increases pulse width, this dataset seems to disagree. For example, suppose we examine a few observations from South American events, essentially arriving along the azimuth of the array (Fig. 5.3).

We picked three stations, NM29 near the center of the slow shallow anomaly (red), NM07 near the center of the fast shallow anomaly (blue), and NM15 a transitional position but closer to NM07. There is little difference between NM29 and NM07

both in the time domain and frequency domain. However, NM15 is the most anomalous. Thus, it appears that wave propagational effects are playing a dominant role in controlling these shapes and amplitude decays. We choose NM07 as the reference station. Such a choice is similar to analyzing waveforms recorded on basin sites relative to that recorded on hard rock sites (**?**). We find it is not critical to our analysis since we are primarily interested in modeling the pattern of changes in travel time and amplitude across the transition region between the western Great Plains and the Rio Grande Rift. We pursue this strategy by generating synthetic waveforms from the above tomographic models and compare them directly with observations to evaluate their effectiveness. To demostrate the usefulness of including waveform and amplitude information, we focus first on the transition from the Great Plains to the rift zone where we expect the largest velocity constrast to occur and waveforms to be heavily distorted. In particular, as we will show later, the waveforms are systematically distorted, broadened and the amplitude decreases accordingly. Instead of cross-correlation, we will pick travel time delays, measure waveform amplitude and use them as observables to compare with synthetic ones. Though other features shown in the tomographic image appear interesting as well, we will leave for future analysis. In this paper, we examine tangential SH broadband waveform first since S wave anomalies typically show much larger distortions than do P waves. In addition, we perform a suite of synthetic tests to demonstrate the usefulness of broadband waveform and amplitude information in deciphering the location, geometry, and depth extent of a subducting slab. We will further analyze P waveforms in a separate chapter and the joint results will provide important constraints on the physical state and composition of this interesting slab feature beneath the western edge of the cratonic Great Plains near the Rio Grande Rift.

We first introduce broadband waveform data from deep events beneath South America recorded by the array. These data display complicated waveform signatures related to mantle structure underneath the array, while the waveform data coming from Kamchatka (NW) indicate relatively simpler behavior. We deconvolve the source wavelet to remove the complexities from the earthquake source and near-source

Event date	Lon	Lat	Depth	Strike	Dip	Rake	Mw
99/09/15	-67.37	-20.73	217.5	351	82	-70	6.4
99/11/30	-69.37	-19.01	138.2	354	81	-107	6.5
00/05/12	-66.85	-23.72	226.6	5	80	-96	7.1
00/04/23	-63.04	-28.41	607.9	171	88	-86	6.9
99/09/18	157.53	51.02	67.7	172	87	92	6.0

Table 5.1: Earthquake source parameter

structure. Then we implement the tomographic models into the 2-D finite difference calculations and compare synthetics against the observed waveform. However, we find the synthetics too simple in waveform shape and inconsistent with the data. Simply amplifying the tomographic models, we achieve a much better fit to the observed waveform complexities.

5.2 Waveform Data

La Ristra transect was configured to take advantage of the 2D geometry with respect to South America events (Table. 5.1).

All the sections span about 2° from the Great Plains into the Rio Gande Rift. More precisely, stations NM07-NM18 are located directly above the slab-like feature shown in Fig. 5.2, although we do not know the true 3D structure. We rotate the horizontal components to obtain the radial component along the great-circle path and corresponding tangential component. Here, we first present P and SH waveforms from event 990915 to the SE (Fig. 5.4). The band-pass filter used here and Fig. 5.5- 5.7 are chosen differently to present waveforms in consistency and accommondate differences in data qualities.

The amplitude of S waves decreases very rapidly in this range with a reduction up to 50%. The waveforms also become broader with less high frequency content. However, such systematic behavior is not seen in the record section from the event arriving from the NW (Fig. 5.5).

We check possible shallow receiver complexities as the causes by examining the

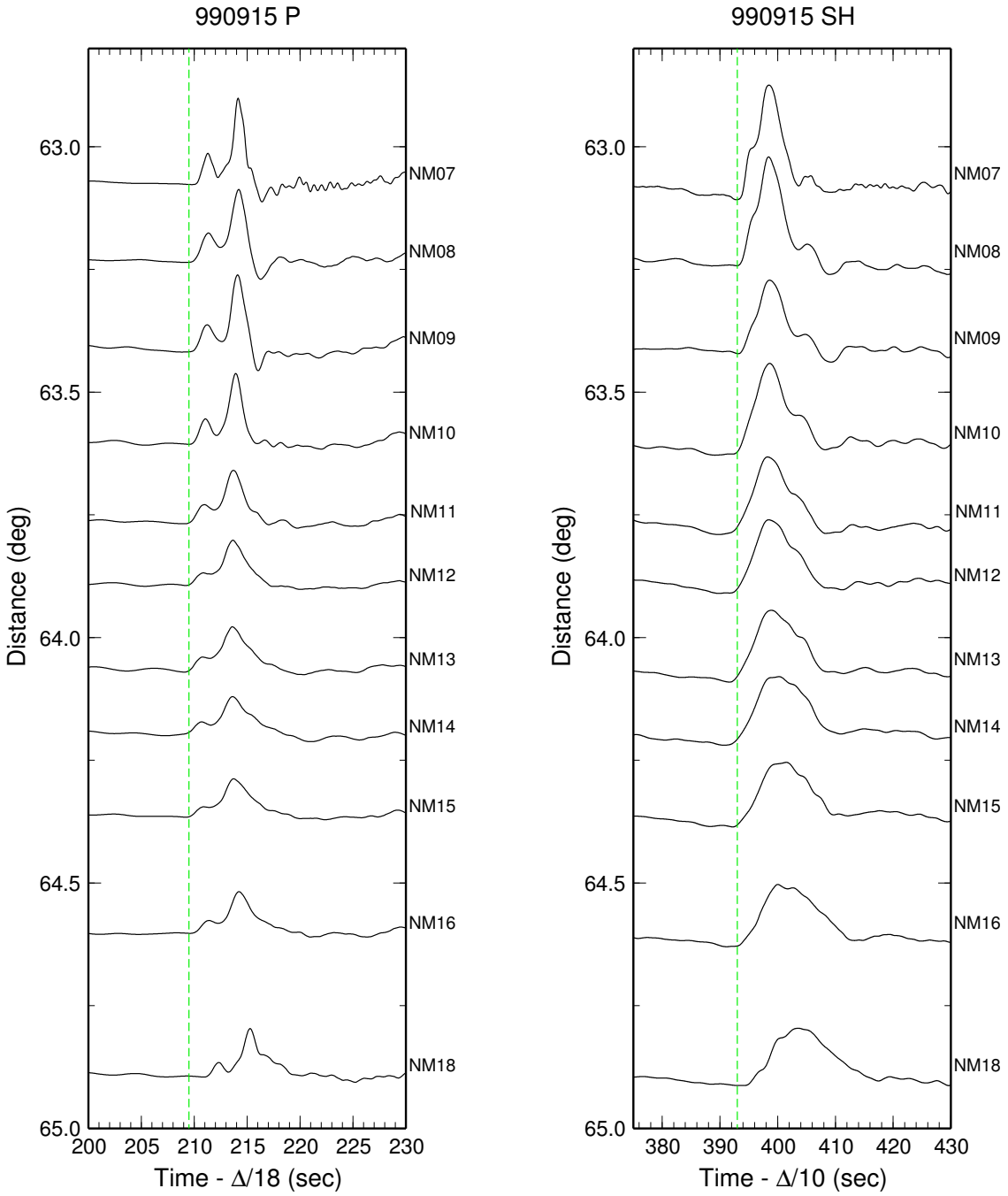

Figure 5.4: P and SH displacement record sections for event 990915 from South America (SE). The absolute amplitudes of P and S waves both reveal significant decreases across the range of distances while their pulse widths become much broader at stations directly above the western side of fast slab. The data are band-pass filtered with corners at 0.02 and 2 Hz for P waves, 0.01 and 2 Hz for S waves, respectively.

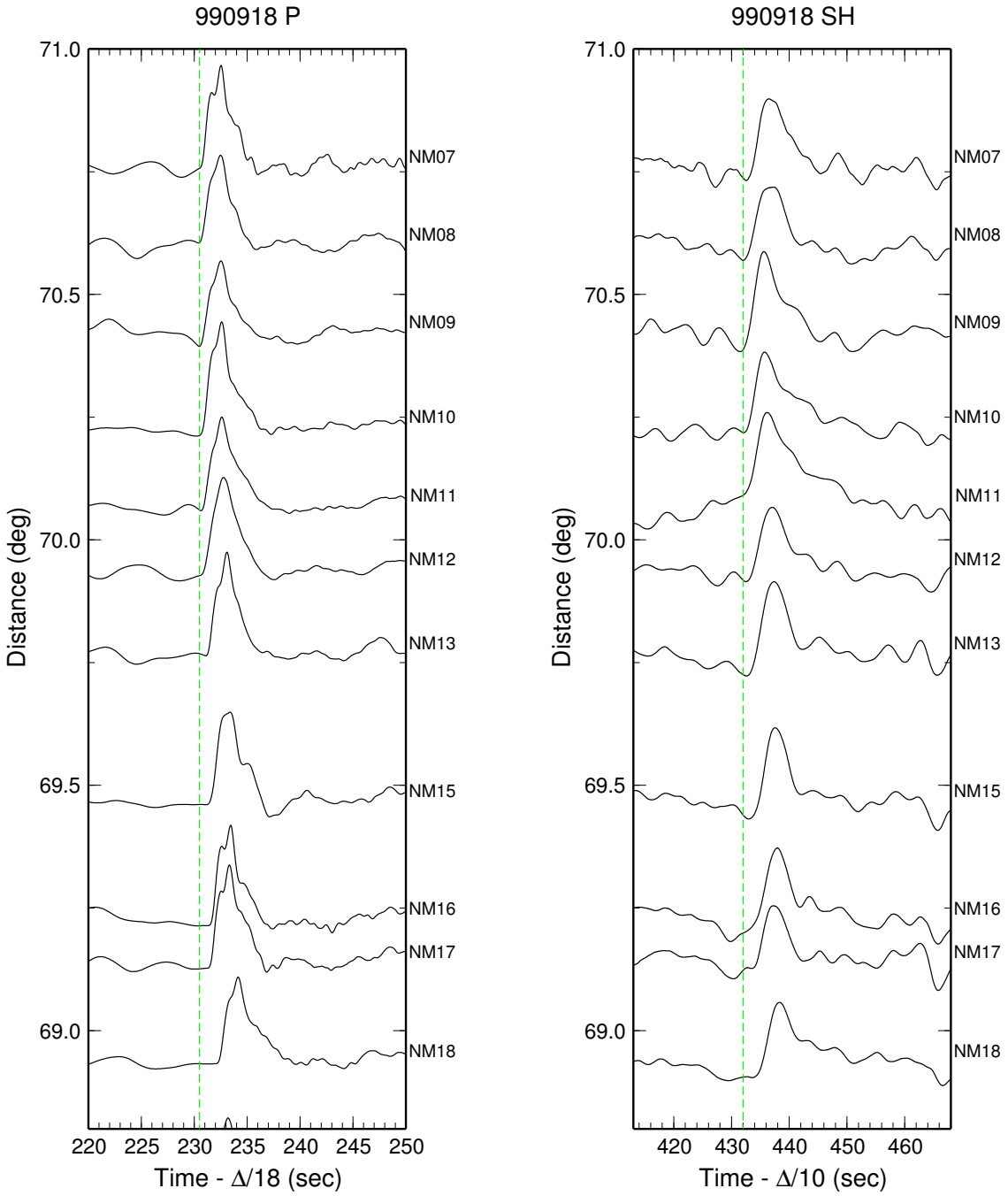

Figure 5.5: P and SH displacement record sections for event 990918 from Kamchatka (NW). The signal-to-noise ratio is lower for this dataset but no significant amplitude decrease or waveform broadening is observed. The data are band-pass filtered with corners at 0.02 and 2 Hz for P waves, 0.02 and 2 Hz for S waves, respectively.

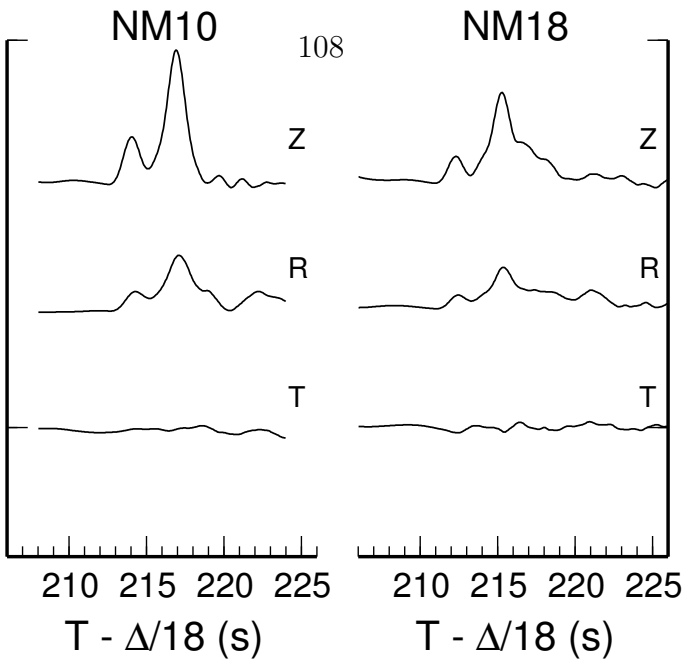

Figure 5.6: P wave displacement recorded on the vertical, radial and tangential components for stations NM10 and NM18 (event 990915). The P waveforms recorded on the vertical and radial components are similar while the tangential component is small, which suggests that, shallow crust does not alter the waveform shape significantly. The data are band-pass filtered with corners at 0.03 and 2 Hz.

vertical and radial components of the P wave. But the similarity of P waves in both vertical and radial components do not support such an argument, while the tangential component is nearly zero, indicating wavefield separation into (P-SV, SH) motions (Fig. 5.6).

The observed waveform distortion and amplitude variations are consistent regardless of the location and the depth of several events to the SE suggesting receiver-side structure effects (Fig. 5.7). In addition, other phases such as sS waves and ScS waves also show similar patterns (Fig. 5.7). Thus, it appears that the observed wavefield is relatively 2D.

In order to remove the complexities introduced by individual earthquake sources, we deconvolve the source wavelet from the raw seismograms to generate an uniform dataset. Since the great-circle paths to these stations differ by less than 2°, the directivity effect on the source-time function in this narrow range is probably very similar.

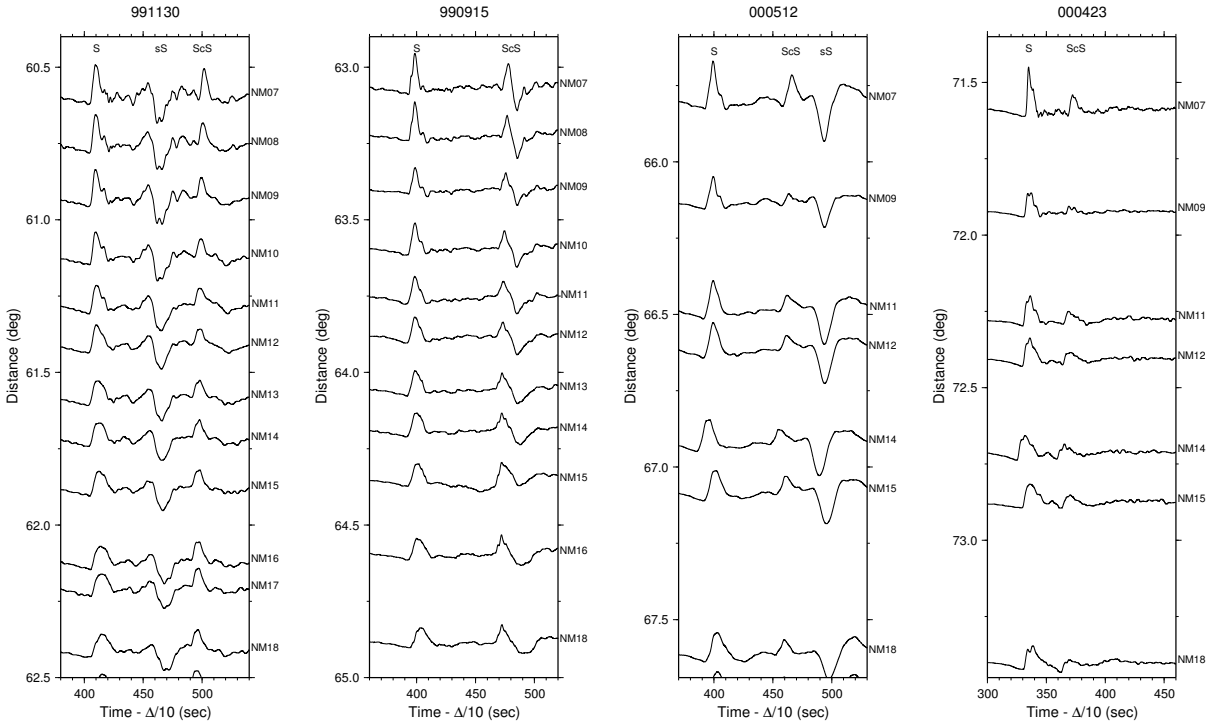

Figure 5.7: Tangential displacement record sections of four events from South America; from left to right: 990915, 991130, 000512, and 000423. All four record sections show systematic amplitude decrease and waveform broadening at stations NM07-NM18. Besides the S wave, the sS wave and ScS wave also reveal similar observations. The data are band-pass filtered with corners at 0.012 and 2 Hz.

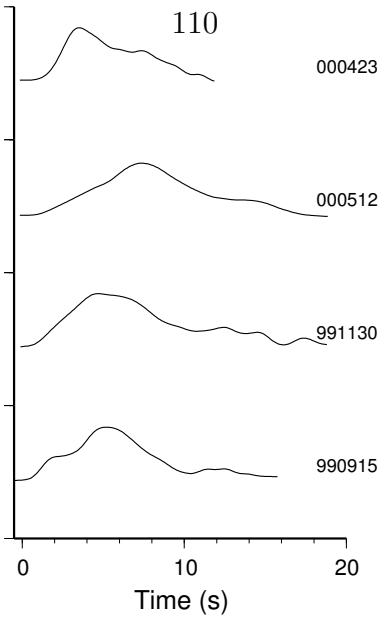

Figure 5.8: Source wavelets used in the deconvolution for event 990915, 991130, 000512 and 000423.

Because we observe systematic waveforms broadening for all events we have analyzed, we decided not to use the stacked S waveform as the source wavelet. We adopt the simplest and narrowest S waveform recorded at station NM07 as the reference station as discussed earlier (Fig. 5.8).

Later we present amplitude ratios and travel time shifts relative to this reference station. We apply a regularized filtered algorithm to stabilize the deconvolution (**?**) and the deconvolved waveform typically has a dominant period of 6-8 secs. All the deconvolved record sections from four events to the SE display consistent results where the peak amplitude of the S wave decreases from station NM07 to NM18 by a factor of 2-3 and the pulse widths is broadened by a factor of 2-3, independent of the source depth and epicentral distance (Fig. 5.9).

The consistency of these datasets strongly suggests that receiver-side structure plays a predominant role in producing such systematic waveform distortion and amplitude decay. We will attempt to model these features with a 2D finite-difference code (**???**). Though only four events are analyzed in the current analysis, we will show indeed that our preferred model can give promised fits to these datasets at multiple frequency bands and predict satisfactory results against data sections from events of different distances and depths.

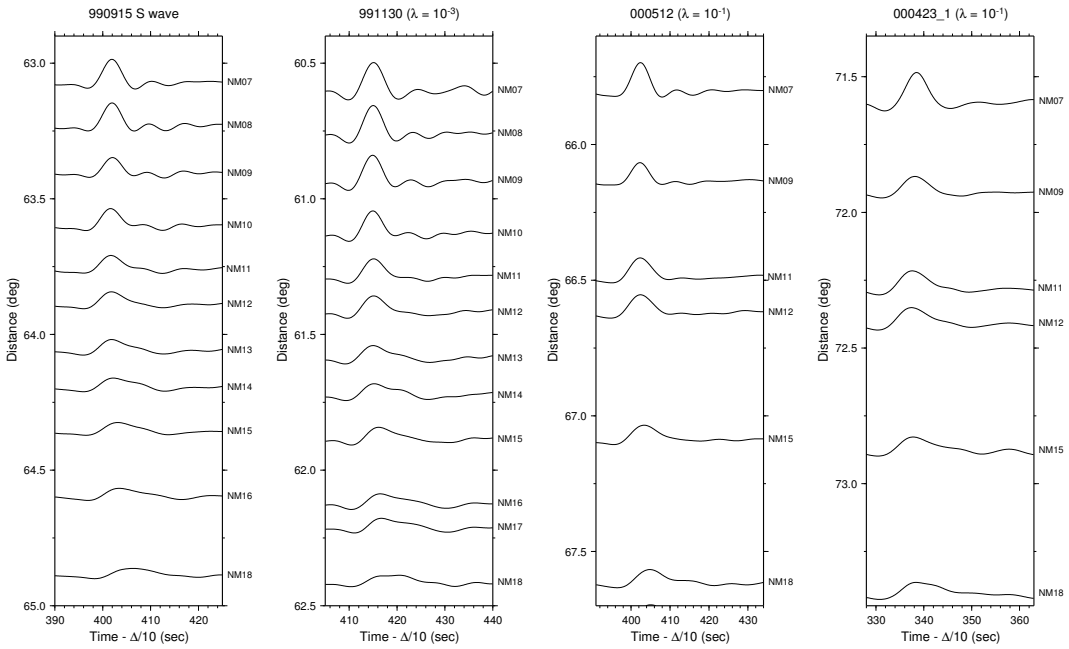

Figure 5.9: Record sections of deconvolved SH waveforms. From left to right: 990915, 991130, 000512 and 000423. The amplitude decreases by more than half from station NM07 to station NM18, while the pulse width increases by more than two times. The dominant period of these deconvolved waveforms is about 6-8 secs.

5.3 Finite Difference Modeling

The finite difference code has been used to investigate the upper mantle triplication (**?**) and core mantle boundary structure (**?**) and it has been successfully benchmarked against 1D reflectivity (**?**) and 2D WKM (**?**). In the following simulations, we adopt a grid spacing of 1.6 km and a time step of 0.077 sec to ensure convergence and accuracy at periods of 3.0 sec and longer. We set the grid boundaries far enough away from the source and receivers to avoid the interference of reflections with the S wave of interest. A Butterworth filter with corners at 0.01 Hz and 0.2 Hz is applied to both the data and synthetics. To examine the effect of long wavelength mantle structure on the waveform broadening and amplitude decay observed, we first compute synthetics based upon the global tomographic model by **?**. It is clearly shown that the long wavelength mantle structure does not produce any noticeable amplitude decay in the record sections of all four events we currently studied (Fig. 5.10).

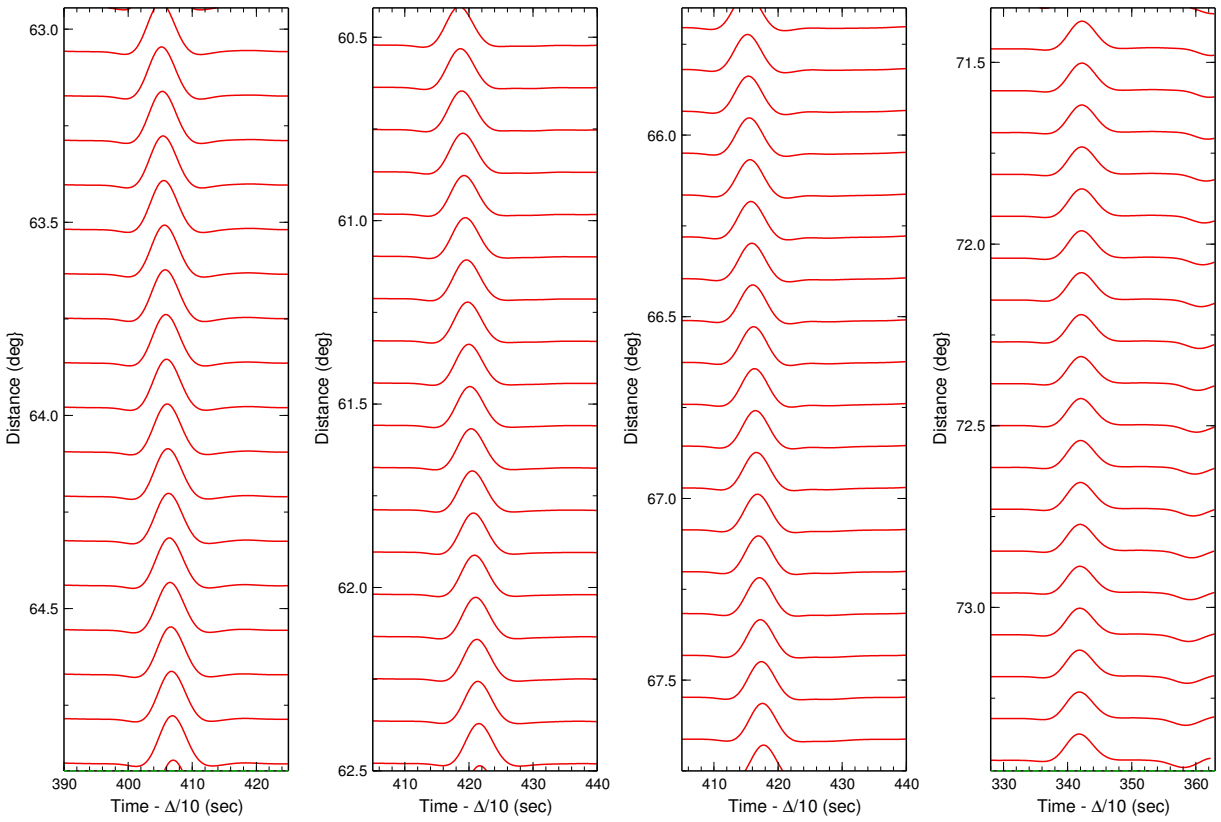

Figure 5.10: Finite-difference (FD) synthetics based upon 2D slices of global S wave tomography model by**?**. From left to right: 990915, 991130, 000512, and 000423. All four sections do not predict any observable differences in the amplitude across the range.

However, if sharp features are present in the source region that are not in Grand's model, we would expect to see changes in the data associated with sampling in the four observed sections. Since the amplitude pattern is stable, we suppose that it is caused by the receiver structure.

5.3.1 Regional tomography model: ?, ?

To examine the effect of receiver-side structure on broadband waveforms, we propagate the waves through the 1-D TNA model (**?**) from the source to the receiver with the 2-D regional tomographic models (**??**) embedded locally beneath the stations. We generate synthetic waveforms and present travel time delays and amplitude ratios relative to reference station NM07. The data and synthetics are both filtered at frequency band of 0.01-0.2 Hz. Since these waveforms are not similar and very differnt in pulse width, we choose not to cross-correlate them but pick the timing of the first swing in filtered waveforms to measure travel time delays, which is similar to **?**'s approach. The amplitude is then computed by taking the envelope of the S wave and measuring its peak. We first examine the data of event 990915 at the range of 63°-65° and synthetics computed from 2D tomography models by **?**. The synthetic waveform is very simple and its amplitude does not decay with distance as much as the data (Fig. 5.11).

In addition, the predicted travel time anomaly varies smoothly across the range (Fig. 5.11). Considering the smoothing and damping made in most inversion procedures, we then simply amplify the magnitude of the velocity anomalies and recompute the synthetics. As introduced earlier, we focus on the waveform phenomena within a relatively small region where velocity varies rapidly. The simple procedure is useful in amplifying these transition regions from fast to slow. But such a process could deteriorate the fit to travel time delays outside the transition region of interest. Overall, the result is satisfying in that the synthetics start revealing similar waveform distortion and amplitude decay as displayed in the data (Fig. 5.11). Our preferred model A is constructed by amplifying the fast anomalies by 2 times and slow anomaly by 4 times

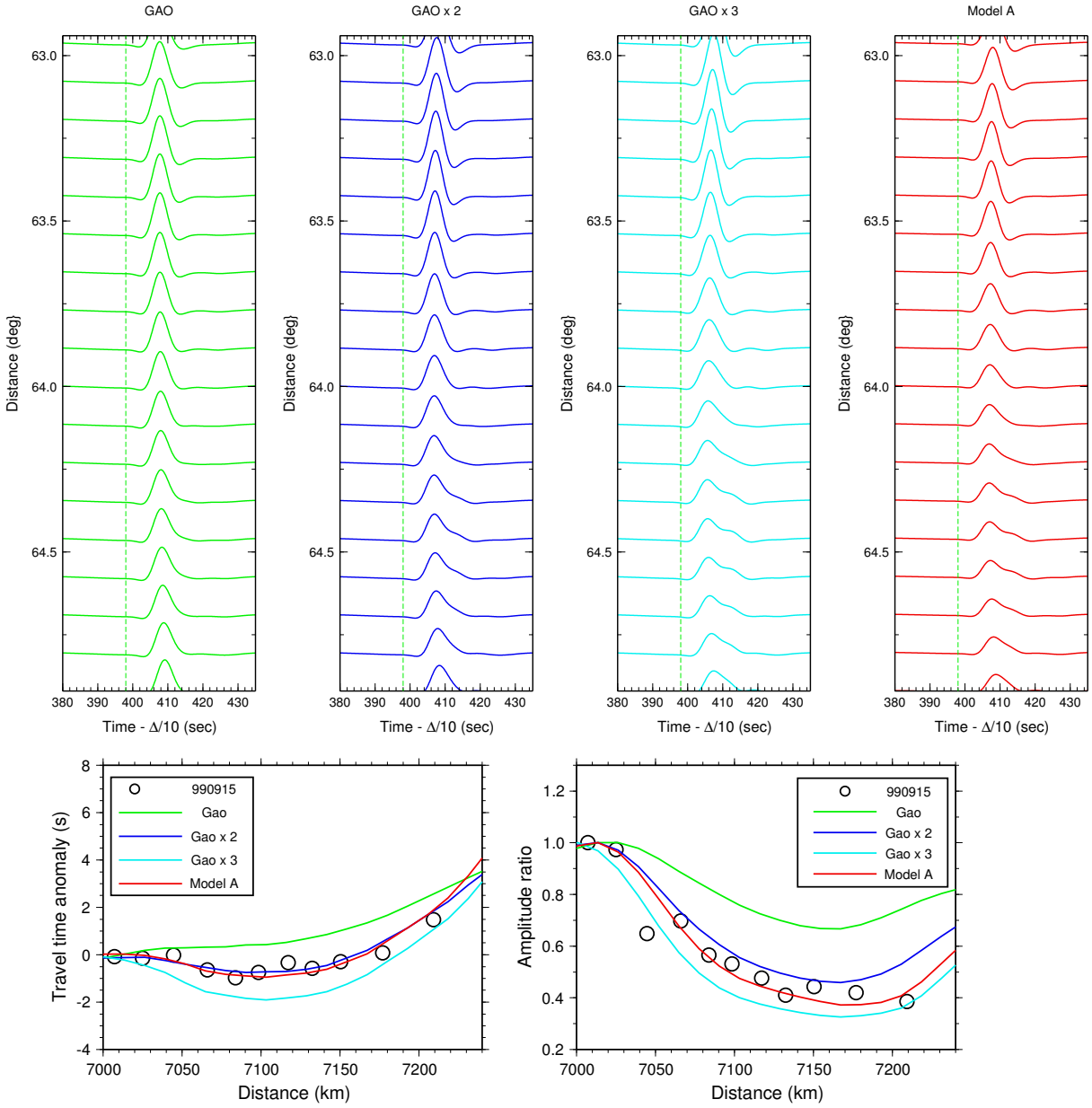

Figure 5.11: FD synthetics (upper panel), travel time delays and amplitude ratio (lower panel). Finite difference synthetics are computed using the S wave tomographic image (Body waves) constructed beneath the array by **?**. The velocity anomaly in the tomographic image is amplified by 1, 2, and 3 times to compute synthetics in the left three columns. To fit both travel time delays and amplitude ratios, model A is constructed by amplifying the fast anomaly by two times and slow anomaly by four times to compute synthetics (right column). The lower left panel shows the comparison of measured travel time delays and predictions. The lower right panel shows the comparison of measured amplitude ratios and predictions. Travel time delays and amplitude ratios are measured relative to reference station NM07.

Model	Gao	Gao×2	Gao×3	Model A
Misfit-Time	3.443	0.806	2.963	0.868
Misfit-Amp	0.808	0.307	0.298	0.219

Table 5.2: Misfit of event 990915

such that it can explain travel time delays and ampltude decays simultanelusly.

To quantify the quality of fit, we compute misfits of travel time delays and amplitude dacay between data and synthetics, respectively. The misfit is difined as the L2 norm of the differences in travel time and amplitude between data and synthetics. Our preferred model is chosen to have low misfits in both travel time delay and amplitude decay. As shown in Fig. 5.11, the preferred model A has the smallest misfit in travel time delays and amplitude decays as well (see Table 5.2).

While teleseismic body wave travel time tomography has a better horizontal resolution, the geometry of raypaths lack vertical resolution. Here we further test possible vertical smearing of the tomography model. In this case, we choose to implement the top 250 km of the velocity model into the FD calculation. This exercise shows that, with an unrealistic amplification factor of 8, we then are able to explain the observations with such a slab-like feature only down to 250 km depth (Fig. 5.12). However, such a model with 50% velocity contrastis is probably physically unlikely.

However, this approach of amplifying anomalies did not work so well with the surface-wave tomography model (**?**). Even if we amplify the velocity perturbation in the mantle, the synthetics do not show similar waveform distortion and the amplitude decay is unsatisfactory (Fig. 5.13). In addition, we are not able to fit the travel time and amplitude simultaneously. As we expected, the surface-wave derived tomography models do not capture the small-scale variation in the upper mantle and probably too smooth, especailly in cases where structures exhibit rapid changes in horizontal direction.

Before evaluating our preferred model against record sections of other events, we also compute travel time delays at frequency range of 0.03-0.1 Hz, which was the frequency range used by **?** to construct tomographic images. We find that their

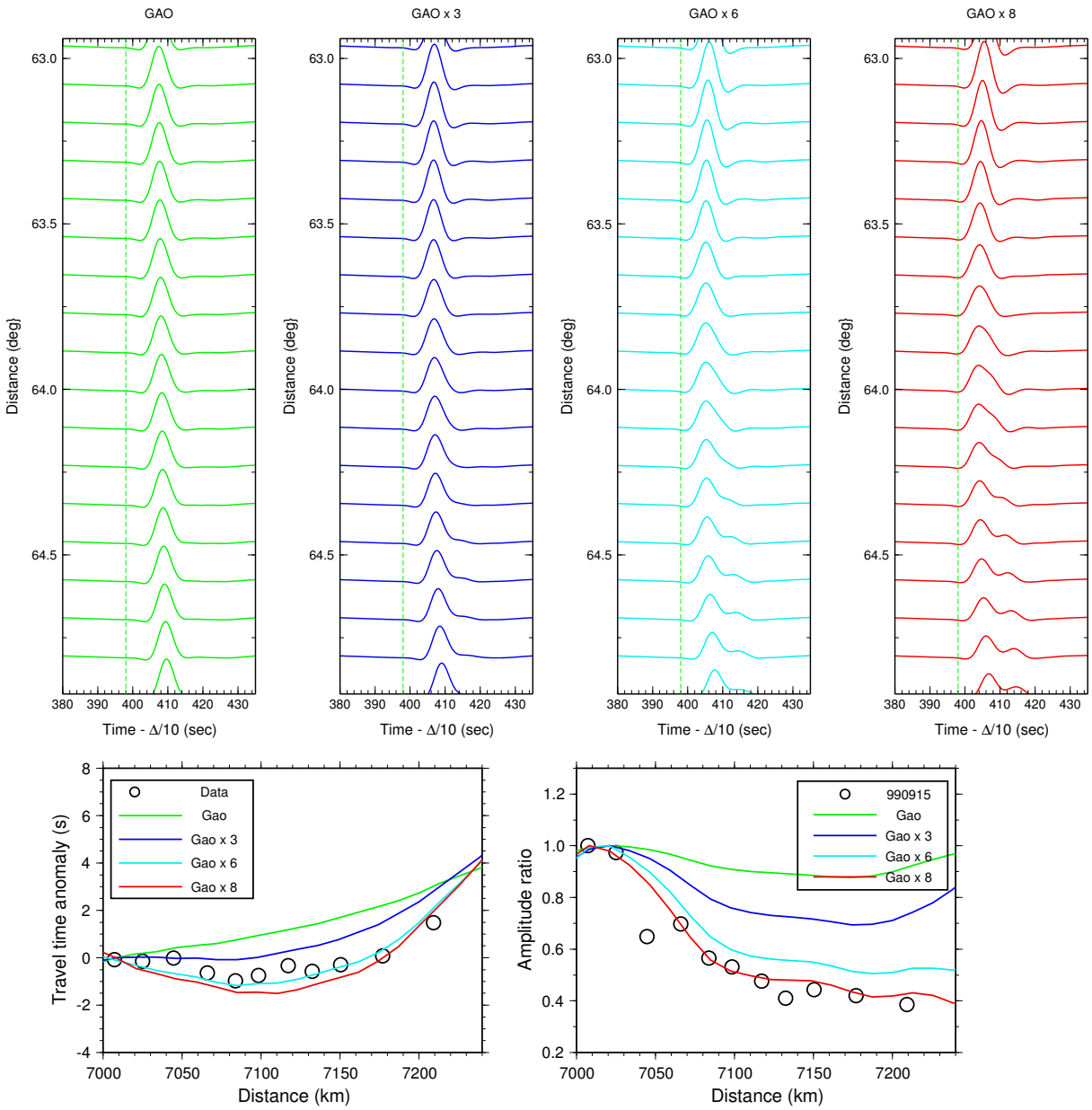

Figure 5.12: Results of a hybrid model containing the tomographic model above 250 km and TNA below. Finite difference synthetics are computed using the S wave tomographic image constructed beneath the array by **?** using surface waves. The velocity anomaly in the tomographic image is amplified by 1, 3, 6, and 8 times to compute synthetics in the top four columns. The lower left panel shows the comparison of measured travel time delays and predictions. The lower right panel shows the comparison of measured amplitude ratios and predictions. The predicted amplitude ratios can be fit with an extremely large amplification factor of 8, while the predicted travel time delays are somewhat too fast.

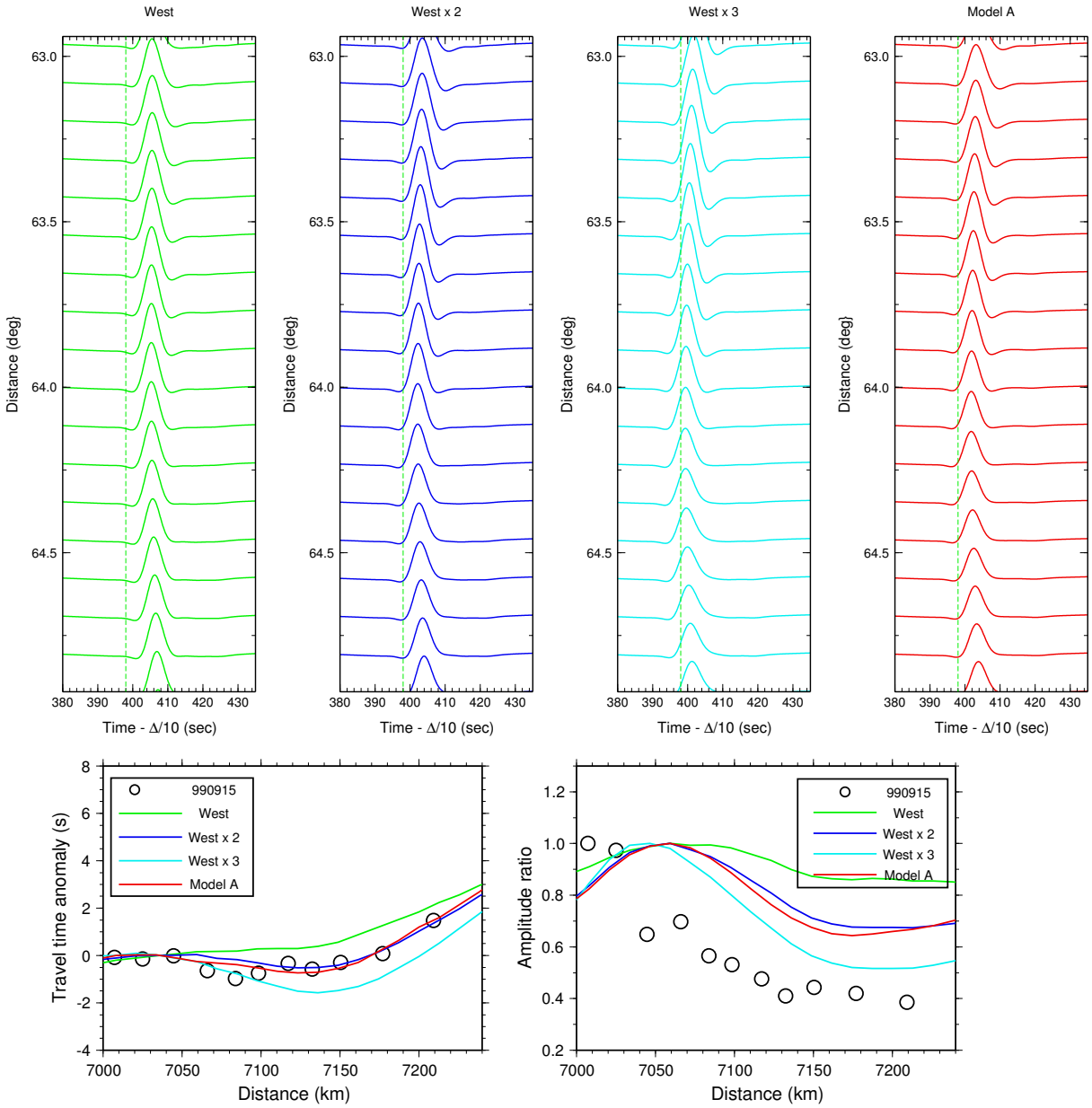

Figure 5.13: FD synthetics (upper panel), travel time delays and amplitude ratio (lower panel). Finite difference synthetics are computed using the S wave tomographic image constructed beneath the array by **?**. The velocity anomaly in the tomographic image is amplified by 1, 2 and 3 times to compute synthetics in the left three columns, while model A is constructed by amplifying the fast anomaly by 2 times and slow anomaly by 4 times to compute synthetics (right column). The lower left panel shows the comparison of measured travel time delays and predictions. The lower right panel shows the comparison of measured amplitude ratios and predictions. The predicted amplitude ratios can be shifted toward the southeast by 50 km to fit the data better, while the fits to measured travel time delays are deteriorated. Also, the synthetics do not reveal enough pulse broadening as shown in the data (Fig. 5.9).

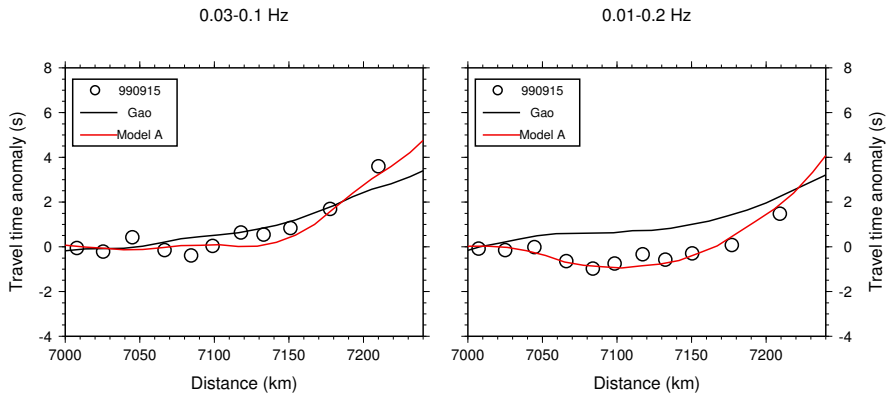

Figure 5.14: Travel time delays computed at two frequency ranges. Left panel shows results at longer periods of 0.03-0.1 Hz and right panel shows results at short periods of 0.01-0.2 Hz.

Model	Gao	Model A
Misfit (0.03-0.1 Hz)	1.740	1.116
Misfit (0.01-0.2 Hz)	3.443	0.868

Table 5.3: Misfit of travel time delays

model indeed explained travel time delays a lot better at longer period (Fig. 5.14, Table 5.3). However, our preferred model A can fit the data slightly better at longer period but also explain data at shorter period (Fig. 5.14, Table 5.3) very well.

When we convolved the source wavelet with synthetics of our preferred model A, the data and synthetics were compatible in amplitude variation, travel time delay, and waveform distortion (Fig. 5.15).

To further demonstrate the consistency of previous results, we model another three events at the distances of 60.5°-62.5° (event 991130), 65.8°-67.8° (event 000512), and 71.5°-73.5° (event 000423), using the same procedure to predict travel time delays and amplitude decays. We obtain similar results with amplification factors of 2-3 while the travel time delays and amplitude variations are reasonably well reproduced by model A (Fig. 5.16, Fig. 5.17, see also Table 5.4-5.6). Other tested models are not favored because of the inability to explain the travel time and amplitude simultaneously. For instance, model Gao×3 explained the amplitude decays of event 000423 well. However, it produced a large misfit in travel time delays (Table 5.6). Model

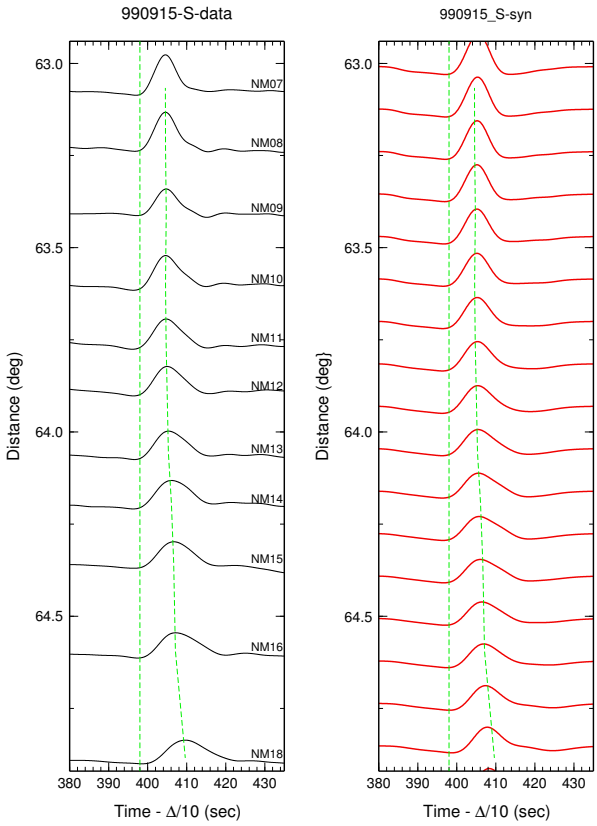

Figure 5.15: Comparison of data and synthetics of model A. Synthetics are convolved with the source wavelet of event 990915 while both data and synthetics are band-pass filtered with corners at 0.01 Hz and 0.125 Hz.

Model	Gao	Gao×2	Gao×3	Model A
Misfit - Time	2.485	1.686	4.934	2.352
Misfit - Amp	0.997	0.421	0.165	0.197

Table 5.4: Misfit of event 991130

Model	Gao	Gao×2	Gao×3	Model A
Misfit - Time	1.380	1.325	3.809	1.616
Misfit - Amp	0.612	0.251	0.334	0.229

Table 5.5: Misfit of event 000512

Gao×2 explained the travel time delays well for event 991130, but it produced large misfit in explaining amplitude data. In summary, it is clear that receiver-side slab-like structure indeed plays a significant role in producing waveform complexities and amplitude changes, and the slab-like velocity anomaly likely exists as displayed in the tomographic model.

However, based on our modeling, the velocity contrast between the fast slab-like feature and the ambient mantle is on average of about 4% down to 600 km or so. Such a structure produced a distorted wavefield and multiple arrivals. This explanation can be easily seen in the snapshots of wave propagation along the slab structure (Fig. 5.3.1). It is clear that the wavefront is more advanced inside the high velocity slab and finally splits apart. It also creates long period energy between the two arrivals evident in the data.

Model	Gao	Gao×2	Gao×3	Model A
Misfit - Time	2.670	0.868	1.953	0.906
Misfit - Amp	0.765	0.342	0.280	0.279

Table 5.6: Misfit of event 000423

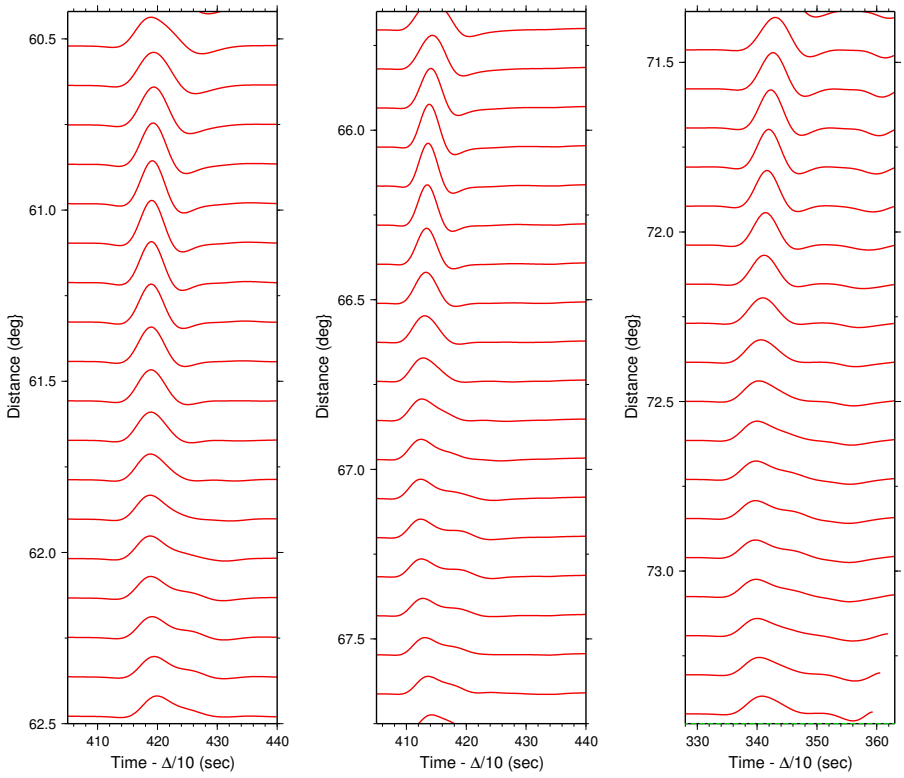

Figure 5.16: Finite difference synthetics computed using amplified tomographic image model A for other three events from South America. From left to right: 991130, 000512, and 000423. All synthetic record sections show comparable waveform distortions observed in the data (Fig. 5.9).

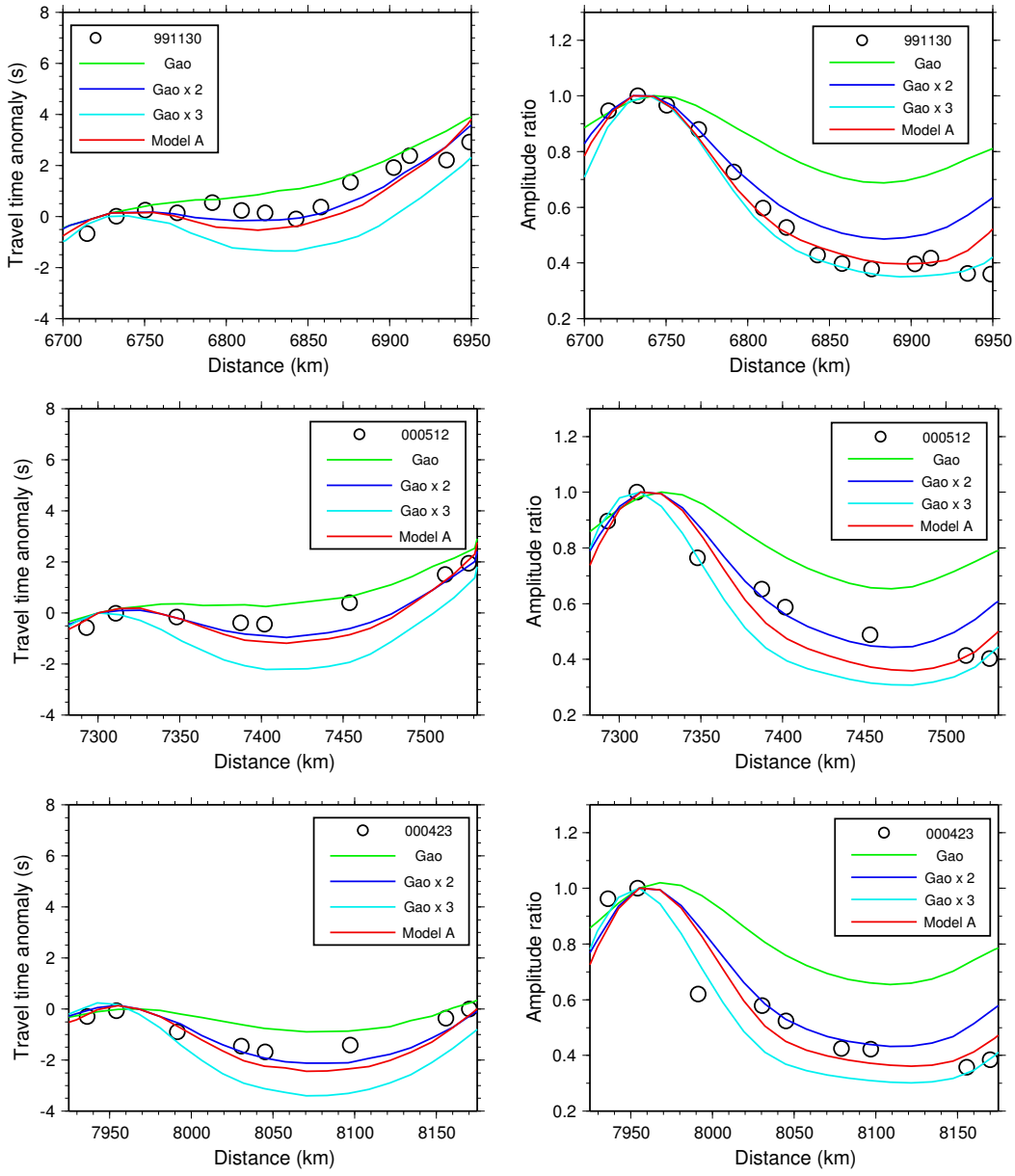

Figure 5.17: Travel time delays and amplitude ratio computed for the three events displayed in Fig. 5.16. From top to bottom: 991130, 000512, 000423. In general, model A predicted nice results against these dataets at different ranges (see also Table 5.4- 5.6).

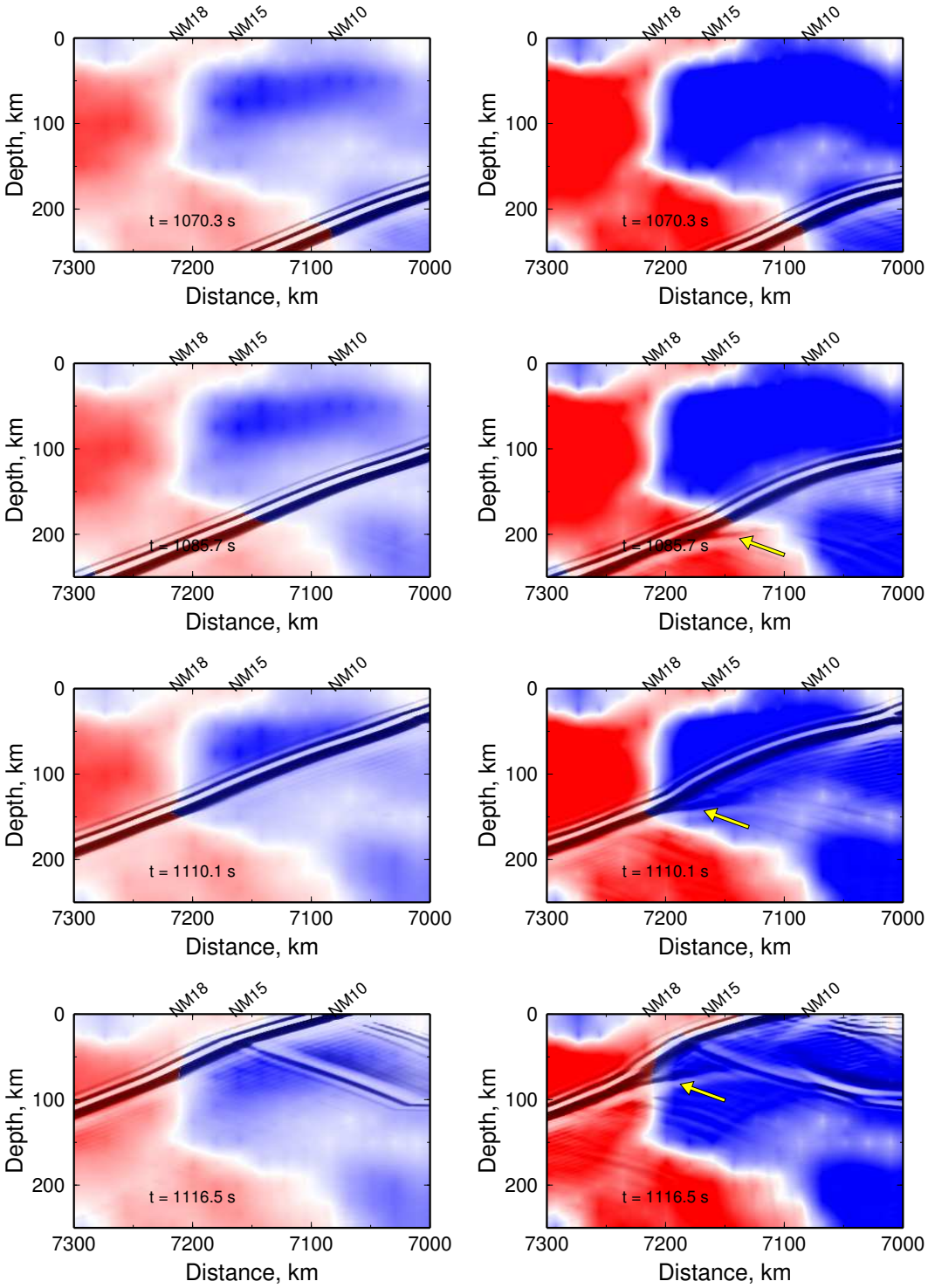

Figure 5.18: Finite difference snapshots. Left: Computed with original tomographic model. Right: Computed with amplified tomographic model (amplidied by 3 times). The wavefront is bent more in the amplified model than the original model at time 1070.3 sec. 15 secs later, the wavefront is starting to broke (yellow arrow) and is separated into two in the case of amplified tomographic image. The broken wavefront is separated even more through continuous propagations along the velocity boundary. Only the top 250 km is presented with background image of velocity anomaly. The location of station NM10, NM15, and NM18 is indicated for reference.

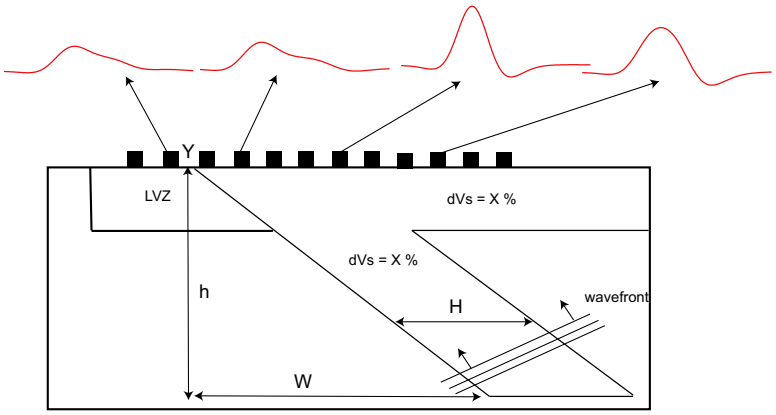

Figure 5.19: Slab diffraction and forward modeling setup. The waveform is narrow and amplified after crossing the eastern side of the slab. Just beyond the western side of the slab where fast-to-slow transition occurs, the waveform is much broadened and the amplitude is decreased due to waveform multipathing. Toward the west, the multipathing is less obvious and the waveform will start to be a simple pulse again. The slab is defined as a dipping layer X% fast than the surroundings. The dipping of the slab is defined by the depth h and the horizontal shift X, while the width of the slab is H. The western tip of the slab is defined at the point Y on the surface. A -3% low velocity layer, 150 km thick is added adjacent to the slab in certain cases (see Table. 5.7).

5.4 Idealized Model Sensitivity: Slab Thickness and Geometry

We demonstrated above that the combination of travel time delays and amplitude patterns set strong constraints on upper mantle structure. However, it is difficult to investigate uniqueness when previously introduced model A has so many complications. To appreciate the essential features of the structure model, we conducted a sensitivity experiment where Gao's model is idealized to a few parameters (Fig. 5.19). We performed tests with various combinations of parameters as given in Table. 5.7, which includes possible trade-offs between the depth of the slab and its velocity perturbation. We find that the amplitude is the smallest near the far-side the slab (NW) and the largest near the near-side of the slab (SE), but within the slab (Fig. 5.20).

While the largest amplitude is sensitive to the width and dip of the slab, the amplitude decay rate with distance primarily depends on the thickness of the slab, where

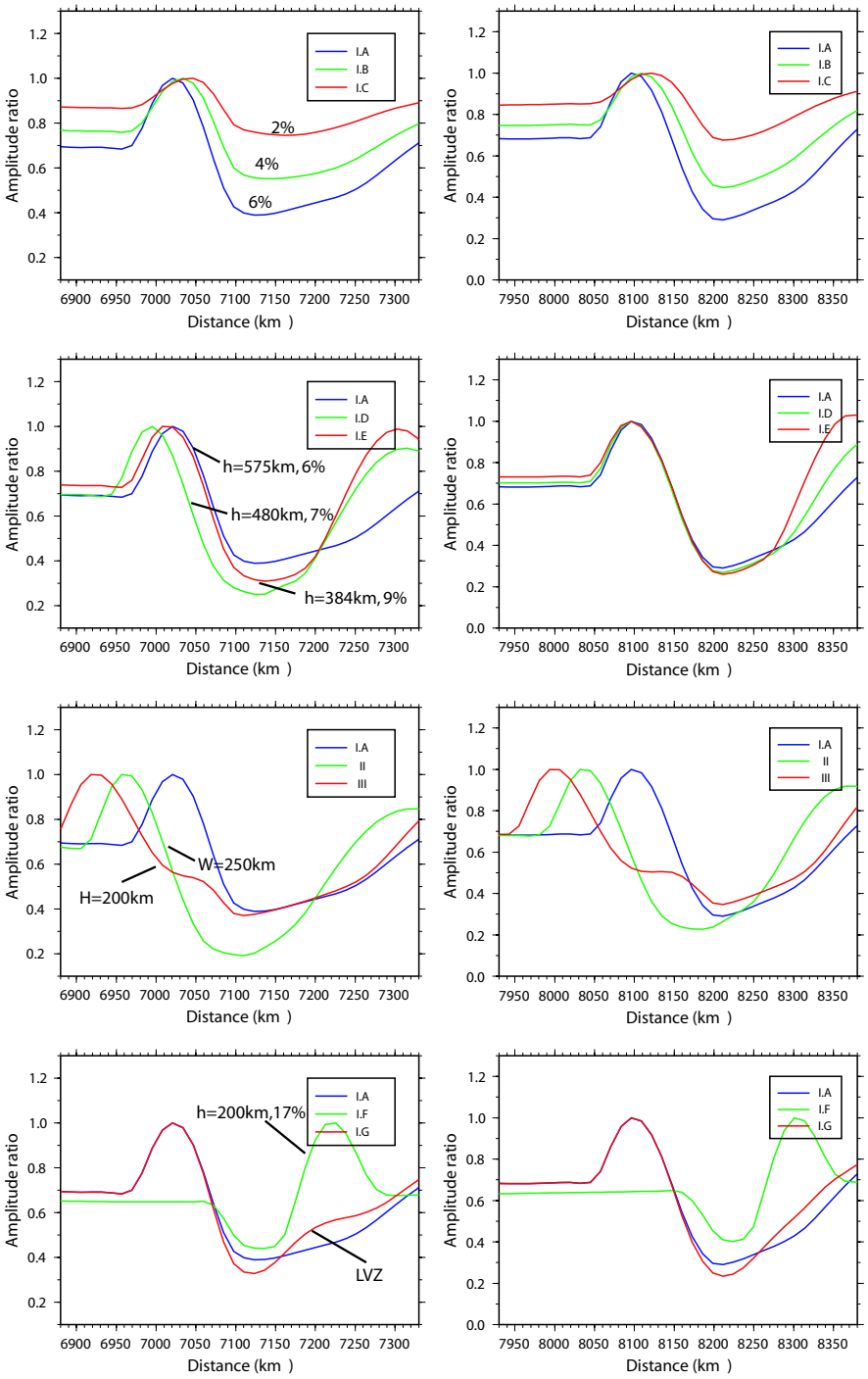

Figure 5.20: Sensitivity test of synthetic amplitude ratios against slab geometry. Left panels show the result computed at shorter ranges ($62° - 66.5°$) and right panels show the result computed at longer ranges ($71.5° - 75°$). The first row presents the comparisons of synthetic amplitude ratios against the velocity anomaly of the slab (model I.A, I.B, I.C). The second row presents comparisons of synthetic amplitude ratios against the depth of the slab (model I.A, I.D, I.E). The third row present comparisons of synthetic amplitude ratio against the dipping angle and the width of the slab (model I.A, II, III). The fourth row presents comparisons of synthetic amplitude ratios against the existence of the slab and low velocity zone (model I.A, I.F, I.G). See also Table. 5.7.

No.	W (km)	H (km)	h (km)	X (%)	LVZ	Y (km)
I.A	150	100	575	6	no	7100, 8200
I.B	150	100	575	4	no	7100, 8200
I.C	150	100	575	2	no	7100, 8200
I.D	150	100	480	7	no	7100, 8200
I.E	150	100	384	9	no	7100, 8200
I.F	150	100	200	17	no	7100, 8200
I.G	150	100	575	6	yes	7100, 8200
II	250	100	575	6	no	7100, 8200
III	150	200	575	6	no	7100, 8200

Table 5.7: Sensitivity test slab parameters

the wider the slab, the lower the decay rate. If we fix the dip and the width of the slab but change its depth extent, we find that the amplitude starts to increase again and after passing the far side of the slab (Fig. 5.20), there exists another amplitude maximum that is sensitive to the depth of the slab. The larger the amplitude, the shallower the slab penetrates. This observation is similar to the previous study by **?**, who used ray theory and Gaussian-beam method to study the waveform amplitude from events inside the slab. Finally, we test an extreme case with no slab but a fast-to-slow transition in the top 200 km. In this case, we consider possible vertical smearing in the tomographic image that produces artificial slab-like feature. We still observe the amplitude decay associated with the diffraction along the boundary, but there is no amplification as seen close to the near-side (SE) (Fig. 5.20). In addition, the amplitude focusing and defocusing varies rapidly on a much shorter scale. If we add a low velocity zone in the top 200 km on the far-side of the slab to simulate the slow rift zones imaged by the tomography, it only modifies the amplitude pattern beyond the far-side of the slab. Finally, we examine the degree of amplitude decay due to the slab diffraction. It is clear that this depends on the velocity anomaly of the slab. However, it also depends on the incident angle of teleseismic waves and the dipping angle of the slab. Such trade-offs can be reconciled if the travel time anomaly is simultaneously analyzed. In summary, the amplitude variation provides fairly good constraints on the location, geometry, depth extent and its velocity perturbation. It

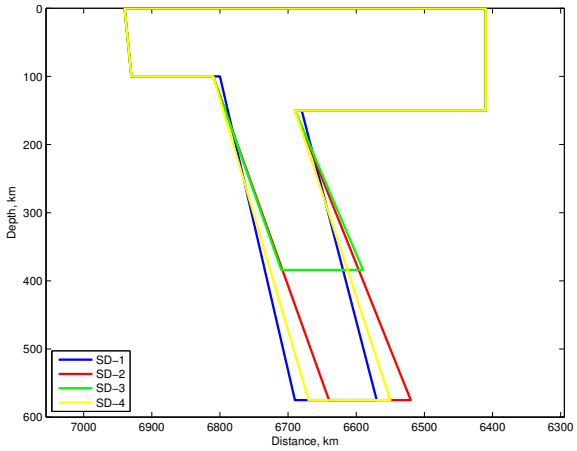

Figure 5.21: Modeling slab geometry under La Ristra transect. The geometry of the slab is constructed to mimic the S wave tomographic image by **?** and explain the observed travel time delays and amplitude ratios for event 991130 (See also Table. 5.8).

No.	W (km)	H (km)	h (km)	X (%)	LVZ	Y (km)
SD-1	120	120	575	6	no	6940
SD-2	170	120	575	3.75	no	6940
SD-3	100	120	380	4.5	no	6940
SD-4	140	120	575	4.5	no	6940

Table 5.8: La Ristra slab parameters

provides complementary information to the travel time data.

Based on these sensitivity tests, we produced a simplified model for the slab near the Rio Grande Rift to explain the data (event 991130). This model is built to mimic the tomographic image and fit the data through a systematic search of model parameters (Table. 5.8). As a result, we are able to generate models which can reproduce the amplitude decay and travel time anomaly (Fig. 5.21).

We can fit the amplitude decay with a 120 km wide, 6% fast slab dipping 80° to the southeast and reaching 575 km depth (Model SD-1), but it fails to explain the travel time anomalies (Fig. 5.22, Table 5.9).

Model SD-2 consists of a 3.75% fast slab dipping 70° to the southeast. This model is able to fit the amplitude and travel time anomaly simultaneously. Model SD-3 consists of 4.5% fast slab of 380 km depth. It explains the travel time delays

Model	SD-1	SD-2	SD-3	SD-4
Misfit-Time	3.759	1.845	1.909	2.385
Misfit-Amp	0.216	0.228	0.465	0.190

Table 5.9: Misfit of event 991130

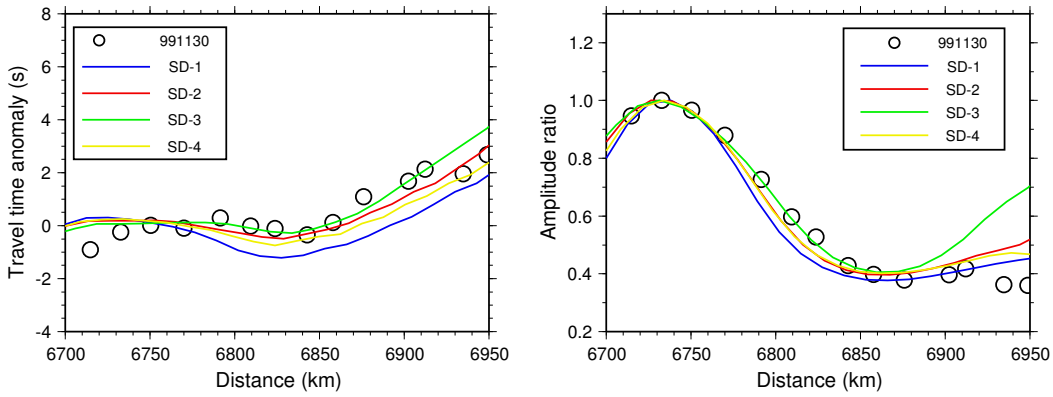

Figure 5.22: FD synthetic travel time delays and amplitude ratios for model SD-1, SD-2, SD-3 and SD-4. Model SD-1 explains the observed amplitude ratios reasonably well but the predicted travel time is systematic too early. Model SD-3 explains the observed travel time delay but fails to predict the amplitude ratios correctly. Model SD-2 and SD-3 are able to explain the observed amplitude ratios as well as travel time delays.

reasonably well, but the amplitude increases much faster than the data recorded at the far-side of the slab (see also Table 5.9), which suggests that the slab is likely too shallow (Fig. 5.22). We find that model SD-4 can also fit the amplitude decay well with a 4.5% fast slab dipping 75° to the SE, though it slightly deteriorated the fit to travel time delays (Table 5.9). As a demonstration, we show that the tradeoff between slab geometry and its velocity anomaly can be reconciled by the use of both amplitude and travel time anomalies. If we fit the amplitude decay with the fast slab, it produces a much faster arrival than the observed. In addition, the amplitude variation across the slab also provides information on the depth extent of the slab. Using both travel time and amplitudes, we can mostly eliminate tradeoffs between the geometry of the slab and its velocity anomaly.

5.5 Discussion and Conclusion

As we have presented in earlier sections, the broadband waveform and amplitude variations recorded by the La Ristra transect provide valuable constraints on the magnitude and geometry of the velocity structure in the mantle. The slab-like feature presented by **?** is validated and amplified according to our modeling result. As shown previously, we directly amplify the tomographic image and test it against waveform and amplitude data. Though this procedure is rather simple and it can certainly involve more delicated processes, we primarily target on how the travel time tomographic images can be improved and validated through forward modeling waveforms and amplitudes.

We generalize such wave propagation phenomena and present a physical interpretation. As pointed out by **?** and **?**, source-side slab diffraction/multipathing causes waveform distortion recorded teleseismically, such as S and ScS, and also cause focusing and defousing at teleseismic distances (**??????**). Such waveform effects and amplitude perturbation due to the high-velocity slab have been used to constrain the geometry and depth of the slab. However, in this study, we focus on the slab structure near the receiver side probed by incoming teleseismic waves. The multi-pathing from

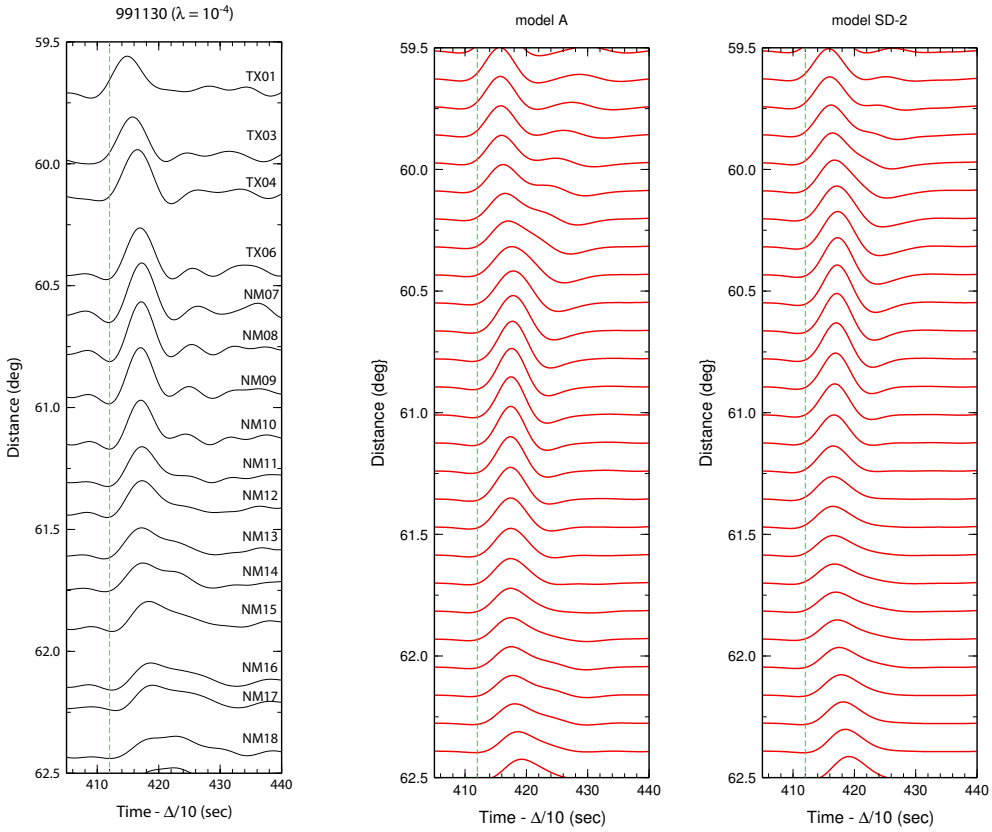

Figure 5.23: Comparison of deconvolved record section (991130) (left panel) and FD synthetic record sections of enhanced model A (middle panel) and simplified model SD-2 (panel).

the SE side of slab (slow-to-fast boundary) magnifies the amplitude of the waveform (Fig. 5.19 Fig. 5.23). Such amplification is analogous to the upper mantle triplication where two branches cross over, except the velocity jump is not horizontal but nearly vertical (**?**). We find amplified tomographic image model A explains the waveform broadening better than simplified model SD-2 for stations to the NW of NM07 (Fig. 5.23, see also Table 5.4, Table 5.9).

However, model SD-2 did a better job mimicking the amplitude increase for stations SE of NM07. Such amplification is analogous to the upper mantle triplications where two branches cross over, except the velocity jump (or large velocity gradient) is not horizontal but nearly vertical (**?**). It also gives tight control in determining the SE boundary of the slab while waveform amplitude decay rate with distance

provides estimate of slab thickness. The slab feature imaged by **?** is amplified and supported by our waveform analysis. Our preferred model has a 3.8-4.5% fast slab of 120 km thickness dipping at an angle of 70°-75° and reaching the depth near 570 km (Fig. 5.21). Also, the slab feature is shifted eastward from the center of the Rio Grande Rift zone by 200 km.

We have presented a systematic analysis of the use of amplitude information in exploring the slab-like structure beneath the eastern edge of the Rio Grande Rift in the southwestern United States. Broadband waveform from South American events recorded by the La Ristra transect clearly show systematic amplitude decays across the slab-like feature imaged by the travel time tomography (**?**). These waveforms demostrated clear multipathing phenomena supported by finite difference simulations where incoming teleseismic wavefronts are distorted by slab features beneath the receivers. In general, the tomographic image has to be amplified about three times to explain the waveform distortion at stations near the transition from the western Great Plain and the Rio Grande Rift. We performed sensitivity tests and found that the amplitude information can be utilized with the travel time delays to better determine the slab geometry. Our preferred model has a fast slab $(3.8 - 4.5\%)$ with thickness of 120 km dipping $70° - 75°$ to the southeast to nearly 600 km and is consistent with both travel time and amplitude observations.

Chapter 6

Probing Deep Continental lithosphere Near the Rio Grande Rift, Southwestern United States, using P and S Wave Broadband Waveforms

Abstract

East of the Rio Grande Rift, tomographic images of teleseismic data have revealed a SE dipping, slab-like structure underneath the western edge of the Great Plains in the southwestern United States. However, finite difference synthetics of such a model do not reproduce the waveform distortions as observed in broadband waveform data recorded along the La Ristra Transect. In addition to travel time anomalies, **?** demonstrated how to use S waveforms and their amplitude patterns to further constrain on the magnitude of the anomalous structure. Their preferred model suggests the slab-like structure is about 4 % fast, 120 km thick and dipping $70^\circ - 75^\circ$ to the SE to about a depth of 600 km. We adopt the preferred S wave model from **?**, and scale the P wave model using a suite of scaling factors $dlnV_s/dlnV_p$. We find the scaling factor $\sim$ 1.25 fits the P waves broadband waveforms and amplitude patterns best. Such a lower SF suggests that the slab-like anomaly is probably also compositionally distinct and SF $\sim$ 1.25 corresponds to $\Delta(V_p/V_s) \sim$ -0.77 % when $\Delta V_s/V_s \sim$ 4 %. This result suggested that the slab-like anomaly is depleted and its $Mg\#$ $(Mg/(Mg + Fe))$ is nearly 3 units higher than that of the adjoining mantle asthenosphere. This estimate is consistent with xenolith data on variations in $Mg\#$ between the sub-continental lithosphere and the mantle asthenosphere. Temperature contrast at depths below 200 km can reach $\sim$ 375 K and it is probably large enough to promote the observed foundering of the continental lithosphere beneath the western Great Plains. Our result suggests that the deeper part of the continental lithosphere is less depleted and it can be recycled into the mantle. *(To be Submitted)*

6.1 Introduction

The longevity of continental roots and their variations from region to region are often debated (??????????????). The depleted, less dense and more viscous continental roots have to overcome the erosion of convective mantle flow with probably higher viscosity (?). However, once delamination or lithospheric removal occurs, the stress field in the crust and shallow mantle is modified to be extensional and it often produces extension, rifting, and magmatism at the surface. PASSCAL experiments have imaged the existence of linearly dipping fast anomalies adjacent to continental rift zones near cratons (??). In particular, ? inverted travel time anomalies across the La Ristra Transect across the Rio Grande Rift in the southwestern US and found a SE-dipping fast velocity anomaly down to 600 km. They interpreted this down-welling as the result of small scale convection beneath the Rio Grande Rift.

Body-wave derived travel time tomographic images often suffer vertical smearing depending on the length of seismic arrays and inversion schemes. ? have shown how broadband waveforms and amplitude systematics can be used to refine the velocity structure underneath such a dense array. They amplified the S wave travel time tomographic images by ? (Fig. 6.1) and found that synthetics computed from such an amplified image explained the waveform data and amplitudes much better than did the original image.

Sharp velocity changes cause diffraction, which partitions the energy and causes waveform distortion and produces pulse broadening. ? produced a model featuring a slab-like fast anomaly near the western edge of the Great Plains dipping SE down to nearly 600 km, with S velocity contrast reaching 4% within a 50 km zone. In addition, they also constructed simplified models to mimic the tomographic image that explained the data equally well (Fig. 6.2). Their best simplified model also features a 4% fast slab dipping 70°-75° to the southeast, with a thickness of 120 km. They performed a series of synthetic tests and showed how the amplitude decay recorded at stations directly above the slab can be utilized with travel time delays to model the slab thickness, dipping angle, penetration depth, and velocity perturbation.

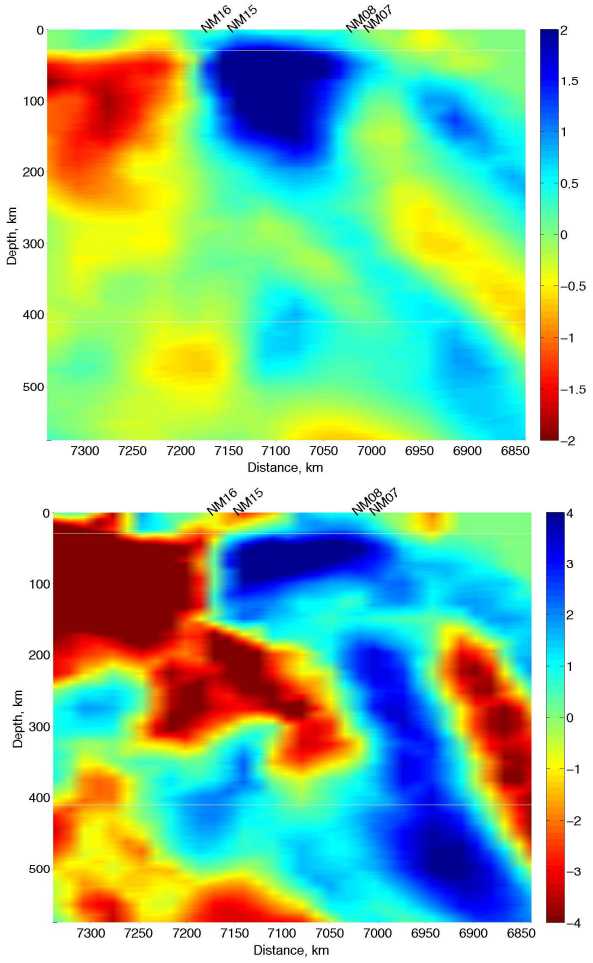

Figure 6.1: P wave tomographic image (top panel) and enhanced S wave tomographic image (bottom panel) (**??**). The original S wave tomographic model is enhanced two times in the fast regions and four times in the slow regions. This procedure increases the velocity contrast between the fast slab-like structure and ambient mantle.

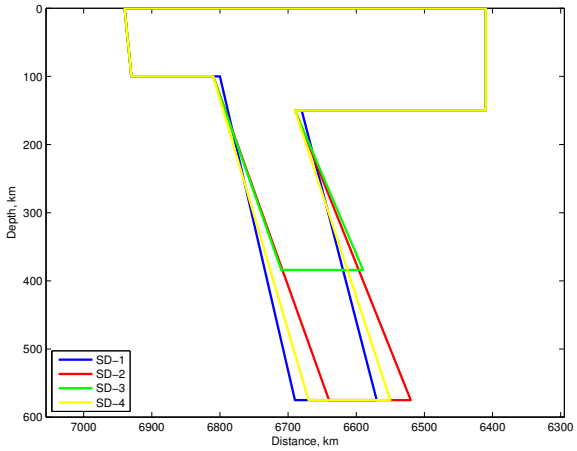

Figure 6.2: Simplified slab geometry under La Ristra transect. The geometry of the slab is constructed to mimic the S wave tomographic image by **?** and explain the observed travel time delays and amplitude ratios for events from South America (**?**, see also Table. 5.1).

To study the physical origin of velocity anomalies, the scaling factor $dlnV_s/dlnV_p$ (SF) obtained from seismic studies has been used to infer the origin of mantle heterogeneity (**????????**). One important aspect of such exercises is the validity of consistent measure of correlated structures. However, it is not easy to measure this SF directly since most tomography images are inverted separately for P and S wave velocity structure. In addition, the frequency range of seismic waves used to construct P and S tomographic models is not uniform and therefore a frequency-dependent correction of anelastic effects is necessary. Surface waves are also useful in mapping the upper mantle structure but it is difficult to infer the origin of rapidly varying structure. In this analysis, we focus on the SF directly by modeling P and S waves record sections of the same source-receiver pair using exactly the same model geometry. This will ensure the measure of SF is meaningful for further inferences on the origin of mantle anomalies. Note that regardless of the origin of the wave speed anomaly in such a slab feature, it is reasonable to suggest that this material was derived from the deep cratonic lithosphere underneath the Great Plains and later sank to the deep upper mantle, either actively or passively. Along with an estimate on shear velocity variation in the mantle, the SF factor can be directly converted to a

change in V_p/V_s ratio, which can provide good constraints on changes in the $Mg\#$ ($Mg/(Mg+Fe)\times 100$) for upper mantle peridotites (**?**).

In this study, we will model the P waveforms following the same procedure used in the S wave study. First we attempted to fit the P waveforms by amplifying the P velocity image produced by **?** (Fig. 6.1) but synthetics propagated through these models failed to reproduce waveform distortion observed in the data (Fig. **??**). Note the reduced amplitude and broadening spanning the stations NM07 to NM15, indicating of a diffration pattern. To model these records, we simply scaled the S wave model obtained from modeling S wave record sections to a P wave model using different SFs ranging from 1 to 2. We found that the P waveforms are best fit in shape, time delays and amplitude ratio with an SF near 1.25. This estimated SF is derived using the same source-receiver pair for P and S waveforms. We then estimate the contrast in $Mg\#$, temperature and density in the deep upper mantle across the western Great Plain and the Rio Grande Rift. The geometry of the problem gives a way to directly compare the continental lithosphere against the mantle asthenosphere. Finally, we discuss its implications for the origin of the slab-like feature near the edge of stable continental Great Plains and Rio Grande Rift in the southwestern US.

6.2 Observations

The P waveforms recorded along the La Ristra transect display a strong azimuthal dependence as do the S waveforms. Observations of events arriving from the NW show relatively uniform amplitude along the array while events from the SE (South America) display the strong reduction in amplitude (Fig. 6.3). The P wavelets from this particular event (990915) have two distinct pulses indicating the earthquake source complexity, when recorded at stations NM07 and NM08. However, it is clear that the long period tails start to develop and follow the second peak of P wavelets at other stations farther to the northwest, while P wave amplitude drops by 50% within this range. Moreover, other phases such as PcP, pP and sP also reveal similar wave phenomena (Fig. **??**), which is consistent with observations in S waves (**?**).

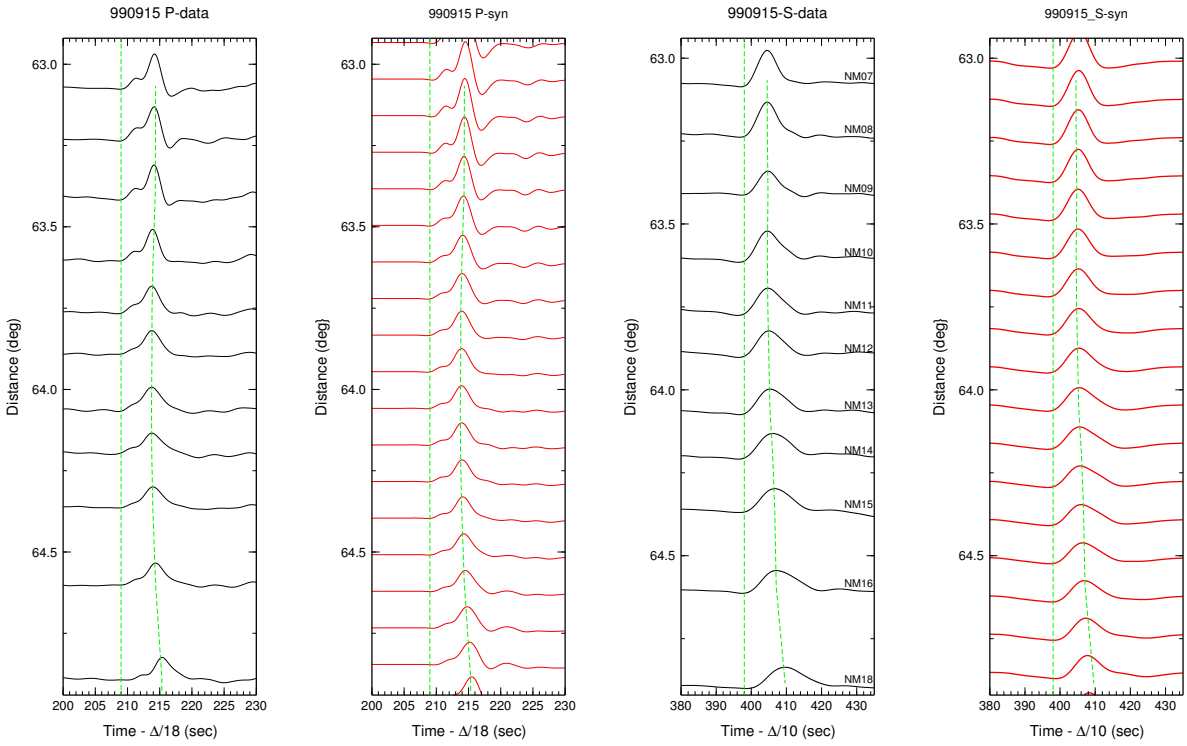

Figure 6.3: Comparison of P and SH displacement record sections for event 990915 from South America (SE) against synthetic record sections. Synthetics are computed with model A (Fig. 6.1, S model) using SF of 1.25. Both data and synthetics are bandpass filtered with corners at 0.02 and 0.3 Hz for P wave and 0.01 Hz and 0.125 Hz for S wave, respectively. Dashed lines mark the timings of the onset and waveform peaks relative to station NM07.